



Numerical study based on experimental datas of the active control applied to the flow past a backward facing ramp

Rémy Simonet

► To cite this version:

Rémy Simonet. Numerical study based on experimental datas of the active control applied to the flow past a backward facing ramp. Fluids mechanics [physics.class-ph]. 2019. dumas-02023452

HAL Id: dumas-02023452

<https://dumas.ccsd.cnrs.fr/dumas-02023452>

Submitted on 18 Feb 2019

HAL is a multi-disciplinary open access archive for the deposit and dissemination of scientific research documents, whether they are published or not. The documents may come from teaching and research institutions in France or abroad, or from public or private research centers.

L'archive ouverte pluridisciplinaire **HAL**, est destinée au dépôt et à la diffusion de documents scientifiques de niveau recherche, publiés ou non, émanant des établissements d'enseignement et de recherche français ou étrangers, des laboratoires publics ou privés.

CONSERVATOIRE NATIONAL DES ARTS ET METIERS

PARIS

MEMOIRE

présenté en vue d'obtenir

le DIPLOME d'INGENIEUR CNAM

SPECIALITE : Mécanique

OPTION : Aérodynamique

par :

SIMONET Rémy

**Numerical study based on experimental datas of the active control applied
to the flow past a backward facing ramp.**

Soutenu le 18 janvier 2019

JURY

PRESIDENT :

Monsieur GRASSO Francesco

Professeur et Directeur de l'INSTITUT AEROTECHNIQUE

MEMBRES :

Monsieur ALLEAU Jean-Luc

Ingénieur calcul et analyses SAFRAN LANDING SYSTEMS

Monsieur BARAZZUTTI Fabrice

Ingénieur simulation numérique PSA GROUPE

Monsieur HLEVCA Dan

Ingénieur de recherche à l'INSTITUT AEROTECHNIQUE

Abstract

This work is based on Dan Hlevca and his co-authors' experimental study [5] on the active control applied to the flow past a backward facing ramp inclined to 25° . Following the study of the mean and unsteady flow without control applied, the authors use the control technique of pulsed jets because they are interested in the influence of the variation of the duty cycle DC, keeping the blowing time constant. In their conclusion they highlight the disappearance of the recirculation bubble at the back of the body and the recovery of pressure at whatever frequency and the applied DC. An estimate of the drag coefficient is calculated by extrapolating the pressure measurements taken in a median longitudinal plane. The authors remain cautious about interpretations related to the drag coefficient, not knowing explicitly the pressure distribution on the body in the transverse dimension.

The present work is the numerical portion of this study. RANS simulations with first order turbulence models were conducted to try to extract the solution on the mean flow in a relatively short time. The incapacity of RANS models of the first order classical turbulence model to determine a precise solution of the mean flow around this type of geometry imposed a mixed numerical strategy URANS-LES, also named DES (detached eddy simulation). Characteristics of the mean and unsteady flow are thus found, which made it possible to validate the numerical DES approach chosen and to consider the solution obtained as a suitable estimation of the physical problem. A restriction of the computation domain with the introduction of synthetic turbulent fluctuations at the inlet makes it possible to envisage, on the delay of this internship and with the computer means at disposal, a simulation of the controlled case. We could afterwards look at the pressure distribution of the entire body and determine the influence of the pulsed jets on the pressure drag coefficient.

Résumé

Ce travail s'appuie sur l'étude expérimentale de Dan Hlevca et de ses co-auteurs [5] du contrôle actif d'un écoulement au passage de la discontinuité géométrique d'une rampe arrière inclinée à 25° . Après l'étude du cas sans contrôle de l'écoulement moyen et instationnaire ses auteurs utilisent la technique de contrôle de jets pulsés et s'intéressent à l'influence de la variation du cycle de fonctionnement (DC Duty Cycle) et en gardant le temps de soufflage constant. Dans leur conclusion ils mettent, entre autres, en évidence la disparition de la bulle de recirculation à l'arrière du profile et la récupération de pression quelque soit la fréquence et le DC appliqués. Une estimation du coefficient de trainée est calculée par extrapolation des mesures de pression prises dans un plan longitudinal médian. Les auteurs restent prudents sur les interprétations liées au coefficient de trainée ne connaissant pas explicitement la répartition de pression sur le profile dans la dimension transverse.

Le présent travail est la partie numérique de cette étude. Des simulations de type RANS avec une modélisation de la turbulence au premier ordre ont été menées, afin d'essayer d'obtenir en un temps relativement court la solution sur l'écoulement moyen. L'incapacité des modèles RANS de turbulence classiques du premier ordre à déterminer une solution précise de l'écoulement moyen autour de ce type de géométrie impose une stratégie numérique de type mixte URANS-LES nommée encore DES (Detached Eddy Simulation). Les caractéristiques de l'écoulement moyen et instationnaire sont ainsi retrouvées, ce qui permet de valider la démarche numérique type DES choisie et de considérer la solution obtenue comme une bonne estimation du problème physique. Une restriction du domaine de calcul avec l'introduction de fluctuations turbulentes simulées à l'entrée permet d'envisager, sur le délai de ce stage et avec les moyens informatiques à disposition, une simulation du cas de contrôle. On peut alors s'intéresser à la répartition de pression sur l'intégralité du profile et déterminer l'influence des jets pulsés sur le coefficient de trainée en pression.

Direction and context

This work was conducted at the Institut AéroTechnique in context for my end-of-studies internship and was directed by Professor Francesco Grasso, chair of industrial aerodynamics at the Conservatoire National des Arts et Métiers and president of the Institut AéroTechnique. I would like to thank him for giving me the opportunity to work on this present topic.

I thank Davide Modesti for his help at the beginning of my internship and for his helpful advice. I extend my gratitude to Dan Hlevca for informing me about his experimental results. I am thankful to the other members of the IAT for helping me in the preparation of the calculation server and for giving me the opportunity to visit institute's the wind-tunnels. I would also like to thank Isabelle Lecacheur for the time she spent integrating me into the IAT.

The total duration of this work was 12 months.

List of Abbreviations

AFC Active Flow Control

IAT Institut AéroTechnique

EU European Union

RANS Reynolds Averaged Navier Stokes

URANS Unsteady Reynolds Averaged Navier Stokes

LES Large Eddy Simulation

DES Detached Eddy Simulation

NACA National Advisory Committee for Aeronautics

FEM Finite Element Method

FVM Finite Volume Method

DC Duty Cycle

Contents

1	Introduction	8
1.1	Global context	9
1.2	Context of the study	10
1.2.1	Topology of the flow	11
1.2.2	Flow control techniques	12
2	Problem	14
2.1	Description of the studied geometry and domain	15
2.1.1	Ramp and its support	15
2.1.2	Jets orifices	16
2.2	Flow configuration	17
2.3	Experimental results	18
2.3.1	Pressure coefficient	18
2.3.2	Drag coefficient	19
2.3.3	Flow topology and reattachment point	20
2.3.4	Spectral density of velocity	21
2.4	Numerical approach	21
2.4.1	Context and computational resource	22
2.4.2	First assumptions on the numerical technique approach	23
2.4.3	Solver and tools	23
2.4.4	Turbulence models taken in account	23
3	Solution	26
3.1	Computational domain	27
3.2	Turbulent scales of the problem and mesh	28
3.2.1	Reminder about the turbulence scales and the scales in our problem	28
3.2.2	Synthesis of the scales from the current problem	30
3.2.3	Cut-off frequency for the LES subgrid-scale filter	30
3.2.4	Mesh	31
3.3	RANS 2D simulation - uncontrolled case	35
3.3.1	Pressure coefficient results	36
3.3.2	Mean flow topology results	36
3.3.3	Discussion	37
3.4	Global domain simulations - uncontrolled case	37
3.4.1	Boundary conditions	37
3.4.2	Schemes	39
3.4.3	Resolution	39

3.4.4	RANS 3D simulation - Mesh 1 - kwSST	39
3.4.5	RANS 3D simulation - Mesh 2 - kwSST	44
3.4.6	DES 3D simulation - Mesh 1 - kwSST	48
3.4.7	DES 3D simulation - Mesh 2 - kwSST - large time step	54
3.4.8	DES 3D simulation - Mesh 2 - kwSST - smaller time step	60
3.4.9	Discussion	66
3.5	Restrict domain simulations - uncontrolled case	67
3.5.1	Computational domain	67
3.5.2	Mesh	68
3.5.3	Schemes	68
3.5.4	Resolution	68
3.5.5	Boundary conditions	68
3.5.6	DES 3D simulation - Mesh 2 - Sparlat-Allmaras - without inlet synthetic turbulence	71
3.5.7	DES 3D simulation - Mesh 2 - kwSST - without inlet synthetic turbulence	77
3.5.8	DES 3D simulation - Mesh 2 - kwSST - with inlet synthetic tur- bulence	83
3.5.9	Discussion	87
3.6	Restrict domain simulations - controlled case $f/DC=180Hz/50$	88
3.6.1	Computational domain	88
3.6.2	Mesh	88
3.6.3	Schemes	89
3.6.4	Resolution	89
3.6.5	Boundary conditions	89
3.6.6	DES 3D simulation - Mesh 3 - kwSST - with inlet synthetic tur- bulence	89
3.6.7	Discussion	93
4	Results synthesis and conclusion	96
4.1	Results synthesis and methods of computation	97
4.1.1	Methods of computation	97
4.1.2	Topology of the flow - synthesis	100
4.1.3	Gain on the drag coefficient - synthesis	102
4.2	Conclusion and next steps	102

Chapter 1

Introduction

The aim of this internship at the Aerotechnique Institute was to perform a numerical simulation of a study first conducted experimentally by Hlevca *et al.* [5] on the active control applied to the flow past a backward facing ramp. Once the numerical method, turbulence model and mesh used confirmed by a comparison with the experimental results, an investigation of the numerical data was proceeded with a three-dimensional topological view.

1.1 Global context

Flow control is an important research theme in aerodynamics or more generally in fluid dynamics. The important publication on this subject which confirms the efficient of AFC¹ on the diminution or disappearance of flow separation, makes this topic of a strong interest for many industries. Many well-known international conferences are dedicated to it, such as the biennial event of the AIAA² in the United States and the AFCC³ conferences in Germany. This subject is directly linked to the issues of consumption and pollution involving air and noise pollution.

Regarding the automotive industry, the repartition of pressure forces around a vehicle is responsible for 33% of the global drag forces induced in relation to the motion [18], and concerning this pressure force, 30% of the drag effect comes from the rear (figure 1.1).

The gain on the C_x is obtained by applying passive, active open-loop or active closed-loop flow control [5]. Nowadays the reduction of the drag effect is approximately 10 % with active control open-loop applied on academic geometries [3]. Continuous injection or aspiration in the case of active control is relatively efficient but involves too much energy compared with the gain obtained[11]. Periodic injection with two known principal techniques, periodic pulsed jet injection and synthetic jet are alternatively studied. The former limits the mass injection and allows a rigorous control of the blowing time (DC : duty cycle), the latter fully eliminates the debit mass injection.

¹Active Flow Control

²American Institute of Aeronautics and Astronautics

³Active Flow and Combustion Control

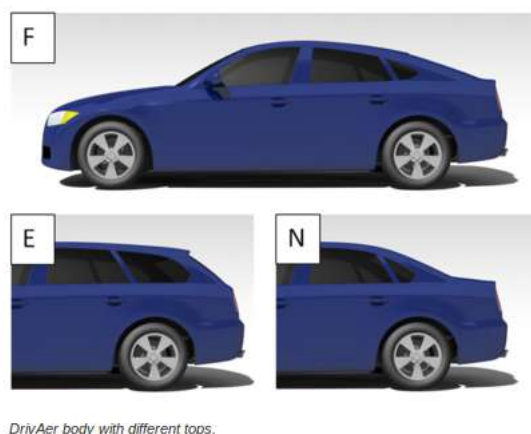


Figure 1.1: C. Leclerc [11], C_x around a vehicle in percent of the total

1.2 Context of the study

We focus on the case of a straight backward facing ramp with a sharp edge and a slant angle of 25° . Applications concerning a priori geometry when shaping optimisations to reduce the drag coefficient are not practicable. This is increasingly the case because mounting demands from car users about the comfort and security will consequently reduce flexibility in geometric aerodynamic arrangements.

This geometry is typically used to model the rear of notchback vehicles and originates from the Ahmed profile.



DrivAer body with different tops.

Figure 1.2: Technical University of Munich, DrivAer Model : F - *Fastback Geometry*; - E - *Estate Back Geometry*; - N - *Notchback Geometry*

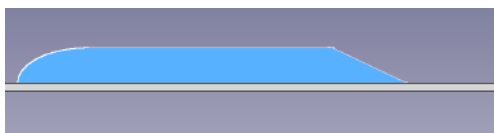


Figure 1.3: Ahmed profile for notchback vehicle - Longitudinal view

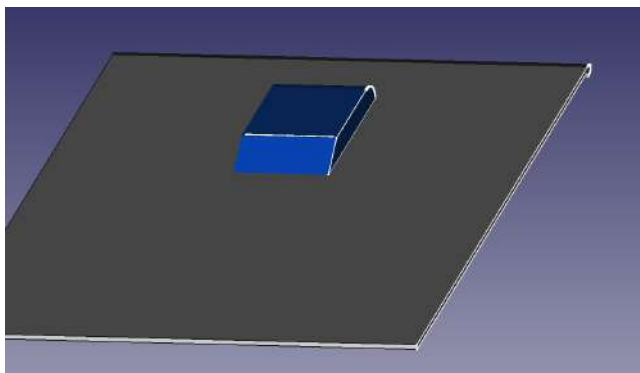


Figure 1.4: Ahmed profile for notchback vehicle - Rear view

1.2.1 Topology of the flow

The mean flow

The mean flow topology behind an Ahmed profile with a backward-facing ramp inclined at 25° is typically constituted by three principal structures linked to the geometry of the profile [22].

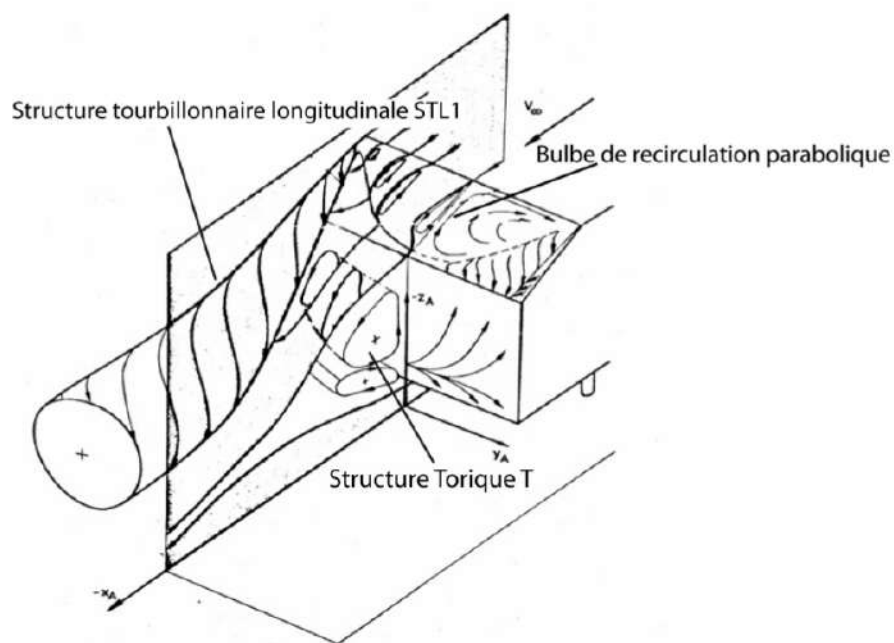


Figure 1.5: Mean flow topology behind an Ahmed profile with a backward facing ramp inclined at 25° [1]

A transversal recirculation bubble is distributed along the span slant, becoming weaker at the edge, pressed near the wall by two longitudinal vortices emanating from the top of the edge.

A recirculation zone also appears at the rear of the lower portion with a toric form. In our study there is no lower portion to be considered. The unique structures appearing are the transversal recirculation bubble and the two longitudinal vortices.

They all generate zones of low pressure, particularly in their centres and are responsible for the drag pressure forces in these areas, the global value of the drag forces depending on the energy and the repartition of these structures.

Concerning the transversal recirculation bubble, the repartition of the pressure at the slant is associated with the separation and the reattachment zone. The pressure values are near the minimum at the separation point and grow until the reattachment point[22].

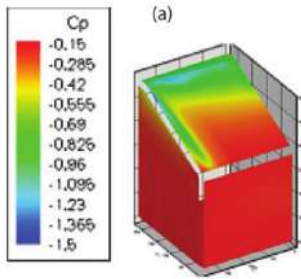


Figure 1.6: Coefficient pressure distribution - Experimental results [12]

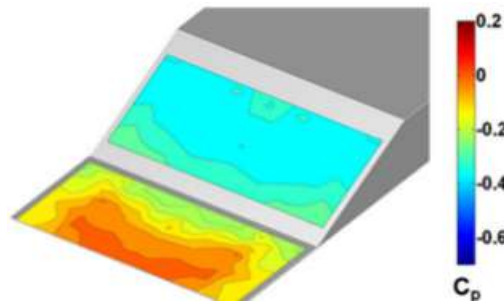


Figure 1.7: Coefficient pressure distribution - Experimental results [9]

Flow fluctuations and non-stationarity

The transversal recirculation bubble is responsible for an important turbulence kinetic energy zone in the vicinity of the separation point extending down to the middle of the slant.

This structure is also strictly unsteady with a low frequency flutter mechanism at the reattachment point [22] ($St_{X_r} = 0.11$ with X_r as the reattachment length). This low frequency phenomenon is also observable on other backward-facing configurations with rupture of the shape's geometry at the separation point similar to the backward-facing step [2].

The position of the longitudinal vortex is relatively stable [22].

1.2.2 Flow control techniques

The aim of flow control in the case of an external flow aerodynamic problem is mainly to act on the coherent structures described above to reduce the drag forces, or improve or recover the lift forces.

The periodic pulsed jets technique described by P. Joseph *et al.* [22], is the AFC technique used in this internship work. This technique allows a strict control of the blowing time and duty cycle. With this feature Hlevca *et al.* [5] consider the question of duty cycles/frequencies combinations influence on the control flow effectiveness.

In general, periodic pulsed jets are numerically modelled as a square signal.

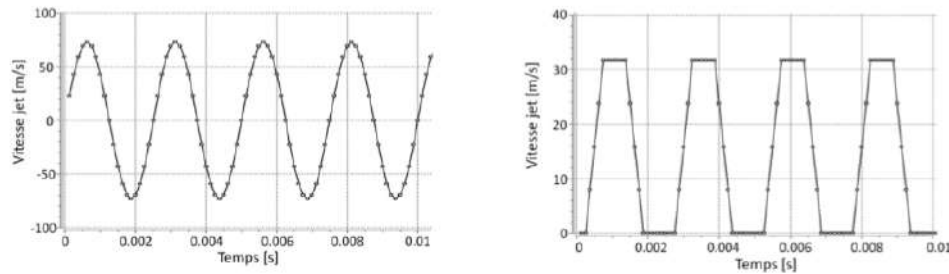


Figure 1.8: Example of numerical jet signal. Left Synthetic jets. Right Pulsed jets. [3]

Periodic pulsed jets generate contra-rotative vortices at the exit of the orifices. On a flat plane, in the mean flow, the upstream flow vortex is reduced by interaction with the vortex of the boundary layer while the downstream vortex increases [11]. This downstream vortex is responsible for a low spike of pressure straight after the jet and mixes high momentum coming from the top of the vortex at deeper levels of the boundary layer [14].

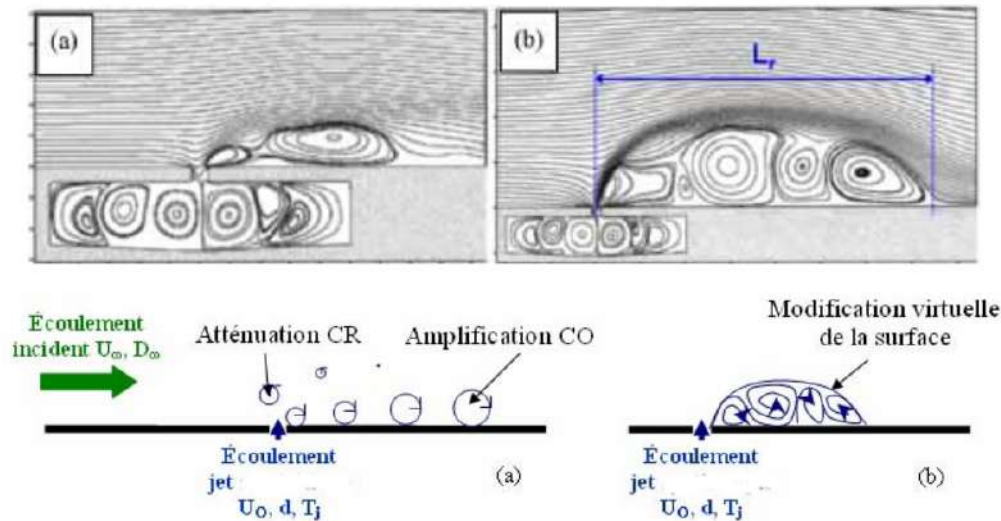


Figure 1.9: Jet vortex formation [11]

Chapter 2

Problem

2.1 Description of the studied geometry and domain

The experimental study that we simulated was carried out in the S4 wind tunnel at the Institut AéroTechnique [5]. The S4 windtunnel has a rectangular section of 5 metres x 3 metres x 10 metres with a maximum freestream velocity of 40 metres per second. The entry turbulence intensity is about 1% and the walls are ventilated to prevent side effects.

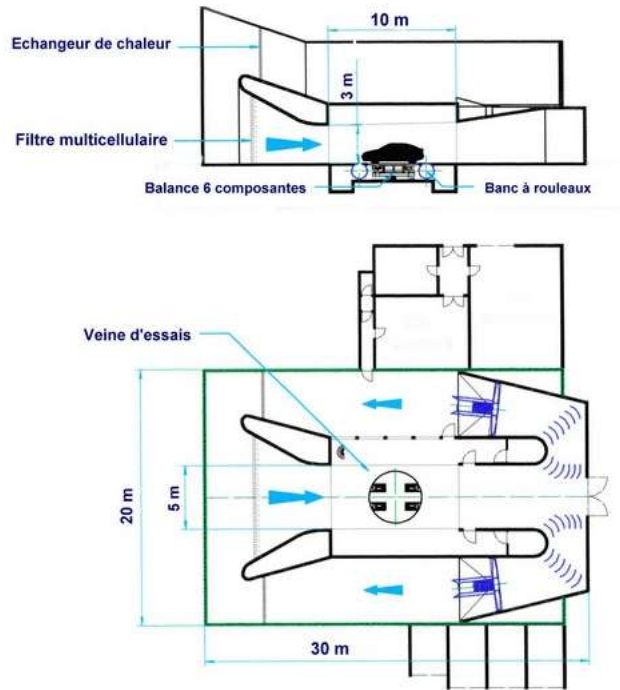


Figure 2.1: IAT's S4 wind tunnel

The numerical design of mechanical parts described below was performed through FreeCAD.

2.1.1 Ramp and its support

The geometry of study is a backward-facing ramp with a finite span and a slant angle of 25° .

The front is set as a half-ellipse with a semi major axis of 187.64 millimetres and a semi minor axis of 93.82 millimetres.

The streamwise length (L), the spanwise extent (W) and the height (H) are respectively $L=1050$ millimetres, $W=389$ millimetres and $H=93.82$ millimetres (see figure 2.2 to 2.3).

The ramp was laid on a support, of which the front consisted of an NACA0018 profile.

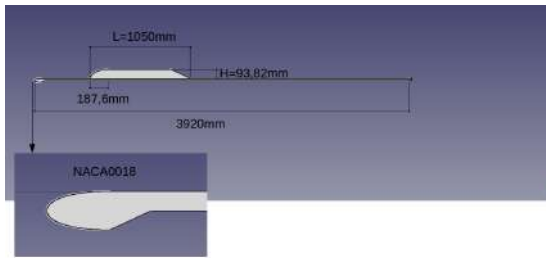


Figure 2.2: Geometrical parameters of the model - Side view

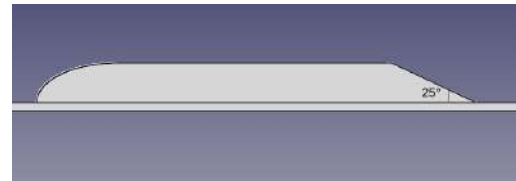


Figure 2.3: Geometrical parameters of the model - Side view

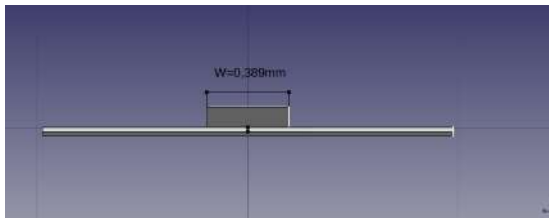


Figure 2.4: Geometrical parameters of the model - Rear view

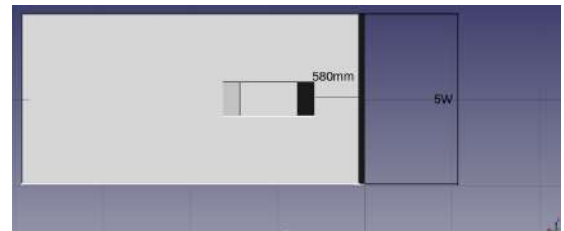


Figure 2.5: Geometrical parameters of the model - Top view

2.1.2 Jets orifices

Eighty-nine orifices are drilled into the ramp through which pulsed jets are injected, directed normal to the mean flow and positioned at 10 millimetres of the sharp edge where separation occurs.

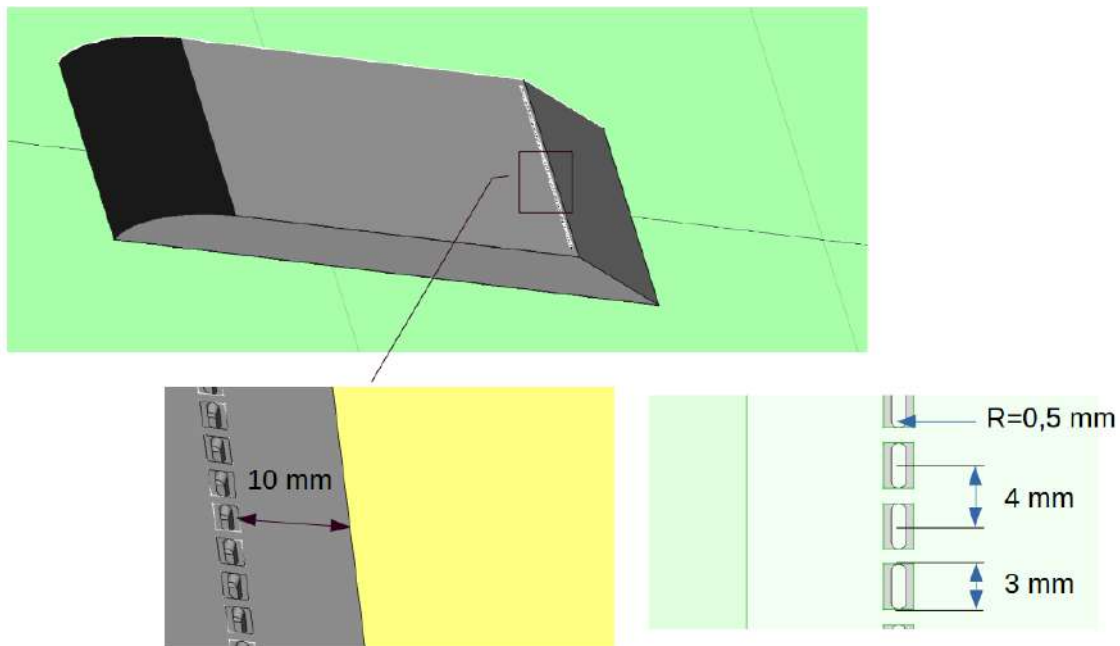


Figure 2.6: Location and dimensions of the jet orifices.

Cavities under the orifices are created to reproduce the pulsed jets expected. We refer to a cavity geometry of a synthetic jet [6] and ensure the formation of jets with numerical tests without mean flow.

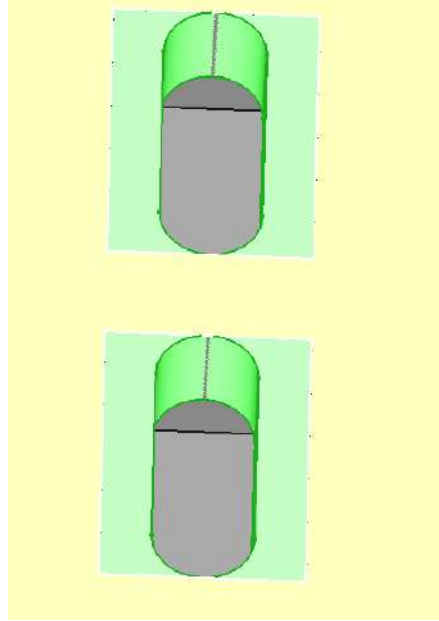


Figure 2.7: Geometry of jet orifices

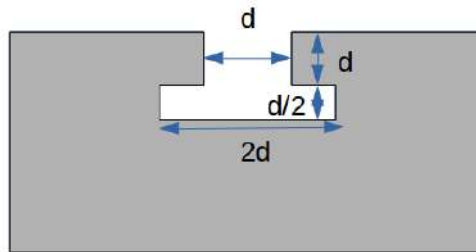


Figure 2.8: Dimensions of jet orifices

2.2 Flow configuration

The experimental study [5] sweeps three different Reynolds numbers. We focused on the intermediary one : $Re_L = 2.35 \cdot 10^6$ or $Re_H = 210380$.

We consider a developed turbulence at the inlet at the intensity order of the S4 wind-tunnel's features.

The wind-tunnel walls are ventilated so that we can consider those regions as slip boundary conditions.

The flow is assumed to be incompressible.

All the global scales of the current problem are given in the figure below 2.9.

Global scales of the flow	
Reference velocity U_{∞} in m/s	30
Reference length L in m	1,05
Reference length H in m	0,09392
Reference length W in m	0,389
Reference time T_L in s	3,50E-02
Reference time T_H in s	3,13E-03
Reference time T_W in s	1,30E-02
Reference frequency f_L in Hz	28,57142857
Reference frequency f_H in Hz	319,4207836
Reference frequency f_W in Hz	77,12082262
Reference in St_H for f_L	0,089447619
Reference in St_H for f_H	1
Reference in St_H for f_W	0,241439589
Kinematic viscosity in m^2/s	1,34E-05
Re_L	2,35E+06
Re_H	2,10E+05

Figure 2.9: Global scales from the current problem

2.3 Experimental results

The results reported in this section are from the baseline experimental study [5] -and are those we will focus on to compare the numerical ones. The objective of this section is not to discuss the results obtained experimentally (see [5] for that) but to display the data we consider the basis of our numerical study. The first case corresponds to the uncontrolled flow, the second one to applied pulsed jets at the frequency and duty cycle $f_i/DC_i = 180/50$.

2.3.1 Pressure coefficient

The pressure coefficient is given by the following equation :

$$C_{p_i} = 2 \frac{(p_i - p_{\infty})}{\rho_{\infty} U_{\infty}^2}$$

We based our comparison of the experimental data pressure curves on the longitudinal middle plane along the shape.

It is important to note at this step that there is no experimental pressure tape on a narrow vicinity of the jet orifices and there is no pressure tape on the top slant near

the geometry discontinuity and the flow separation point.

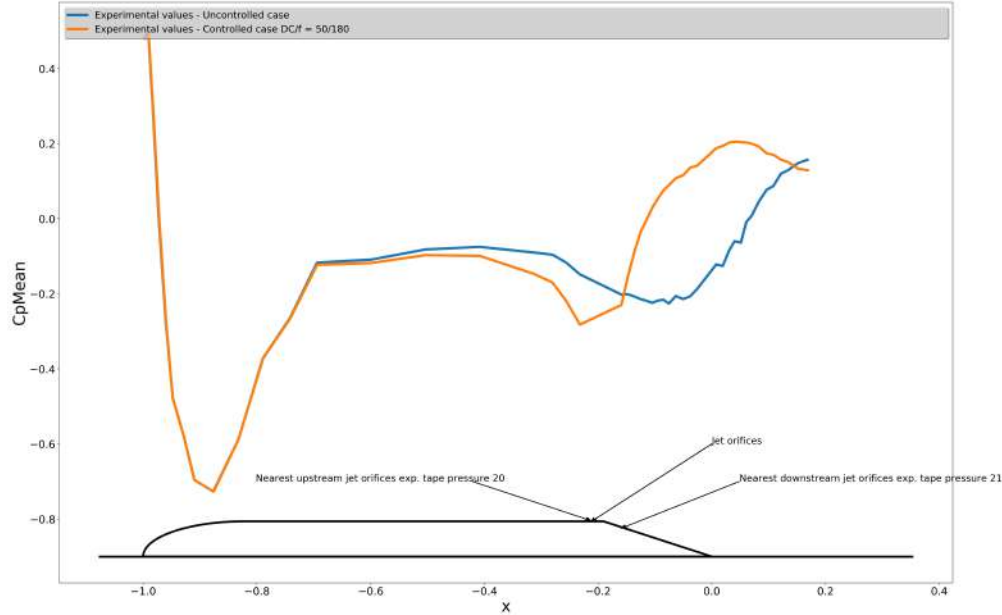


Figure 2.10: Pressure coefficient - middle plane $z=0$ - experimental data - uncontrolled case and controlled case $f_i/DC_i = 180/50$

2.3.2 Drag coefficient

As a result of the pressure experimental tapes' location exclusively in the symmetric middle plane, the deduction of the drag coefficient is not possible. These authors [5] obtained an estimation of it with the following formulation, extrapolating the value of the pressure from the middle plane all over the spanwise of the slant.

$$C_D = - \frac{\sum_{i \text{ over-slant-surface}} C_{p_i} \Delta S_i}{HW}$$

$Re_L \cdot 10^{-6}$		C_D			
Uncontrolled flow		Controlled flow			
1.56	0.1967	0.0075(A_{11})	0.0004(A_{12})	-0.0048(A_{13})	-0.0138(A_{14})*
2.35	0.2060	0.0332(A_{21})	0.0094(A_{22})	0.0026(A_{23})*	0.0053(A_{24})
3.13	0.2140	0.0746(A_{31})	0.0467(A_{32})	0.0283(A_{33})	0.0211(A_{34})*

Figure 2.11: Estimation drag coefficient on the slant - experimental data - uncontrolled case and controlled case - see : [5]

2.3.3 Flow topology and reattachment point

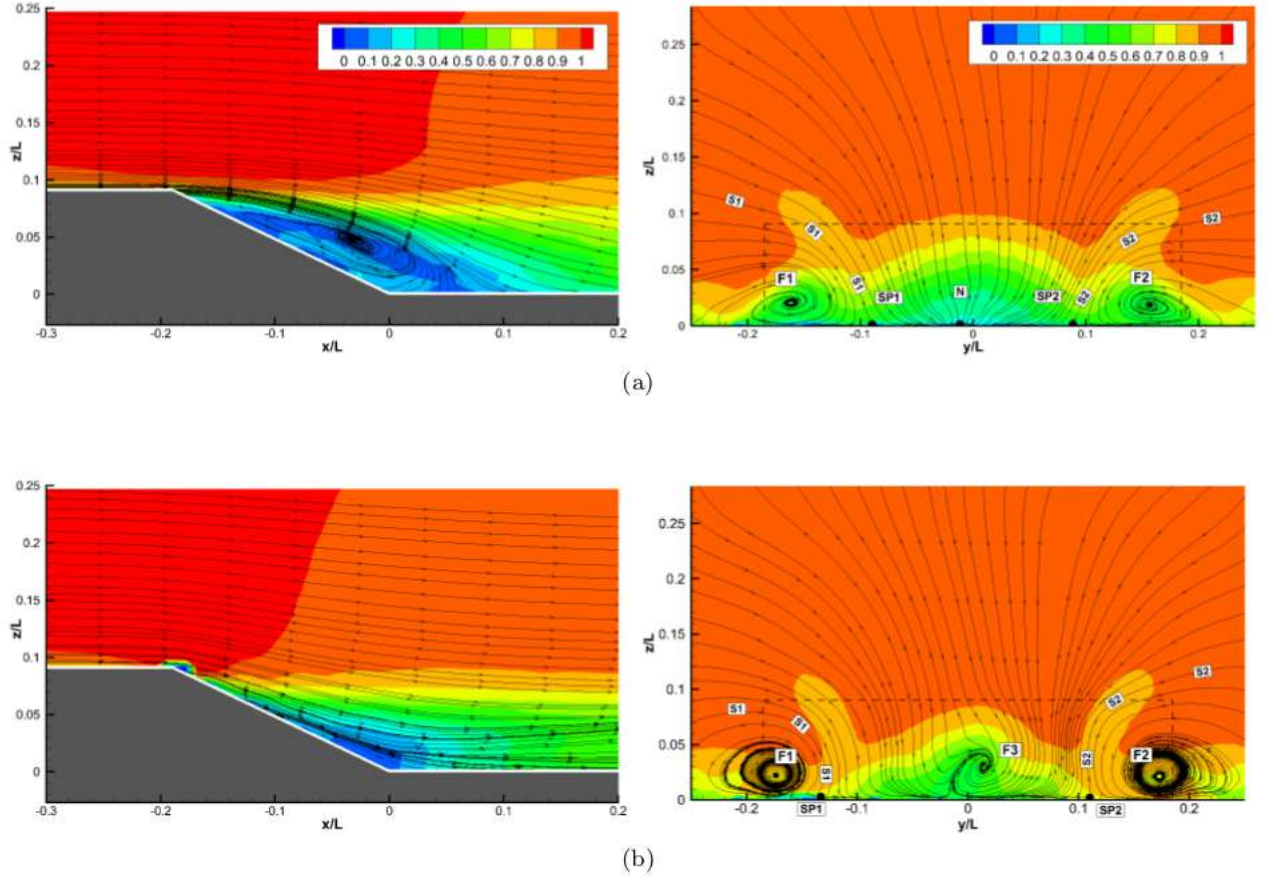


Figure 2.12: Streamline mean adimensional velocity magnitude experimental data - longitudinal middle plane $z/L=0$ left - transversal plane $x/L=0.137$ right- (a) uncontrolled case - (b) controlled case $f_i/DC_i = 180/50$ [5]

We can observe figure 2.12 (a) left, the typical recirculation bubble discussed chapter 1.2.1 at the rear after the detachment point corresponding to the spot of the acute angle.

In the controlled case $f_i/DC_i = 180/50$, this structure disappears almost completely with a reattachment of the flow.

The reattachment point corresponding to the spot where the shear stress at the wall is equal to zero.

$$\tau_p = \mu \left(\frac{\partial u_x}{\partial y} \right)_{reattachment} = 0$$

We notice also on the right figures 2.12 the typical longitudinal vortex reinforced in case of control [9][5].

2.3.4 Spectral density of velocity

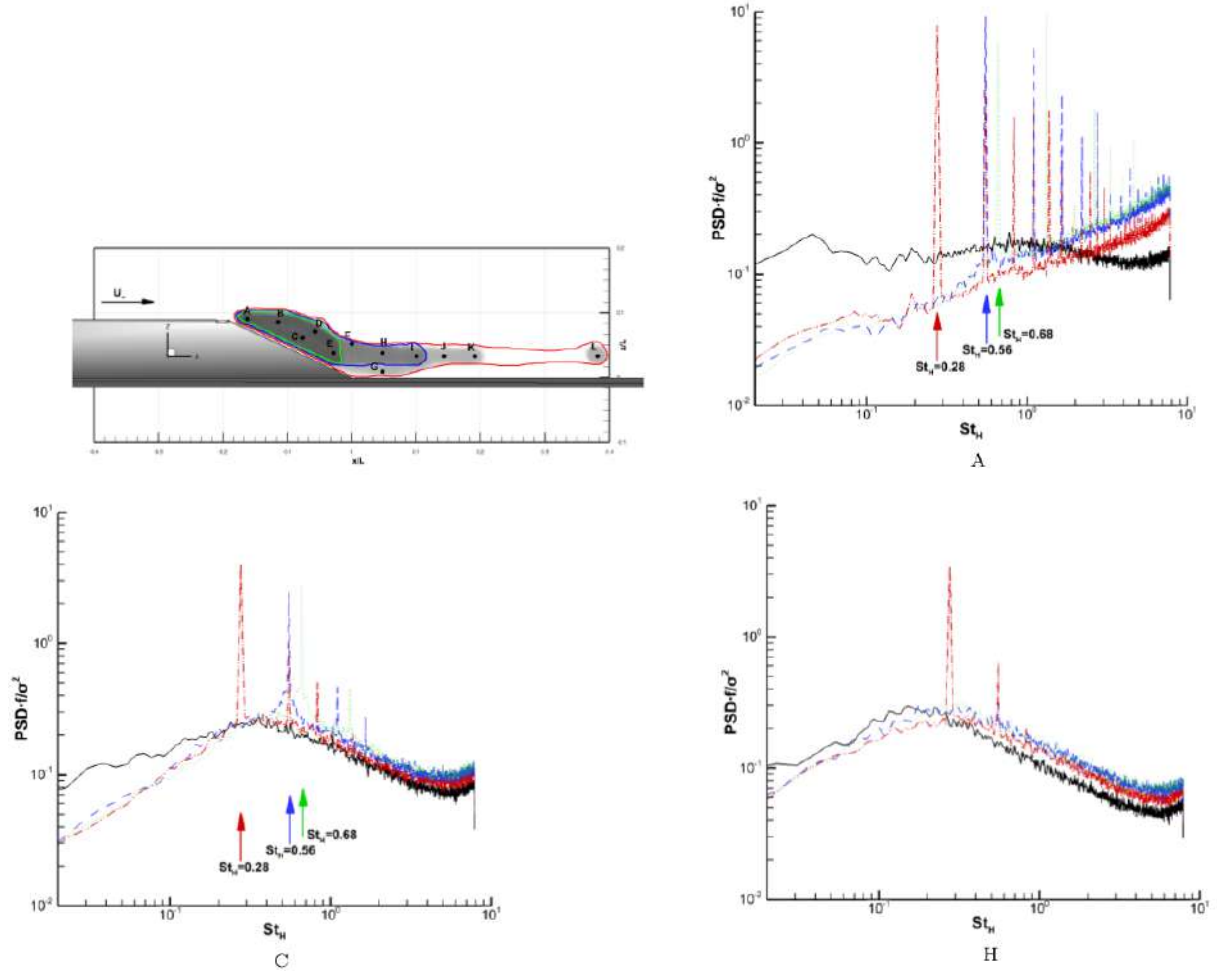


Figure 2.13: Normalised power spectral density of the velocity signal at points A,C,H - *Solid black line*, uncontrolled case; *dashed blue line*, controlled case $f_i/DC_i = 180/50$ - *Other*, other cases - *Figure extracted from [5]*

These results give us an initial impression of the time-frequency range scales of the turbulent structures that have to be simulated. The most energetic are situated in a range of Strouhal number of $8 \cdot 10^{-2} < St_H < 1$ (see all the experimental spectrum in [5]).

2.4 Numerical approach

Numerical simulations for backward-facing ramp or other types of geometries that are similar, with AFC control applied have been done frequently with different numerical techniques.

Pamart *et al.* [15] studied a rounded facing ramp with the synthetic jets technique approach at $Re_H = 30000$. These authors used an LES method on a restricted domain

focussed on the step. Influence of frequency on variate criteria such as reattachment point, separation length, separation area is analysed. In his doctoral thesis, Eulalie [3] simulates the flow around an Ahmed profile with a straight rear part with pulsed jets technique approach at $Re_H = 402000$. He used a DES-Spalart-Almaras on the wind tunnel's whole domain with FEM discretisation. Zhao Guoqing *et al.* [4] were interested in instabilities and AFC over rotor airfoil. The numerical method used in this paper is a URANS k- ω SST modelling, and the authors seem to obtain results without using LES. Furthermore, Bhanu Prakash *et al.* [17] performed a DNS simulation of a flow over an Ahmed body.

2.4.1 Context and computational resource

The behaviour of the flow in our study is essentially unsteady, including the mean flow's structures developed at the rear of the ramp inducing low frequency mechanism, forcing us to proceed computations over long period of time - as we will see over than 10 - 15 T_L (T_L being the flow-through time).

Furthermore, the discontinuity of the geometry at the location of the acute angle induces a vast separation zone in the flow past the ramp which must be considered with a good mesh accuracy and an adapted turbulent model.

Another important parameter that must be considered is the computer mean and the computational power we have. The simulations are achieved on a Ubuntu server with 16 processors each set to run at 2.10 GHz. With an assumption of 4 flops par cycle, we dispose of approximately 130 gigaFLOPS. All the processing power can be dedicated to this numerical study. The RAM is about 32 Go.

If we compare with a similar problem studied by Pamart *et al.* [15] in 2010, they disposed of two units of a NEC SX-8 server, that is 256 gigaFLOPS and 256 Go of RAM. The study was limited at the rear of the ramp with a span extension considered endless and probably periodic boundary conditions on the sides. So that, the three dimensional effect of a finite span were not considered (the two longitudinal vortices). They reach the solution of the mean flow in 2 flow-through times.

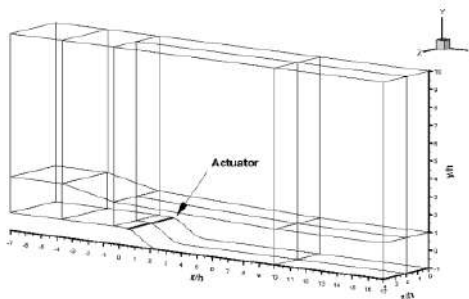


Figure 2.14: Pamart domain of calculation see : [15]

We had to compute a domain approximately ten times bigger, a compute time to consider also ten bigger with less than two time less computational resources. Our

computational features were therefore quite restrictive for this problem and the time we dedicate for this work. We had to find an adapted simulation strategy.

2.4.2 First assumptions on the numerical technique approach

We had to calculate the finest coherent structures that can interact in the separation zone especially with active flow controlled applied and were inclined to use LES methods. Particularly limited by the computational resources, we did not have enough points in the boundary layers and the shear layer to converge toward a good representation of the physical solution.

Therefore we tended to use DES methods which use URANS calculations near the wall and LES elsewhere.

The domain that had to be simulated to near-exactly represent the experimental study is quite vast. DES calculation for the controlled-case with sufficient accuracy of the locations of interest was unfeasible all over this domain with our limited computer resources and time. Therefore we attempted to split the simulation into two parts. The first part consisted of proceeding a RANS/DES computation on the whole area to define the further entry boundary conditions for the second part corresponding to a more accurate DES simulation on a limited region.

Danet [2] was interested by the inflow conditions of a mixed RANS-LES simulation in the case of a backward-facing-step flow and synthesised different techniques. Immer also [7] describes, in his doctoral thesis, the current methods allowing turbulent inflow boundary conditions. This subject is expanded in the chapter dedicated to the DES calculation (see section 3.5.5)

2.4.3 Solver and tools

OpenFOAM was chosen as CFD solver because of its costless acquisition reliability and extended use. This solver is based on a finite volume discretization method (FVM). The version used is the last one at the time of writing this work, the 1806.

The CAO tool used was FreeCAD version 0.16. The automation of the object generation with geometric variations was made with the FreeCAD macro in Python.

Python, Jupyter Notebook and Paraview were used for the pre- and post-treatment data analyses.

2.4.4 Turbulence models taken in account

A multitude of turbulence models were implemented in OpenFOAM. We focussed on affordable a priori ones in regard to the burden of computation. We therefore considered exclusively eddy-viscosity models. The following models that could potentially be adapted to our case, with a wall problematic and strong separation zone, have been tested in the context of this work :

Sparlat Allmaras' eddy-viscosity model [19] is based on one equation modelling for the turbulent viscosity ν_t . An 'empirical' transport equation (not originated from the rigorous transport equation of the Reynolds stress components) was designed by the authors with all its components, which, for $\tilde{\nu}$ defined a viscosity respecting the log layer rules all the way to the wall ($\nu_t = \tilde{\nu} \frac{X^3}{X^3 + c_{\nu 1}^3}$ with $X = \kappa y^+$):

- the Lagrangian derivative

$$\frac{D\tilde{\nu}}{Dt} \quad (1),$$

- a production term

$$c_{b1}[1 - f_{t2}]\tilde{S}\tilde{\nu} \quad (2),$$

- a diffusion term

$$\frac{1}{\sigma}[\nabla \cdot ((\nu + \tilde{\nu})\nabla \tilde{\nu}) + c_{b2}(\nabla \tilde{\nu})^2] \quad (3),$$

- a near wall region and laminar region destruction term

$$- \left[c_{w1}f_w - \frac{c_{b1}}{\kappa^2} \right] \left[\frac{\tilde{\nu}}{d} \right]^2 \quad (4),$$

- a trip term

$$f_{t1}\Delta U^2 \quad (5),$$

$$\frac{D\tilde{\nu}}{Dt} = c_{b1}[1 - f_{t2}]\tilde{S}\tilde{\nu} + \frac{1}{\sigma}[\nabla \cdot ((\nu + \tilde{\nu})\nabla \tilde{\nu}) + c_{b2}(\nabla \tilde{\nu})^2] - \left[c_{w1}f_w - \frac{c_{b1}}{\kappa^2} \right] \left[\frac{\tilde{\nu}}{d} \right]^2 + f_{t1}\Delta U^2$$

This model is adapted for DES calculations [20] (development of DES method is based on the Sparlat Allmaras turbulence model and had been initiated by these authors) and allowed a priori relatively weakest costs of calculation (only one more equation to solve for the modelling of turbulence) compared to a more classical two equations model.

Choosing d as the minimum length between the distance from the wall and the length local grid mesh $\min(d, C_{DES}\Delta)$ (CDES is an adjustable model constant) - d corresponds to the length turbulence scale which is modelled - allows the destruction term (4) to cut the value of the turbulent viscosity under a value related to the dimension of the mesh and so permits LES simulation on the regions far from walls. The DES computation is globally no more expensive than a URANS technique and gives better predictions in separation zones.

$k - \omega$ SST eddy-viscosity model [13] is a two equations model, a composite of the classical $k - \epsilon$ and $k - \omega$. The $k - \epsilon$ works well far from walls but becomes problematic when determining the correct turbulence length scale near the wall. In contrast $k - \omega$ gives good predictions in terms of turbulence length scale near the wall but is unsuitable for use on free stream regions. The $k - \omega$ SST takes advantage of the two models,

allowing $k - \omega$ modelling near the wall and $k - \epsilon$ in the free stream regions.

$$\begin{aligned}\frac{D\rho k}{Dt} &= \tilde{P}_k - \beta^* \rho \omega k + \frac{\partial}{\partial x_j} \left(\Gamma_k \frac{\partial k}{\partial x_j} \right) \\ \frac{D\rho \omega}{Dt} &= \frac{\gamma}{\nu_t} P_k - \beta^* \rho \omega^2 + \frac{\partial}{\partial x_j} \left(\Gamma_\omega \frac{\partial \omega}{\partial x_j} \right) + (1 - F_1) 2\rho \sigma_{\omega 2} \frac{1}{\omega} \frac{\partial k}{\partial x_j} \frac{\partial \omega}{\partial x_j}\end{aligned}$$

Each term for each equation respectively corresponds to the material derivate, a production term, a destruction or dissipative term and a diffusion term, with $(1 - F_1) 2\rho \sigma_{\omega 2} \frac{1}{\omega} \frac{\partial k}{\partial x_j} \frac{\partial \omega}{\partial x_j}$ whose function is to ensure the link between the $k - \epsilon$ and $k - \omega$ models.

This model is known as one of two-equation RANS models that provide accurate results for separation flow prediction. The length turbulence scale is calculated through the modelling of ω or ϵ . In the Sparlat Allmaras model, this length is a priori given by the distance from the wall. In case of flow separation, it could be overestimated.

DES computation with a $k - \omega$ *SST* model has been done by [21]. The turbulent length scale is either calculated by $l_{k-\omega} = k^{\frac{1}{2}}/(\beta^* \omega)$ or corresponds to the dimension of the local mesh :

$$\tilde{l} = \min(l_{k-\omega}, C_{DES} \Delta)$$

With the Sparlat Allmaras DES technique, the destruction term increases with a diminution of the length scale, but, far from the wall, in case a mesh's dimension is greater than the turbulence scale, RANS computation is done instead of LES. Therefore, this model should give best results in the separation zone as the Sparlat Allmaras DES technique does for relatively coarse mesh.

Chapter 3

Solution

3.1 Computational domain

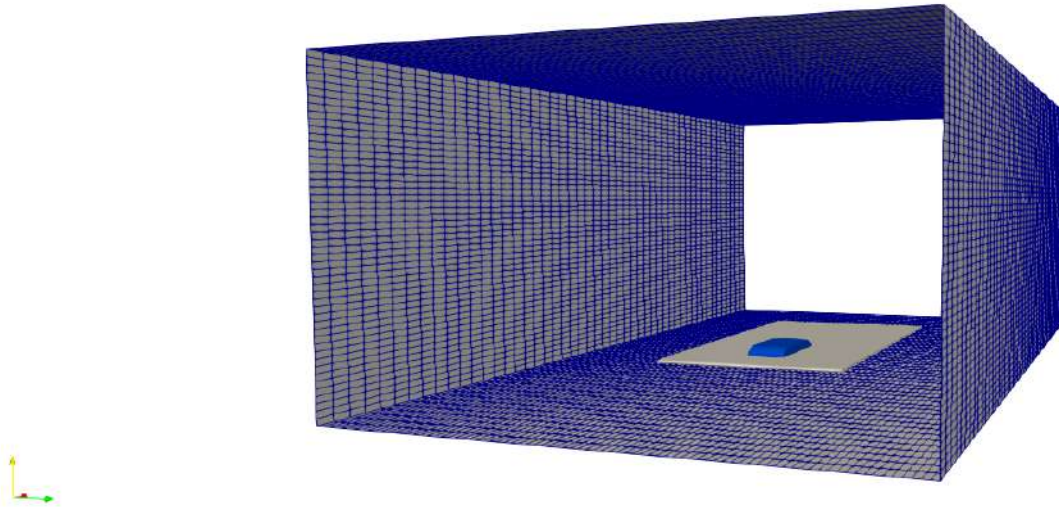


Figure 3.1: Computational domain - wintunnel wall

We considered the test wind tunnel section as a rectangular 5 metres x 3 metres x 10 metres duct. The support's nose is placed at a distance of 3.25 metres from the inlet and 0.17 metres from the duct's ground (see figure 3.2 to 3.3).

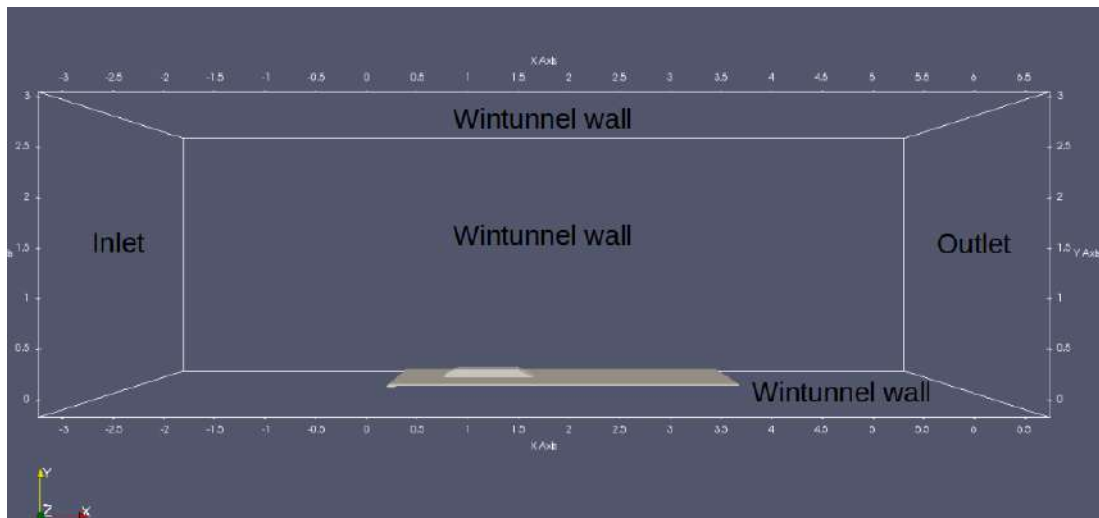


Figure 3.2: Domain and ramp's disposition in metres - side view

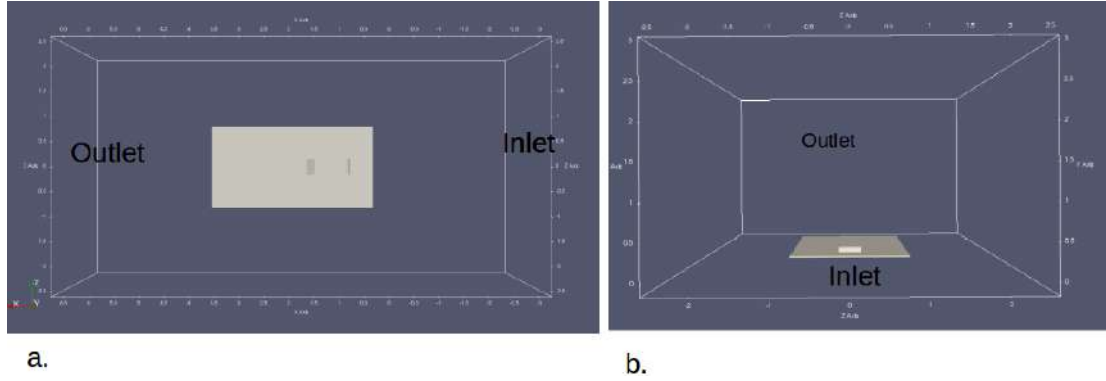


Figure 3.3: Domain and ramp's disposition in metres - a. top view - b. front view

3.2 Turbulent scales of the problem and mesh

To conceive a mesh related to the flow of the current problem that responds to our needs (not to modelling) the turbulence lengthscales susceptible to enter in interaction with the structures generated by the impulsed jets, we proceeded with an estimation of the scales from our studied case.

3.2.1 Reminder about the turbulence scales and the scales in our problem

See [16] for detailed concept.

The first important concept for fully developed turbulent flows is the energy cascade. That is, kinetic energy enters the turbulence at the largest scales and is transferred progressively to the smaller until the energy is dissipated by the viscosity.

This energy cascade is linked with eddies of different sizes l , each with a distinct characteristic velocity $u(l)$ and timescale $\tau(l) = \frac{l}{u(l)}$. The Reynolds number of these eddies $Re(l) = u(l)l/\nu$ is assumed to decrease from $Re_0 = u_0 l_0/\nu$ (Re_0 being the Reynolds number of the most energetic structures) with the decreasing of length l to reach a value where the viscosity is dominant and so too are the dissipative actions.

The largest eddies can be characterised by the length scale l_0 in the order of the flow scale L with their characteristic velocity $u_0 = u(l_0)$. **In our case**, $L = 1.05m$, $l_0 = H = 0.0939m$ and $u_0 = U_\infty = 30m/s$.

The energy assumed to be transferred and dissipated is from the largest structures so that the dissipation rate can be evaluated with the present defined scale $\epsilon = u_0^3/t_0 = u_0^3/l_0$. **In our case**, $\epsilon = 2.87 \times 10^5 \text{ Watt.kg}^{-1}$.

At this point we are not able to characterised the smaller scales under l_0 and the behaviour of $u(l)$ and $\tau(l)$ with the decrease of l . For that, we need to consider the three hypotheses of Kolmogorov.

The first hypothesis of Kolmogorov states that at *sufficiently high Reynolds number*, the *small-scale turbulent motions* ($l \ll l_0$) are statistically isotropic.

If we call l_{EI} (with $l_{EI} \approx \frac{1}{6}l_0$) the lengthscale defining the demarcation between the anisotropic large eddies and the isotropic small eddies, we can say that in the zone $l < l_{EI}$ all information of the geometry of the large eddies and the problem is lost and the behaviour of the eddies is universal. **In our case** $l_{EI} = 1.57 \times 10^{-2}$ m.

At this point, assuming that the statistical universal state depends only on the rate of energy received from the large scales $\Gamma_{EI} \approx \epsilon$ and the viscous dissipation ν the first Kolmogorov's similarity hypothesis can be enunciated *in every turbulent flow at a sufficiently high Reynolds number, the statistics of the small-scale motion* ($l < l_{EI}$) *have a universal form that is, uniquely determined by ν and ϵ .*

The typical Kolmogorov scales can then be defined as the following :

$$\begin{aligned}\eta &= (\nu^3/\epsilon)^{1/4}, \\ u_\eta &= (\epsilon\nu)^{1/4}, \\ \tau_\eta &= (\nu\epsilon)^{1/2}.\end{aligned}$$

Or with $\epsilon \approx u_0^3/l_0$:

$$\begin{aligned}\eta/l_0 &\approx Re^{-3/4}, \\ u_\eta/u_0 &\approx Re^{-1/4}, \\ \tau_\eta/\tau_0 &\approx Re^{-1/2}.\end{aligned}$$

In our case :

$$\begin{aligned}\eta &\approx l_0 \times Re_{l_0}^{-3/4} = 9.58 \times 10^{-6}m, \\ u_\eta &\approx u_0 \times Re_{l_0}^{-1/4} = 1.4m/s, \\ \tau_\eta &\approx \tau_0 \times Re_{l_0}^{-1/2} = 6.84 \times 10^{-6}s.\end{aligned}$$

Assuming now that there is a rang in the universal zone sufficiently far from the dissipation rang, that is, $\eta \ll l \ll l_0$ where the length scale of eddies is large enough to neglect the viscosity effect, we can write the Kolmogorov's second similarity hypothesis : *in every turbulent flow at a sufficiently high Reynolds number, the statistics of the motions of scale l in the range $\eta \ll l \ll l_0$ have a universal form that is uniquely determined by ϵ and independent of ν .*

Introducing l_{DI} with $l_{DI} = 60\eta$, we can define a demarcation in the universal equilibrium range between a dissipation range and an inertial range.

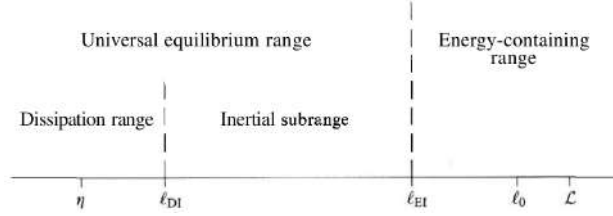


Figure 3.4: Stephen B. Pope : Various length scales and ranges

In the inertial zone, we can now characterised the velocity and time scale function of ϵ and l .

$$\begin{aligned} u(l) &= (\epsilon l)^{1/3} = u_\eta (l/\eta)^{1/3} \approx u_0 (l/l_0)^{1/3}, \\ \tau(l) &= (l^2/\epsilon)^{1/3} = \tau_\eta (l/\eta)^{2/3} \approx \tau_0 (l/l_0)^{2/3}. \end{aligned} \quad (3.1)$$

3.2.2 Synthesis of the scales from the current problem

Global scales of the flow	
Reference velocity U_∞ in m/s	30
Reference length L in m	1,05
Reference length H in m	0,09392
Reference length W in m	0,389
Reference time T_L in s	3,50E-02
Reference time T_H in s	3,13E-03
Reference time T_W in s	1,30E-02
Reference frequency f_L in Hz	28,57142857
Reference frequency f_H in Hz	319,4207836
Reference frequency f_W in Hz	77,12082262
Reference in St_H for f_L	0,089447619
Reference in St_H for f_H	1
Reference in St_H for f_W	0,241439589
Kinematic viscosity in m^2/s	1,34E-05
ReL	2,35E+06
ReH	2,10E+05

Global turbulence scales	
Kolmogorow length η in m	9,58E-06
Kolmogorow velocity u_η in m/s	1,40E+00
Kolmogorow time scale τ_η in m/s	6,84E-06
Reference turbulente length scale $l_0 = H$ in m	9,39E-02
Reference turbulent velocity $u_0 = U_\infty$ in m/s	3,00E+01
Reference turbulente time scale τ_0 in s	3,13E-03
Demarcation length between anisotropic large eddies and isotropic small eddies $l_{EI} = l_0/6$ in m	1,57E-02
Reference dissipative length l_{DI} in m	5,75E-04
Rate of dissipation ϵ in W/kg	2,87E+05

Figure 3.5: Scales from the current problem

3.2.3 Cut-off frequency for the LES subgrid-scale filter

The question is now which is the correct length of mesh that respond to our need to obtain a correct numerical solution with and without AFC applied ? Moreover, what is the cut-off frequency to consider for the LES filter in the subgrid scale ? We focus on this issue particularly at the rear of the ramp where the mixing layer occurs and the impulsed jets have effects.

We have to capture the coherent energetic structures linked with the geometry of the problem more precisely, where the turbulence is not universal and not in measure to be picked up by a first-order turbulence model. That is, the mesh has to be at least inferior at l_{EI} .

3.2.4 Mesh

Three different types of mesh with the same global topology but with differences in accuracy were used for the simulations. This allowed us to see the influence of accuracy linked to the mesh on the resulted solutions; the last mesh was dedicated for the controlled case and the presence of jet orifices.

Mesh 1 : The first mesh is constituted as follow :

Numner of points = 16 907 856	Zone 1	Zone 2	Zone 3	Zone 4	Zone 5	Boundary layers
Δx in mm	1,00E-01	5,00E-02	2,50E-02	1,25E-02	6,25E-03	6,25E-03
Δy in mm	3,00E-02	1,50E-02	7,50E-03	3,75E-03	1,88E-03	9,38E-04
Δz in mm	3,13E-02	1,56E-02	7,81E-03	3,91E-03	1,95E-03	1,95E-03
$< \text{LeI}$	No	No	No	Yes	Yes	Yes
Type of calculation	URANS	URANS	URANS	LES	LES	URANS

Figure 3.6: Mesh 1 : Length scale in the different zones

Reference scales of the smallest eddies calculated	
Smallest subgrid length scale in m	6,25E-03
Smallest time scale in s	5,14E-04
Smallest eddies velocity scale in m/s	1,22E+01
Highest Strouhal number	6,089552482
Highest frequency in 1/s	1,95E+03

Figure 3.7: Mesh 1 : Smallest length scale

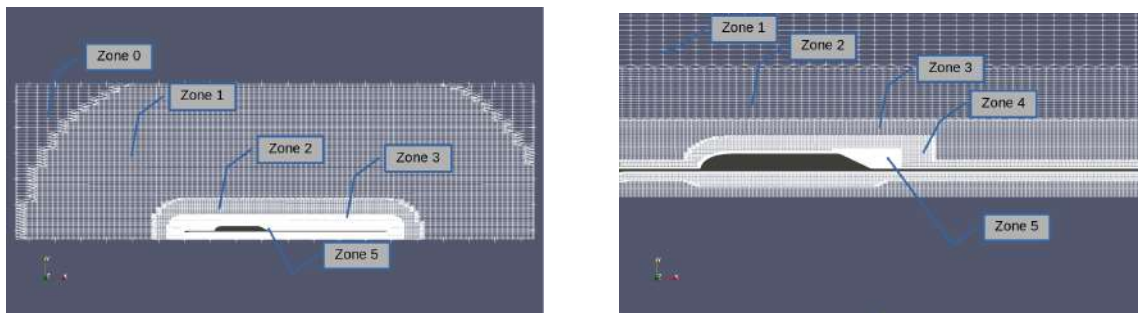
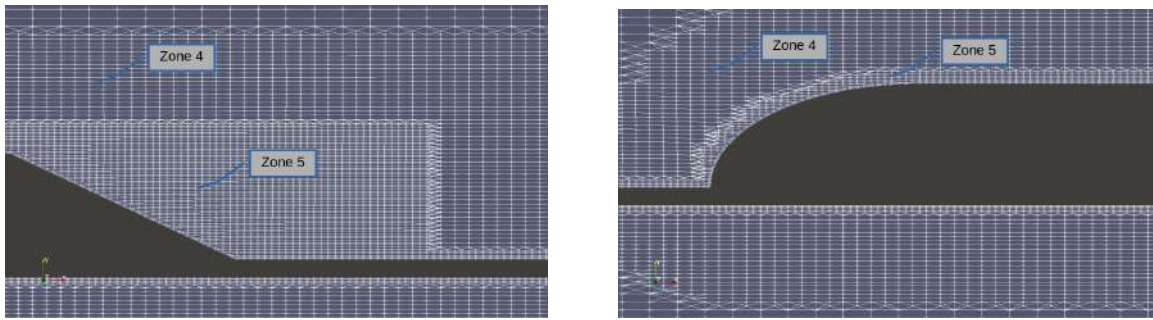
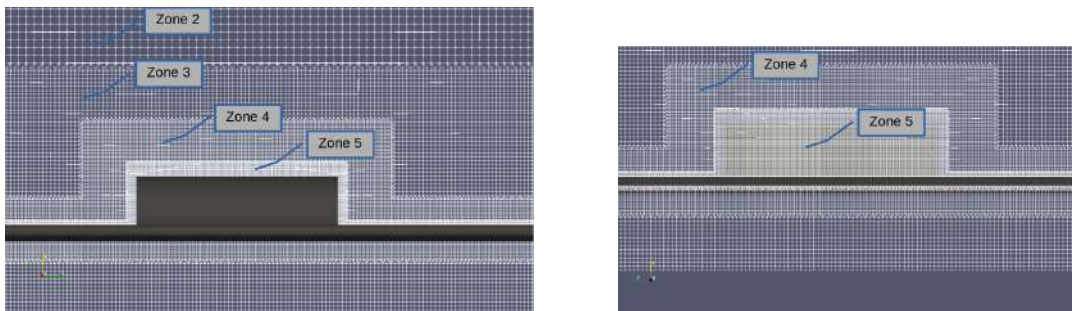
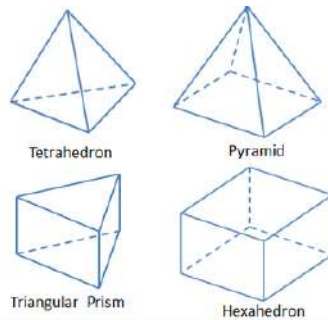


Figure 3.8: Mesh 3D mesh 1 - middle plane $z=0$

Figure 3.9: Mesh 3D mesh 1 - middle plane $z=0$ Figure 3.10: Mesh 3D mesh 1 - plane $x=1$ m and $x=1,77$ m

Mesh quality : The mesh is of good quality with mostly hexahedral cells.



hexahedra: 14931950,
prisms: 25260,
pyramids: 0,
tetrahedra: 0,
polyhedra: 505482,

and mostly orthogonal:

Mesh non-orthogonality max: 84.68141 degrees average: 9.568813 degrees,
Number of severely non-orthogonal (> 70 degrees) faces: 1974.

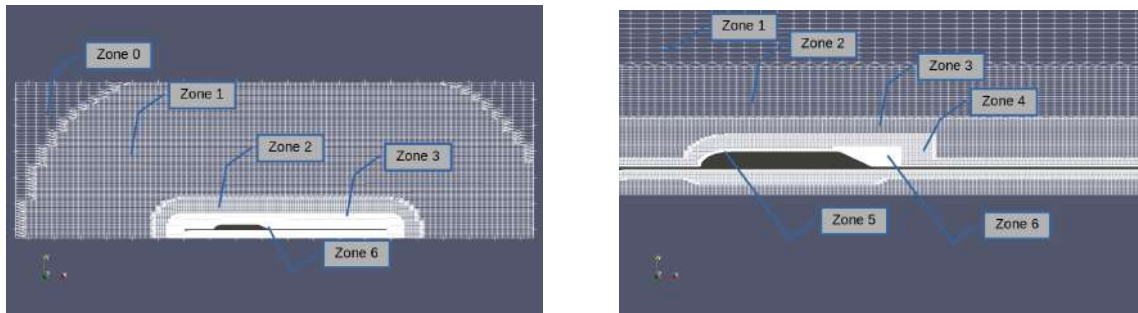
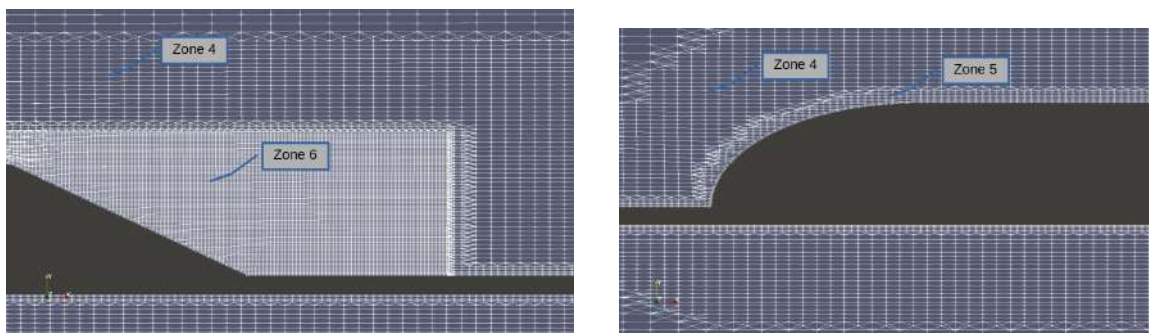
Mesh 2 : The more refined mesh is constituted as follow, where the difference with the first one resided in the refinement of zone 5 in zone 6 at the rear of the profile :

Nunmer of points = 21 960 270	Zone 1	Zone 2	Zone 3	Zone 4	Zone 5	Zone6	Boundary layers
Δx in mm	1,00E-01	5,00E-02	2,50E-02	1,25E-02	6,25E-03	3,13E-03	6,25E-03
Δy in mm	3,00E-02	1,50E-02	7,50E-03	3,75E-03	1,88E-03	9,38E-04	9,38E-04
Δz in mm	3,13E-02	1,56E-02	7,81E-03	3,91E-03	1,95E-03	9,77E-04	1,95E-03
< l_{EI}	No	No	No	Yes	Yes	Yes	Yes
Type of calculation	URANS	URANS	URANS	LES	LES	LES	URANS

Figure 3.11: Mesh 2 : Length scale in the different zones

Reference scales of the smallest eddies calculated	
Smallest subgrid length scale in m	3,13E-03
Smallest time scale in s	3,24E-04
Smallest eddies velocity scale in m/s	9,65E+00
Highest Strouhal number	9,666562015
Highest frequency in 1/s	3,09E+03

Figure 3.12: Mesh 2 : Smallest length scale

Figure 3.13: Mesh 3D mesh 2 - middle plane $z=0$ Figure 3.14: Mesh 3D mesh 2 - middle plane $z=0$

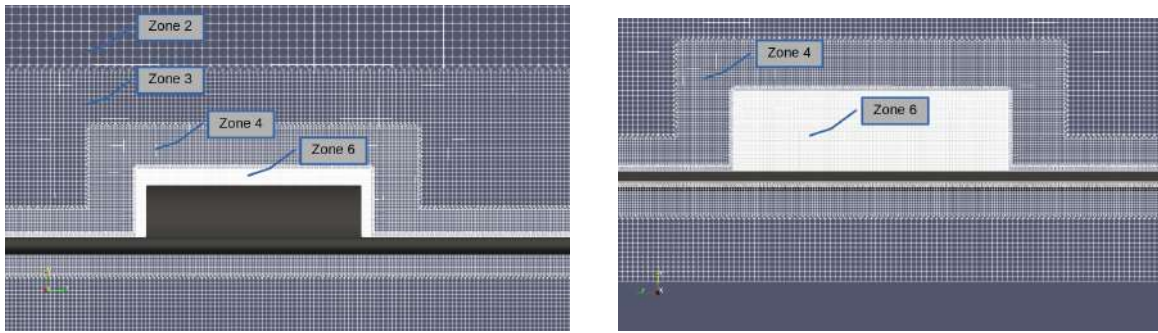
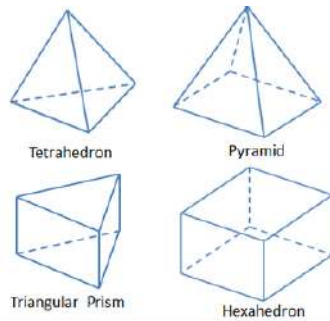


Figure 3.15: Mesh 3D mesh 2 - plane $x=1$ m and $x=1,77$ m

Mesh quality : The mesh is of good quality with mostly hexahedral cells,



hexahedra: 19839444,
prisms: 44946,
pyramids: 0,
tetrahedra: 0,
polyhedra: 548583,

and mostly orthogonal:

Mesh non-orthogonality max: 84.69618 degrees average: 8.624567 degrees,

Number of severely non-orthogonal (> 70 degrees) faces: 2264.

Mesh 3 : This mesh corresponds, to the mesh 2 with a large refinement at the jet orifices and in their vicinity and at the beginning of the separation zone :

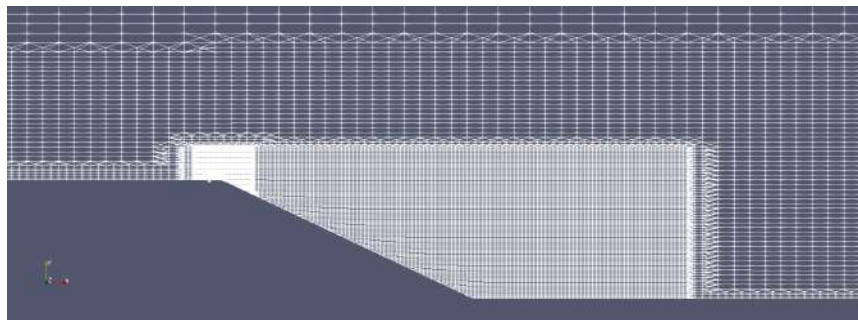
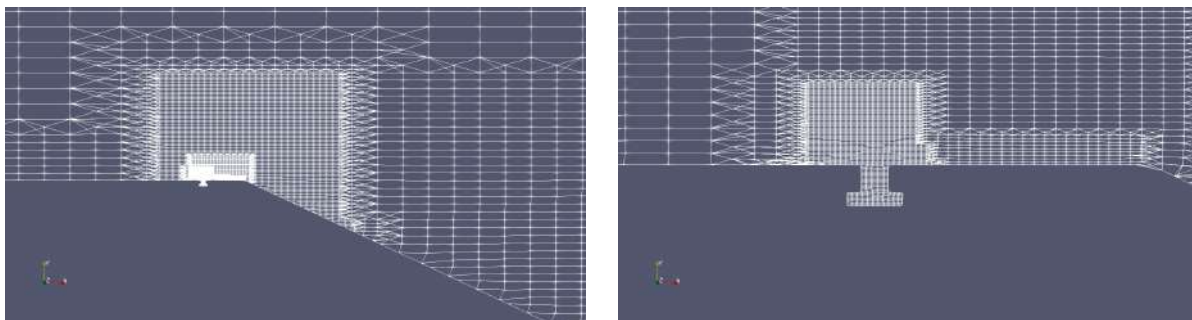
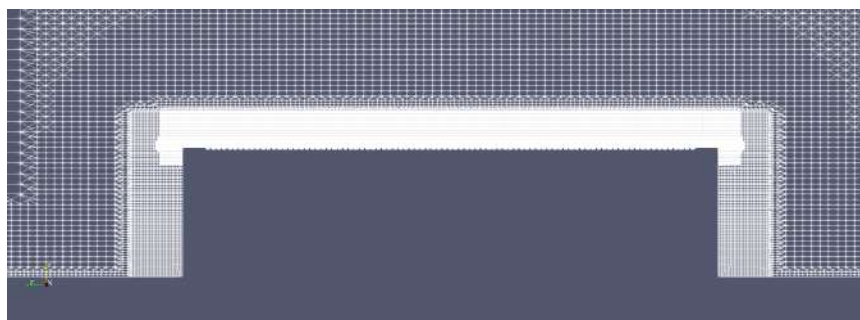
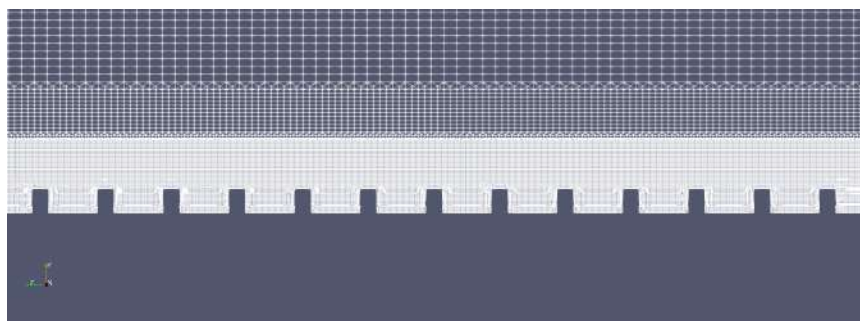


Figure 3.16: Mesh 3D mesh 3 - middle plane $z=0$

Figure 3.17: Mesh 3D mesh 3 - middle plane $z=0$ Figure 3.18: Mesh 3D mesh 3 - plane $x=1,42$ mFigure 3.19: Mesh 3D mesh 3 - plane $x=1,42$ m

3.3 RANS 2D simulation - uncontrolled case

The topic of this section concerns quick simulations and attempts to determine the influence of the turbulent model and the mesh. We compare the behaviour of the two first-order models of turbulence described in the chapter 2.4 on a large separated zone at the rear of the profile.

This test was conducted using two-dimensional (2D) simulations of the two first type mesh extracted from the transverse middle plane.

3.3.1 Pressure coefficient results

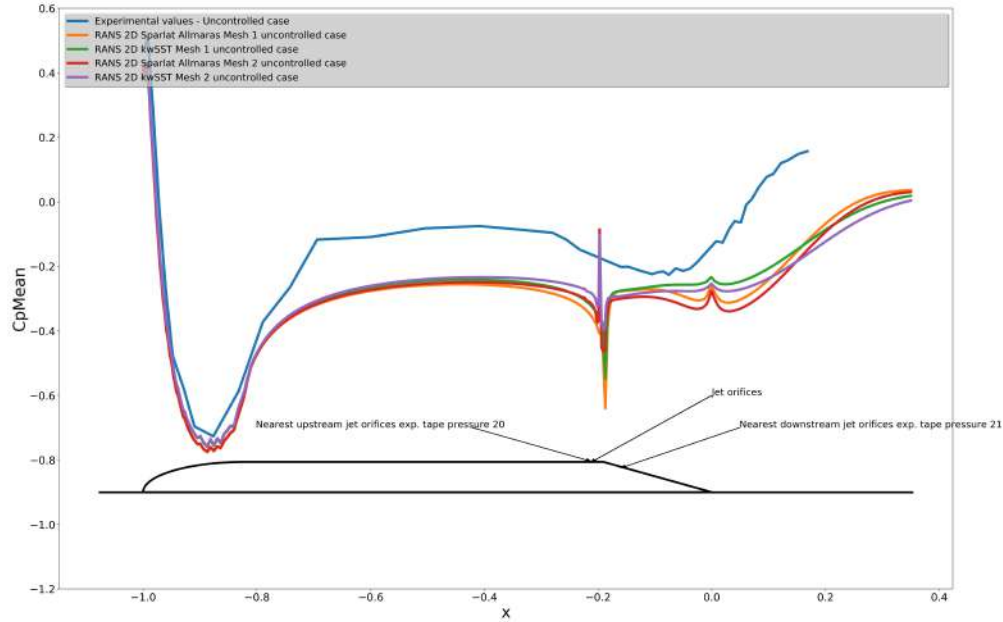


Figure 3.20: Pressure coefficient middle plane $z=0$ - RANS 2D kwSST and SA simulations Mesh 1 and Mesh 2 plus experimental data - uncontrolled case.

3.3.2 Mean flow topology results

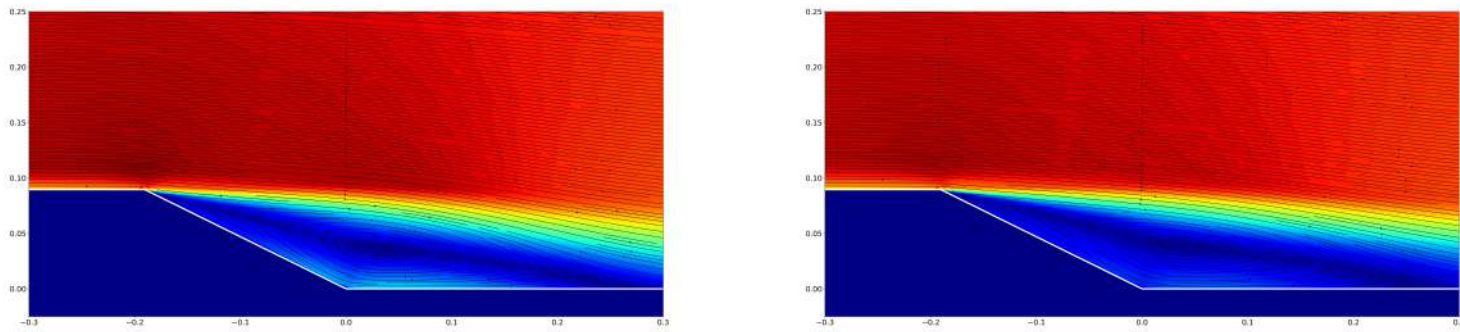


Figure 3.21: Streamline mean adimensional velocity middle plane $z=0$ - RANS 2D SA Mesh 1 distance of reattachment $h_r/L = 0.469$ (left) - Streamline mean adimensional velocity middle plane $z=0$ - RANS 2D kwSST Mesh 1 distance of reattachment $h_r/L = 0.457$ (right) - uncontrolled case.

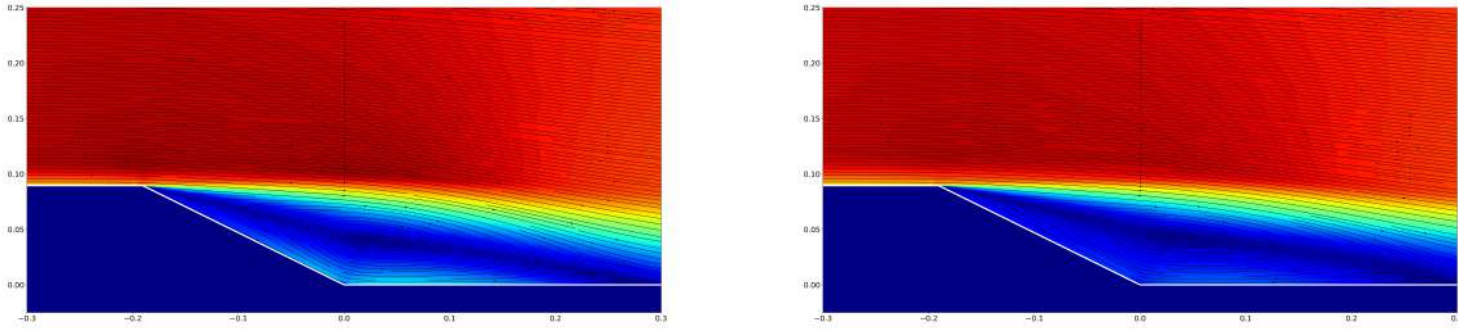


Figure 3.22: Streamline mean adimensional velocity middle plane $z=0$ - RANS 2D SA Mesh 2 distance of reattachment $h_r/L = 0.485$ (left) - Streamline mean adimensional velocity middle plane $z=0$ - RANS 2D kwSST Mesh 2 distance of reattachment $h_r/L = 0.486$ (right) - uncontrolled case.

3.3.3 Discussion

The results do not match the experimental results, neither the reattachment length for the C_p in the middle plane. This unsurprising because of a known 3D problem (see chapter 1.2.1).

The two models of turbulence seem, in this case, to behave similarly whatever the refinement use on the mesh. The recirculation bubble is slightly more developed in the mesh 2 and the Sparlat-Allmaras turbulence model.

These 2D simulations do not give us relevant information on the influence of the model or on the mesh, so we proceeded with 3D simulations, which is the topic of the next section.

3.4 Global domain simulations - uncontrolled case

As already developed in the 2.4 section of this thesis, the simulation of the whole wind-tunnel does not allow us to use the finest grid mesh 3 with the jet orifices with the computing resources at our disposal. The aim of these simulations is to test on the mesh 1 (the least refined) and on the mesh 2 (the more accurate) first-order turbulent models kwSST (see chapter 2.4.4), the two different techniques RANS and DES and obtain inlet boundary conditions for the restrict calculation domain.

A test between the Sparlat-Allmaras model and the kwSST model was carried out with the DES technique on the restrict domain in the next section (see chapter 3.5).

3.4.1 Boundary conditions

See figure 3.2 for the name and position of the boundaries.

At the inlet :

U is set with a fixed value at 30 m/s in the whole boundary,

p is considered to be zero gradient,

k is estimated by the formulation $k = \frac{3}{2}(U_{inlet}I)^2$, where I is the turbulence intensity set here to 1%,

ω is given by $\omega = \frac{k^{1/2}}{C_\mu^{1/4}l}$, where l is the turbulent length scale, here set to 0.035m considering a grid turbulence with 35mm diameter bars and where C_μ is an empirical constant (approximately 0.09),

ν_t is calculated through k and l for the kwSST model and is set to $\nu_t = 2 \times \nu$ for the Sparlat-Allmaras model.

At the outlet :

All the components of the calculation are set to zero gradient.

Wall conditions :

At the windtunnel wall :

U is set with a slip condition considering here the wall of the simulated domain outside the boundary layers of the real domain-,

p is considered to be zero gradient,

k , ω , and ν_t are considered to be zero gradient.

On the body :

U is set to a no slip condition on the body and is calculated in boundary layers of the body,

p is considered to be zero gradient at walls,

ν_t is calculated through k and l for the kwSST model and is modelled with the OpenFOAM function `nutkWallFunction` for the Sparlat-Allmaras model,

k is modelled with the OpenFOAM function `kqRWallFunctions` which corresponds to a zero gradient,

ω is modelled with the OpenFOAM function `OmegaWallFunctions`, which is [10]

in the viscous layer,

$$\omega_{Vis} = \frac{6.0\nu}{\beta_1 y^2}$$

where β_1 is constant with value of 0.075,

in the log area,

$$\omega_{Log} = \frac{k^{1/2}}{C_\mu^{1/4} \kappa y}$$

, where C_μ is an empirical constant (approximately 0.09).

ω is the sum of the two functions : $\omega = \omega_{Vis} + \omega_{Log}$

3.4.2 Schemes

All the schemes used are second-order schemes, without a limiter in most of the cases.

The estimation of values on the faces cells is done with a linear interpolation of the centres cells computed values.

The estimation of the gradient on the faces cells for the Laplacian scheme is corrected in the case of non-orthogonal mesh.

The time scheme is transient, second order implicit for the DES calculations.

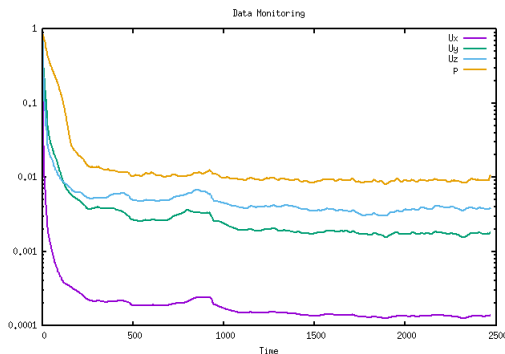
3.4.3 Resolution

Time depended equations or each iteration of a RANS simulation are resolved with iterative methods and Gauss-Seidel smoother, while the Poisson's equation resolution of the pressure is done with preconditioned techniques or with a geometric-algebraic multi-grid solver (GAMG) to gain in performance in the case of a small time-step.

3.4.4 RANS 3D simulation - Mesh 1 - kwSST

Conditions of the run

The model of turbulence used is the kwSST model.



The convergence of the solution is reached after 1000 iterations. We represent below the solution after 2300 iterations.

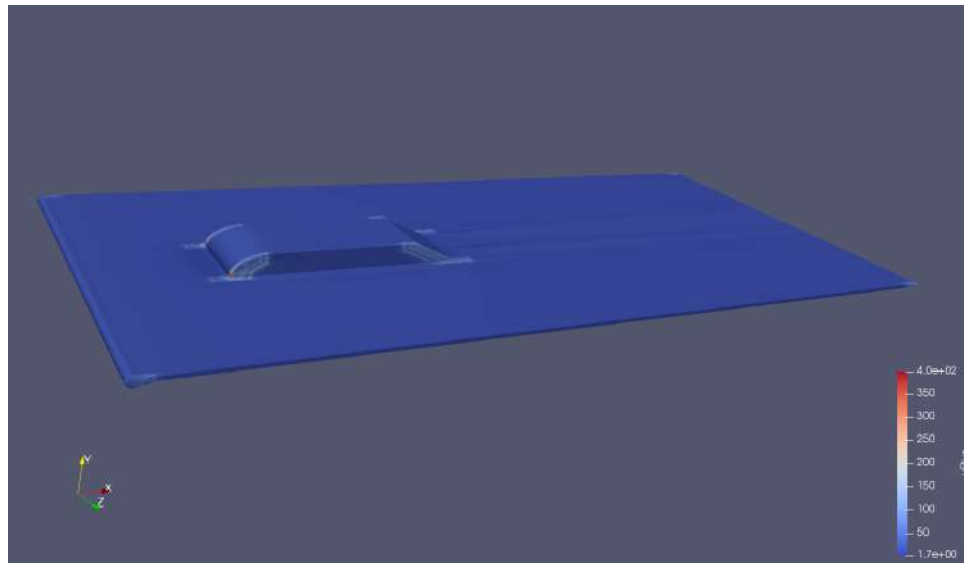


Figure 3.23: RANS 3D Mesh 1 - The value of y^+ is generally good and mostly under 50.

Pressure coefficient results

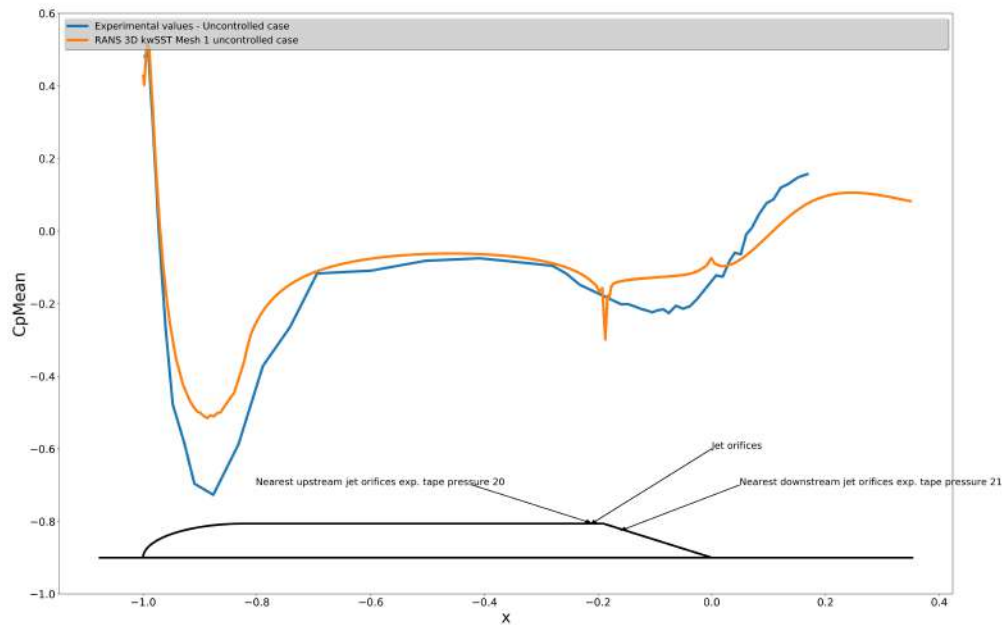


Figure 3.24: Pressure coefficient middle plane $z=0$ - RANS 3D kwSST simulations Mesh 1 and experimental data - uncontrolled case.

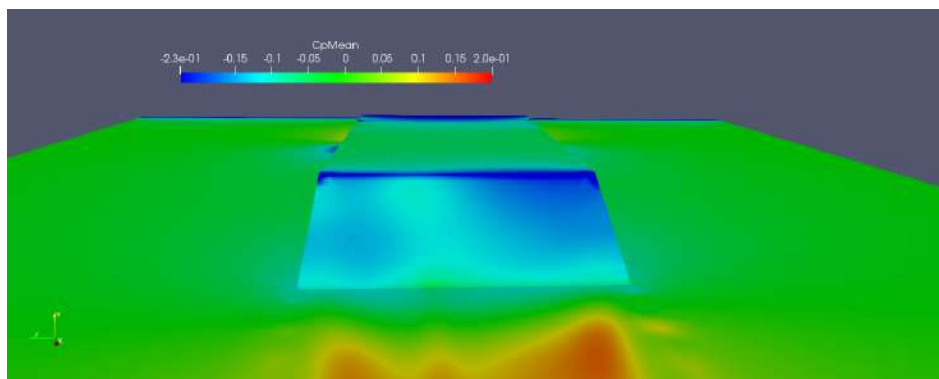


Figure 3.25: Pressure coefficient at the rear of the shape on the ramp - RANS 3D kwSST simulations Mesh 1 - uncontrolled case.

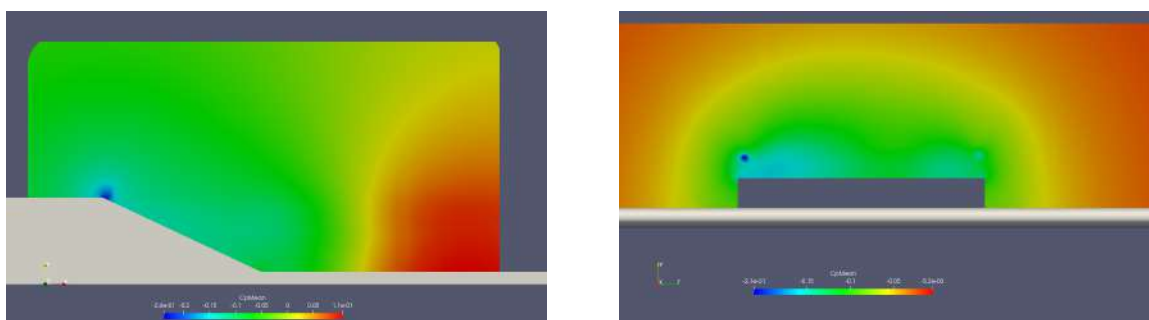


Figure 3.26: Pressure coefficient middle plane $z=0$ (left) and transverse plane $x=1.53$ m (or $x=-0.095$ in dimensional coordinates with the centre at the rear) (right) - RANS 3D kwSST simulations Mesh 1 - uncontrolled case.

Mean flow topology results

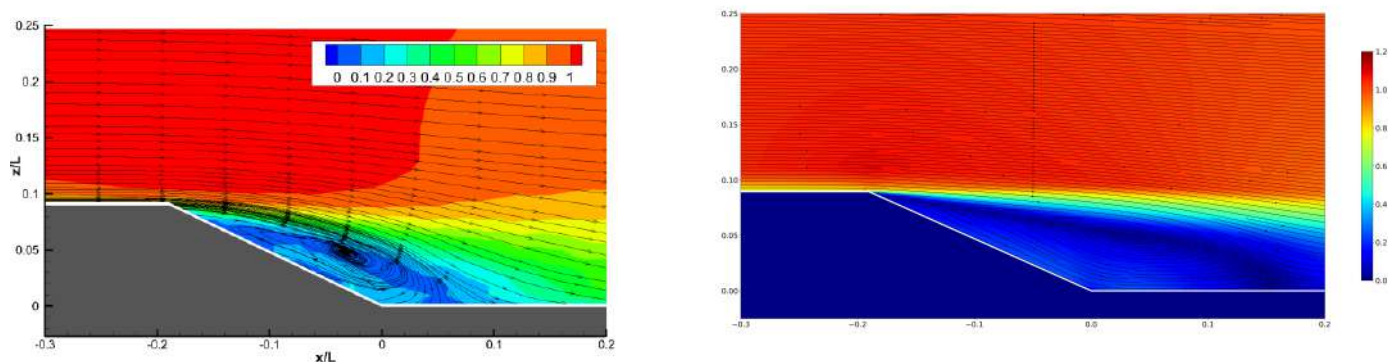


Figure 3.27: Streamline mean adimensional velocity middle plane $z=0$ - Experimental data distance of reattachment $h_r/L = 0.24$ [5] (left) - Streamline mean adimensional velocity middle plane $z=0$ - RANS 3D kwSST Mesh 1 distance of reattachment $h_r/L = 0.349$ (right) - uncontrolled case.

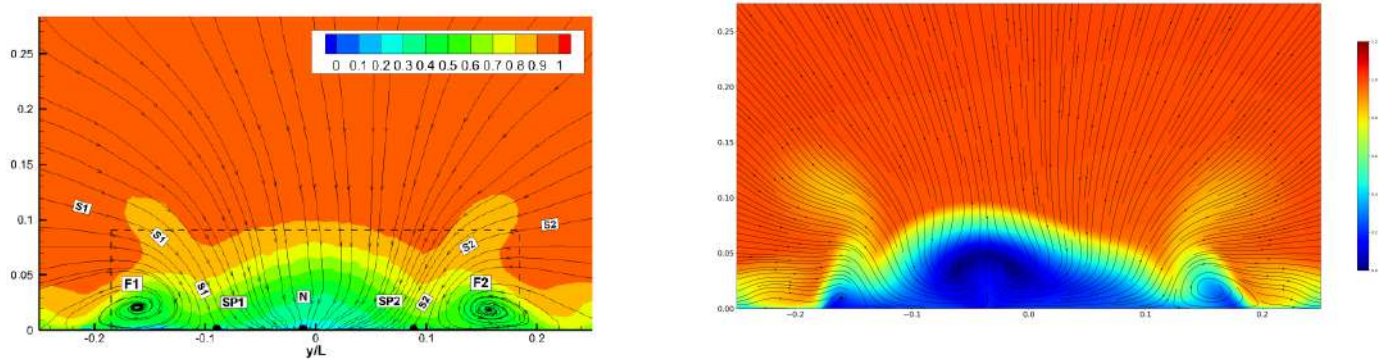


Figure 3.28: Streamline mean adimensional velocity transverse plane $x=1.77$ m (or $x=0.13$ in adimensional coordinates with the centre at the rear) - Experimental data [5] (left) - Streamline mean adimensional velocity transverse plane $x=1.77$ m - RANS 3D kwSST Mesh 1 (right) - uncontrolled case.

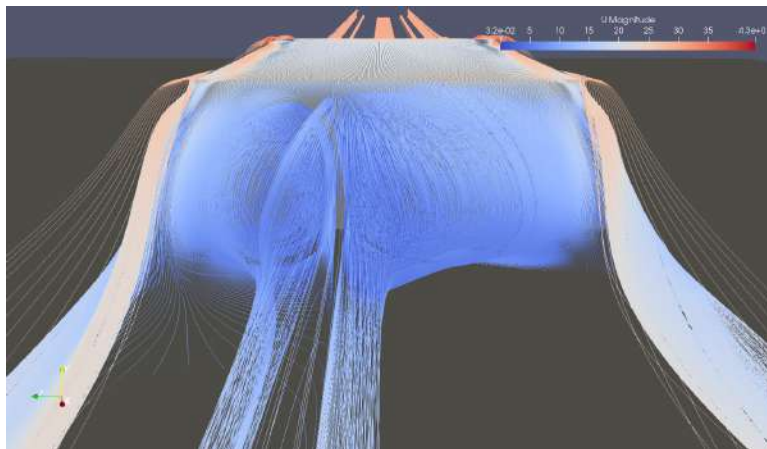


Figure 3.29: UMean streamline at the rear - RANS 3D kwSST simulations Mesh 1 - uncontrolled case.

Unsteady flow topology results

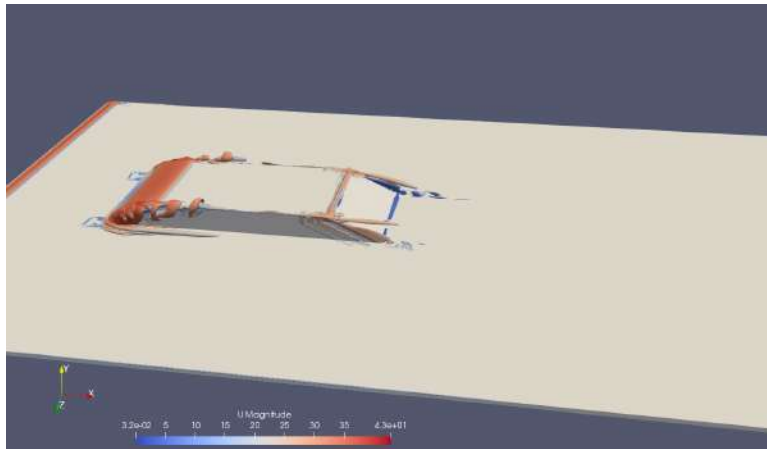


Figure 3.30: Q criterion RANS 3D kwSST simulations Mesh 1 - Contour $Q = \frac{4U_{\infty}^2}{H^2}$ coloured by U_{mean} - uncontrolled case.

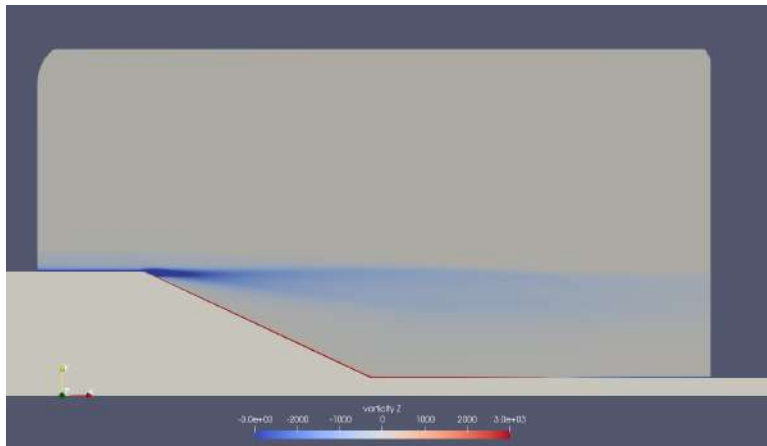


Figure 3.31: Vorticity contour middle plane $z=0$ - RANS 3D kwSST simulations Mesh 1 - uncontrolled case.

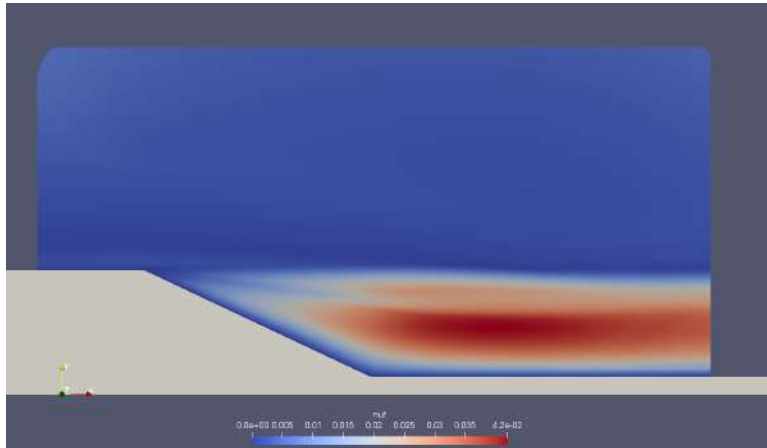


Figure 3.32: nut middle plane $z=0$ - RANS 3D kwSST simulations Mesh 1 - uncontrolled case.

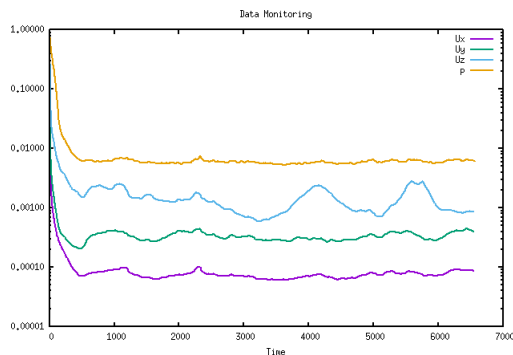
Drag coefficient

	ReL.10-6	CD Uncontrolled flow
Experimental estimation	2,35	0,206
Numerical simulation RANS mesh1	2,35	0,142712

Figure 3.33: C_D value at the rear slant comparison RANS 3D mesh 1 simulation and experiment - uncontrolled case.

3.4.5 RANS 3D simulation - Mesh 2 - kwSST

The model of turbulence used is the kwSST model.



The convergence of the solution is in this case relatively mediocre. We represent below the solution after 6500 iterations.

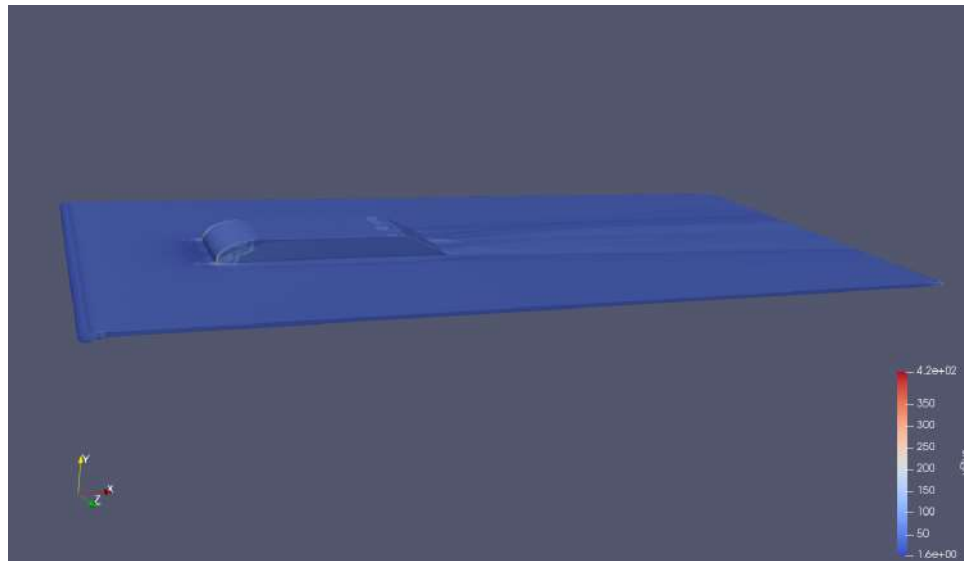


Figure 3.34: RANS 3D Mesh 1 - The value of y^+ is generally good and mostly under 50

Pressure coefficient results

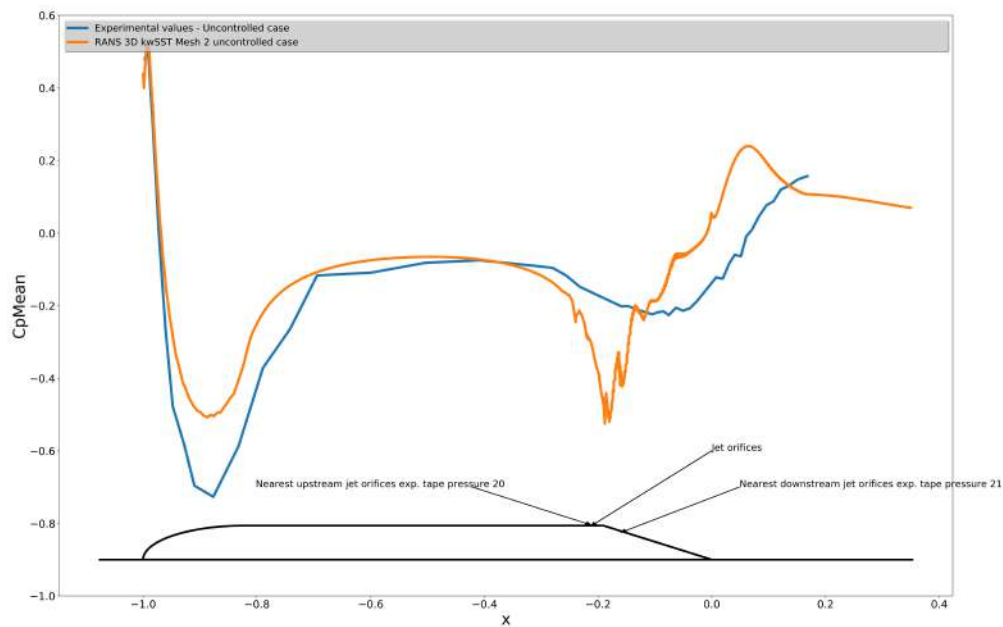


Figure 3.35: Pressure coefficient middle plane $z=0$ - RANS 3D kwSST simulations Mesh 2 and experimental data - uncontrolled case.

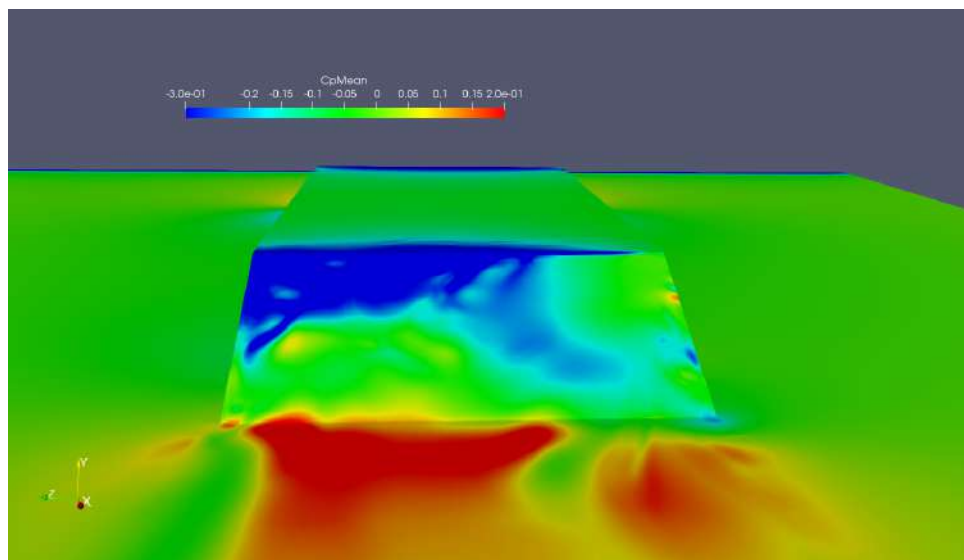


Figure 3.36: Pressure coefficient at the rear of the shape on the ramp - RANS 3D kwSST simulations Mesh 2 - uncontrolled case.

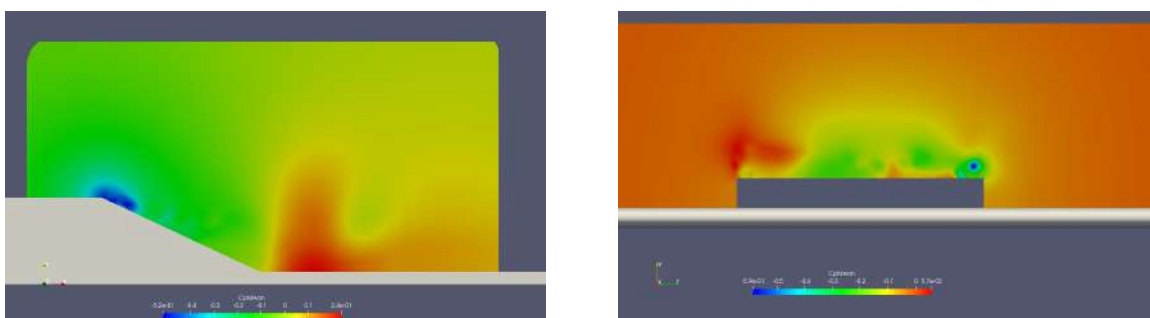


Figure 3.37: Pressure coefficient middle plane $z=0$ (left) and transverse plane $x=1.53$ m (right) - RANS 3D kwSST simulations Mesh 2 - uncontrolled case.

Mean flow topology results

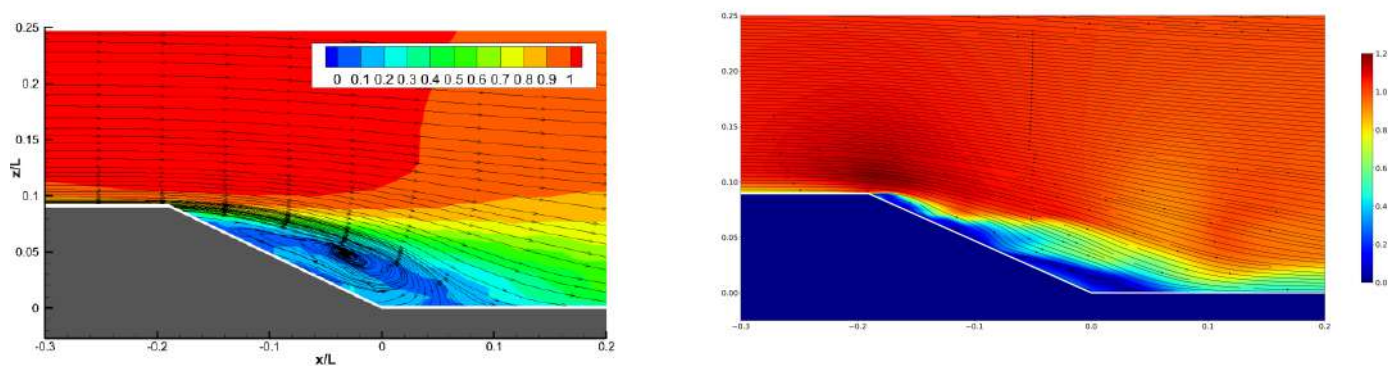


Figure 3.38: Streamline mean adimensional velocity middle plane $z=0$ - Experimental data distance of reattachment $h_r/L = 0.24$ [5] (left) - Streamline mean adimensional velocity middle plane $z=0$ - RANS 3D kwSST Mesh 2 distance of reattachment $h_r/L = 0.230$ (right) - uncontrolled case.

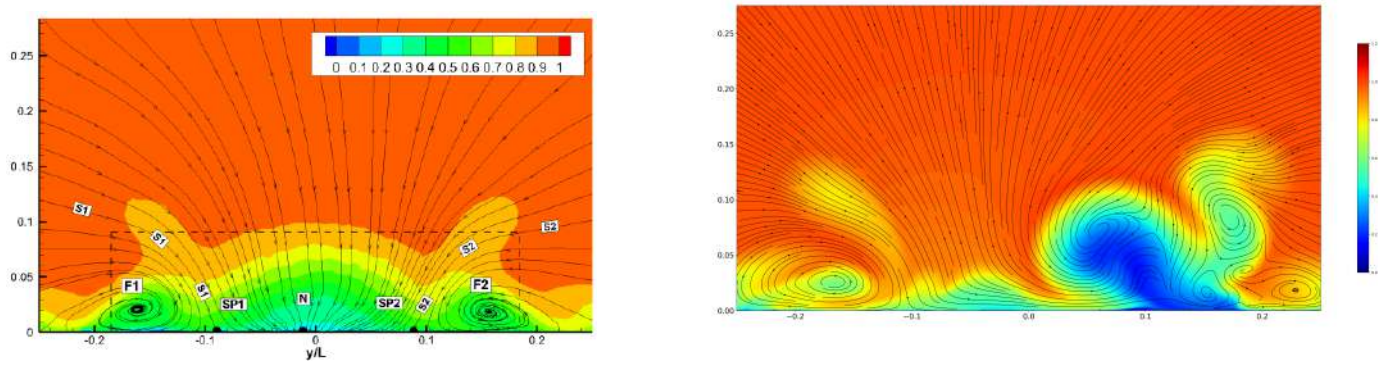


Figure 3.39: Streamline mean adimensional velocity transverse plane $x=1.77$ m - Experimental data [5] (left) - Streamline mean adimensional velocity transverse plane $x=1.77$ m - RANS 3D kwSST Mesh 2 (right) - uncontrolled case.

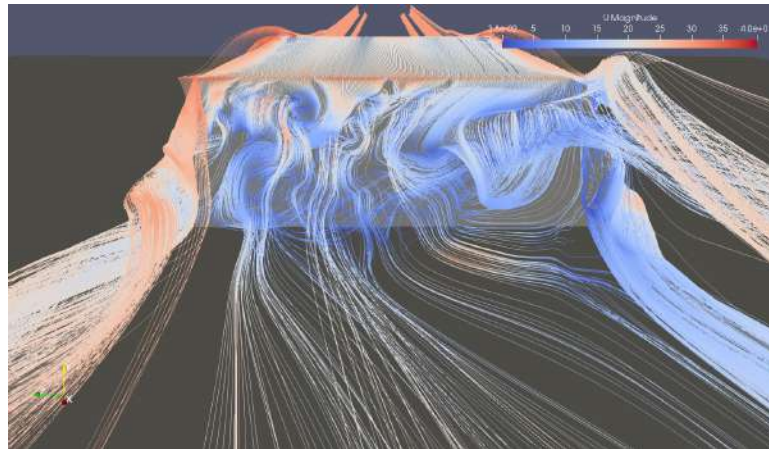


Figure 3.40: UMean streamline at the rear - RANS 3D kwSST simulations Mesh 2 - uncontrolled case.

Unsteady flow topology results

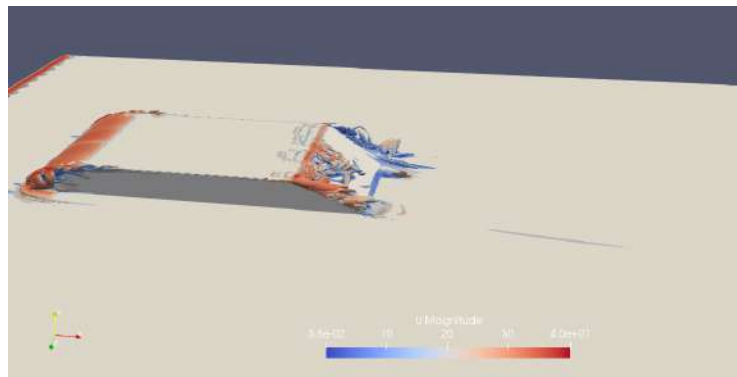


Figure 3.41: Q criterion RANS 3D kwSST simulations Mesh 2 - Contour $Q = \frac{4U_{\infty}^2}{H^2}$ coloured by Umean - uncontrolled case.

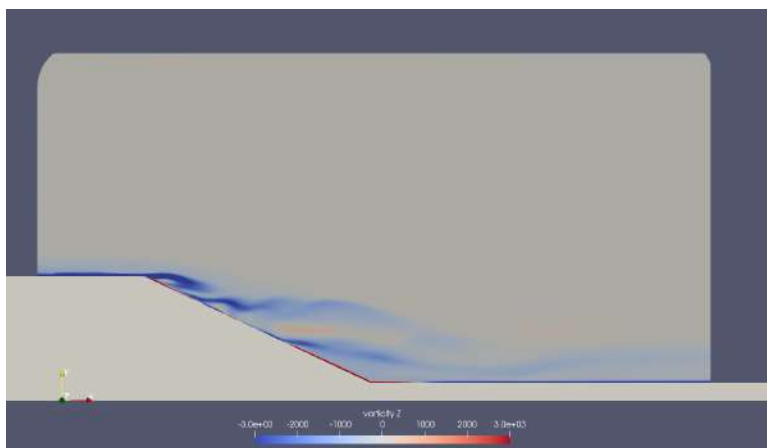


Figure 3.42: Vorticity contour middle plane $z=0$ - RANS 3D kwSST simulations Mesh 2 - uncontrolled case.

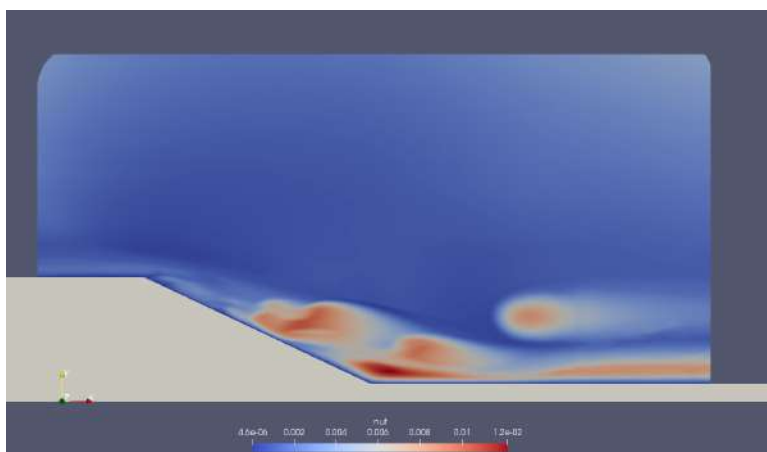


Figure 3.43: nut middle plane $z=0$ - RANS 3D kwSST simulations Mesh 2 - uncontrolled case.

Drag coefficient

	ReL10-6	CD Uncontrolled flow
Experimental estimation	2,35	0,206
Numerical simulation RANS mesh2	2,35	0,1612

Figure 3.44: C_D value at the rear slant comparison RANS 3D mesh6 simulation and experiment - uncontrolled case.

3.4.6 DES 3D simulation - Mesh 1 - kwSST

Conditions of the run

The model of turbulence used for the subgrid scales and the boundary layers is the kwSST model.

The solution for the mean flow is reached when the C_p profile curve at the middle plane is relatively stable for an $1T_L$ average pressure. The solution presented below is obtained after $t = 4T_L$ and averaged over $t = 6T_L$.

The condition $Co \leq 1$ is globally respected, thus avoiding numerical dissipation for hyperbolic equations.

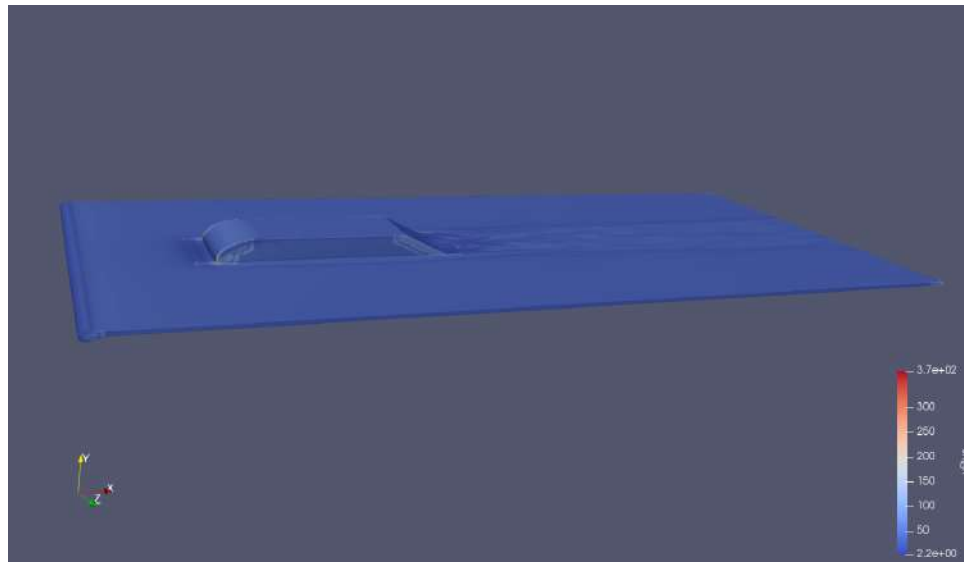


Figure 3.45: DES 3D Mesh 1 - The value of y^+ is generally good and mostly under 50

Pressure coefficient results

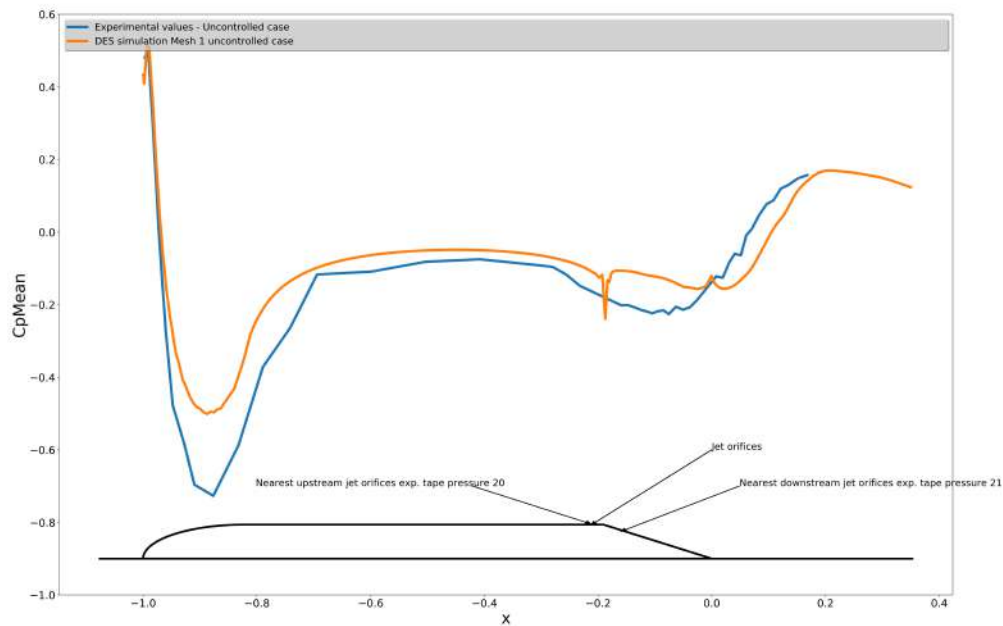


Figure 3.46: Pressure coefficient middle plane $z=0$ - DES 3D kwSST simulations Mesh 1 and experimental data - uncontrolled case.

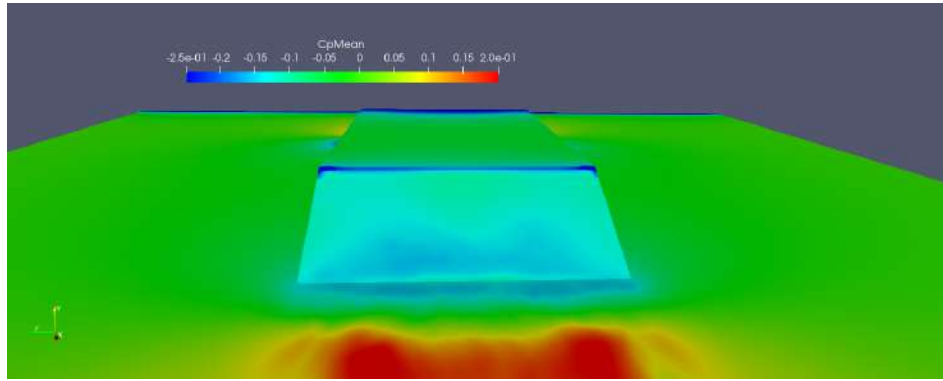


Figure 3.47: Pressure coefficient at the rear of the shape on the ramp - DES 3D kwSST simulations Mesh 1 - uncontrolled case.

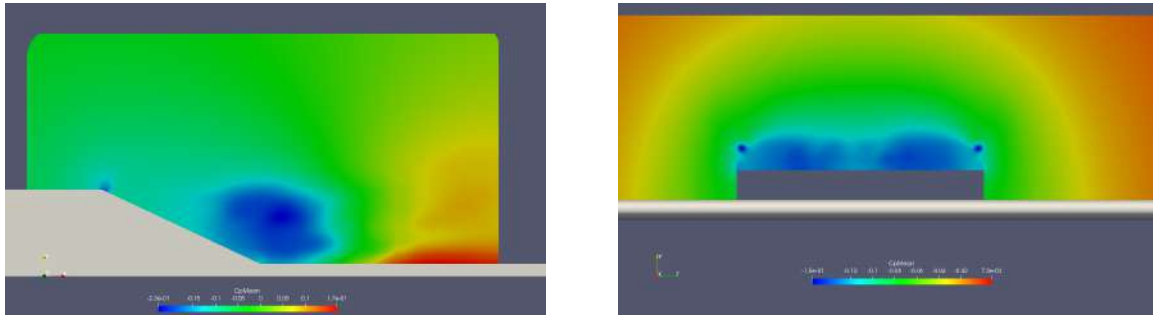


Figure 3.48: Pressure coefficient middle plane $z=0$ (left) and transverse plane $x=1.53$ m (or $x=-0.095$ in dimensional coordinates with the centre at the rear) (right) - DES 3D kwSST simulations Mesh 1 - uncontrolled case.

Mean flow topology results

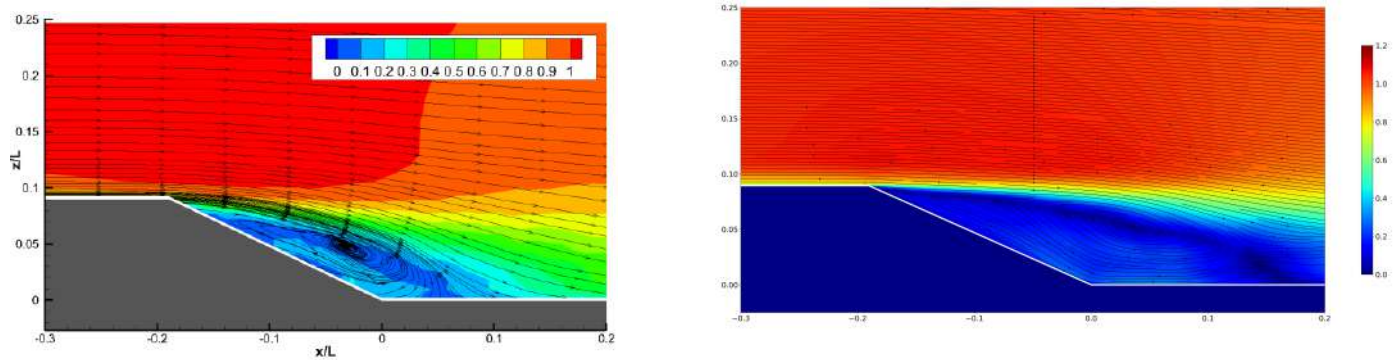


Figure 3.49: Streamline mean adimensional velocity middle plane $z=0$ - Experimental data distance of reattachment $h_r/L = 0.24$ [5] (left) - Streamline mean adimensional velocity middle plane $z=0$ - DES 3D kwSST Mesh 1 distance of reattachment $h_r/L = 0.369$ (right) - uncontrolled case.

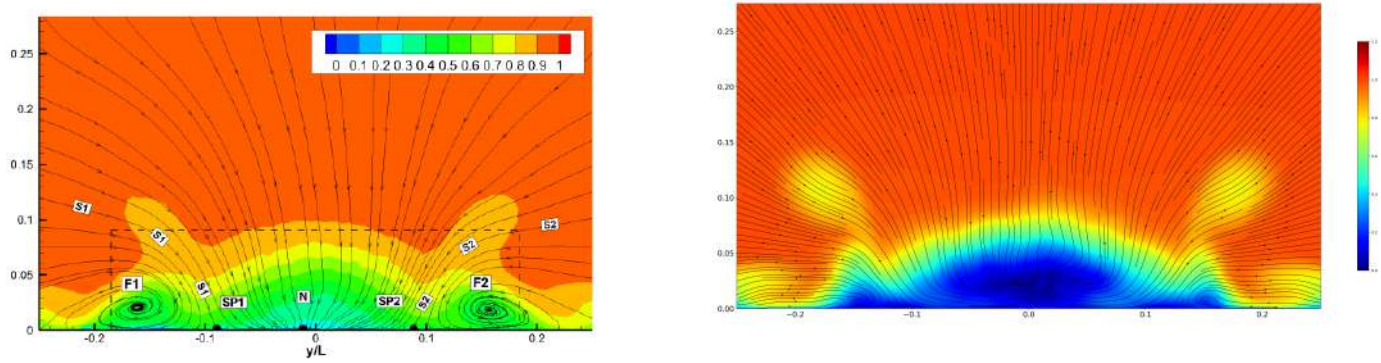


Figure 3.50: Streamline mean adimensional velocity transverse plane $x=1.77$ m (or $x=0.13$ in adimensional coordinates with the centre at the rear) - Experimental data [5] (left) - Streamline mean adimensional velocity transverse plane $x=1.77$ m - DES 3D kwSST Mesh 1 (right) - uncontrolled case.

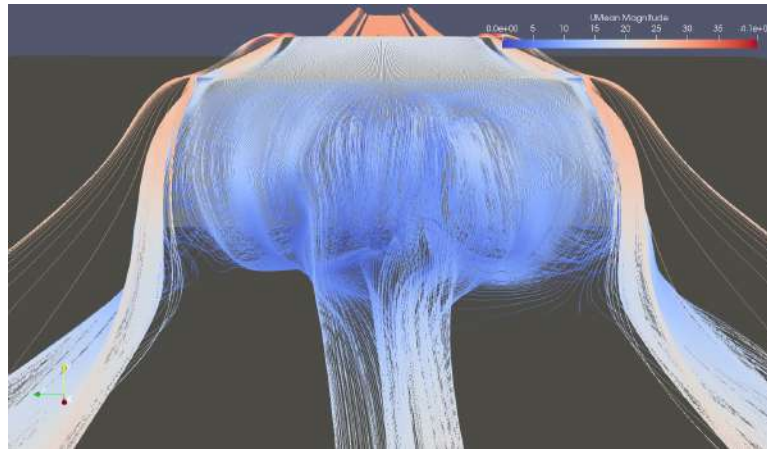


Figure 3.51: UMean streamline at the rear - DES 3D kwSST simulations Mesh 1 - uncontrolled case.

Unsteady flow topology results

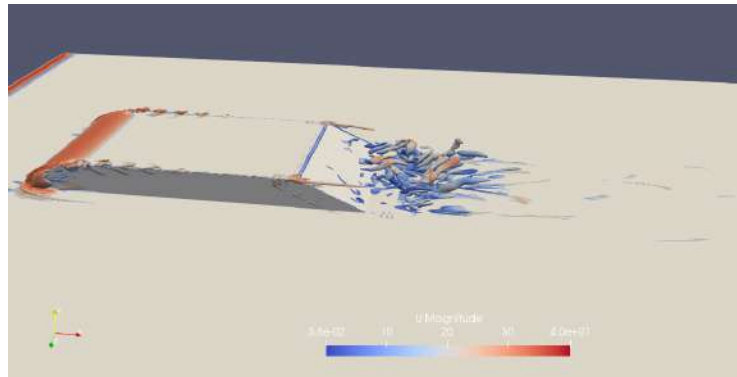


Figure 3.52: Q criterion DES 3D kwSST simulations Mesh 1 - Contour $Q = \frac{4U_\infty^2}{H^2}$ coloured by Umean - uncontrolled case.

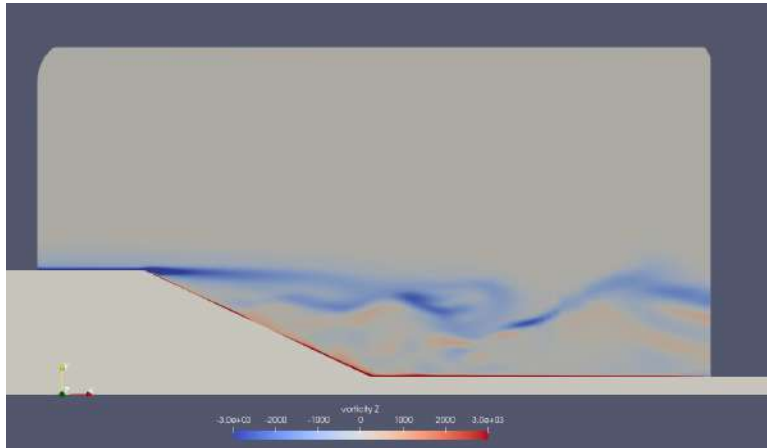


Figure 3.53: Vorticity contour middle plane $z=0$ - DES 3D kwSST simulations Mesh 1 - uncontrolled case.

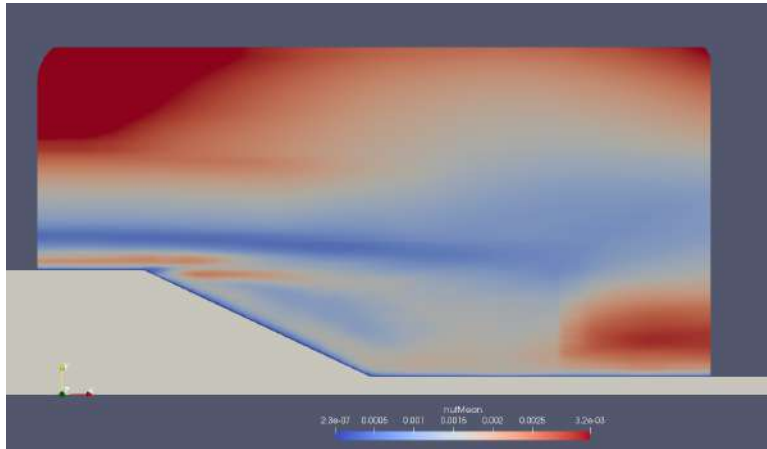


Figure 3.54: nut mean middle plane $z=0$ - DES 3D kwSST simulations Mesh 1 - uncontrolled case.

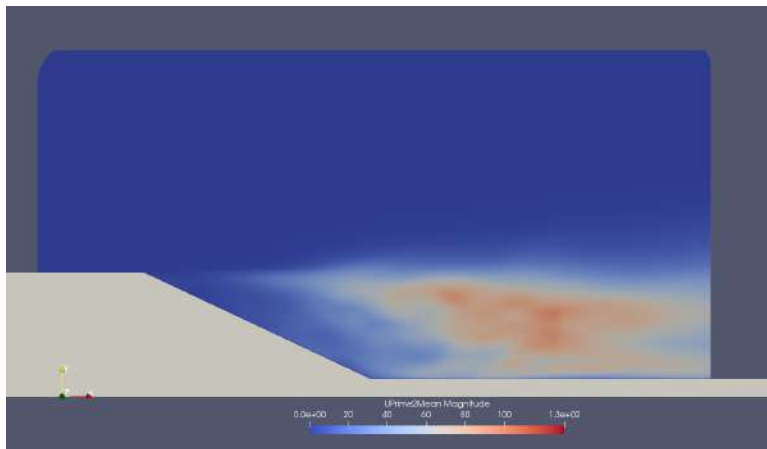


Figure 3.55: Reynolds stress magnitude middle plane $z=0$ - DES 3D kwSST simulations Mesh 1 - uncontrolled case.

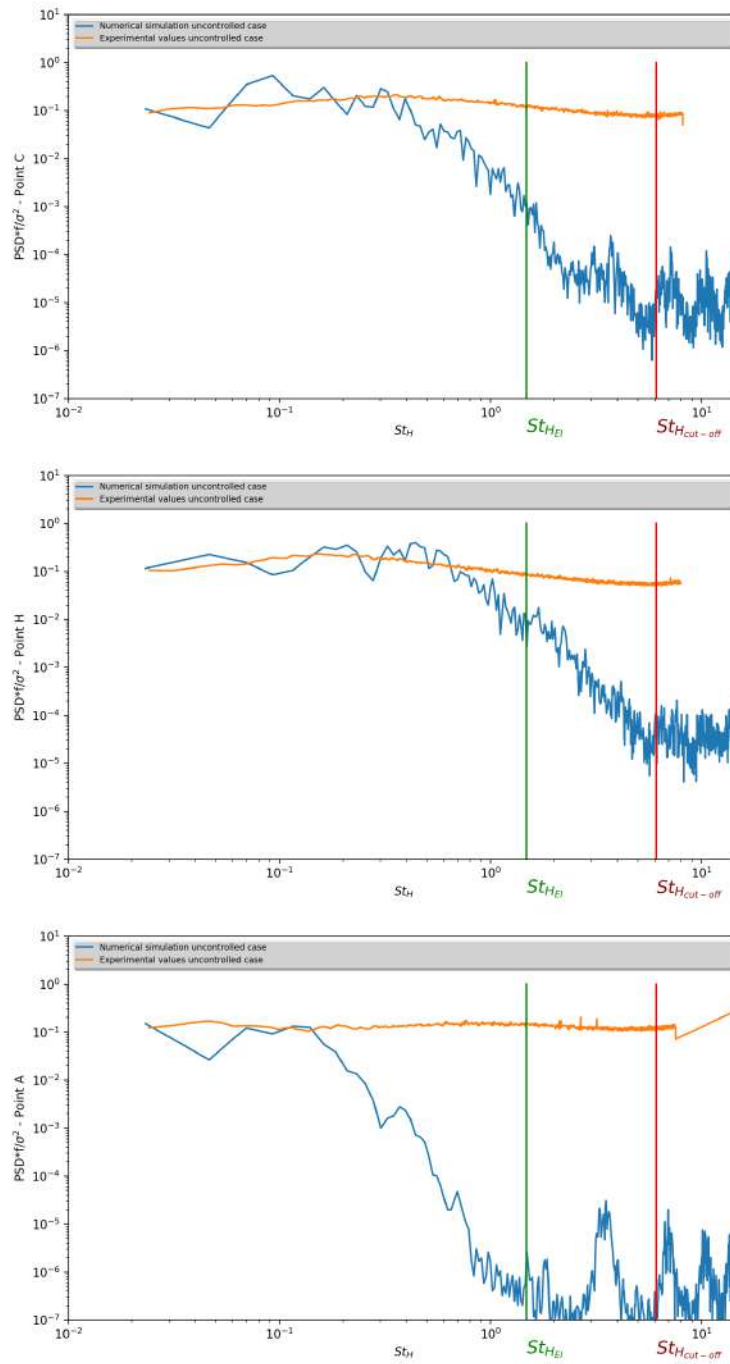


Figure 3.56: Normalised power spectral density of the velocity signal at points C,H,A (see 2.3.4) - DES 3D kwsST simulations Mesh 1 and experimental values [5] - uncontrolled case.

Drag coefficient

	ReL.10-6	CD Uncontrolled flow
Experimental estimation	2,35	0,206
Numerical simulation DES mesh1	2,35	0,136144

Figure 3.57: C_D value at the rear slant comparison DES kwSST 3D mesh 1 simulation and experiment - uncontrolled case.

3.4.7 DES 3D simulation - Mesh 2 - kwSST - large time step

A first attempt at a DES simulation on the global domain with a refined mesh was done with a relatively large time step and with a limiter on the transport equation of ω :

The model of turbulence used for the subgrid scales and the boundary layers is the kwSST model. The solution for the mean flow is reached when the C_p profile curve at the middle plane is relatively stable for an $1T_L$ average pressure. The solution presented below is obtained after $t = 10T_L$ and averaged over $t = 11T_L$.

The maximum of Co is set to 6, though the condition $Co \leq 1$ is, in general respected, thus avoiding numerical dissipation for hyperbolic equations.

It is relevant to note here that the kwSST model is trickier to use than the Sparlat-Allmaras model because of the relative sensitivity of the diffusive term $\frac{\partial}{\partial x_j} \left(\Gamma_\omega \frac{\partial \omega}{\partial x_j} \right)$ in the transport equation of ω particularly with severe non progressive uniformity of the grid mesh. Quality of the mesh for a kwSST model must be superior otherwise a limiter on gradient discretisation need to be used with a degradation of the accuracy of the scheme and the solution.

In this case of time step and mesh we had to use a limiter on the transport equation of ω .

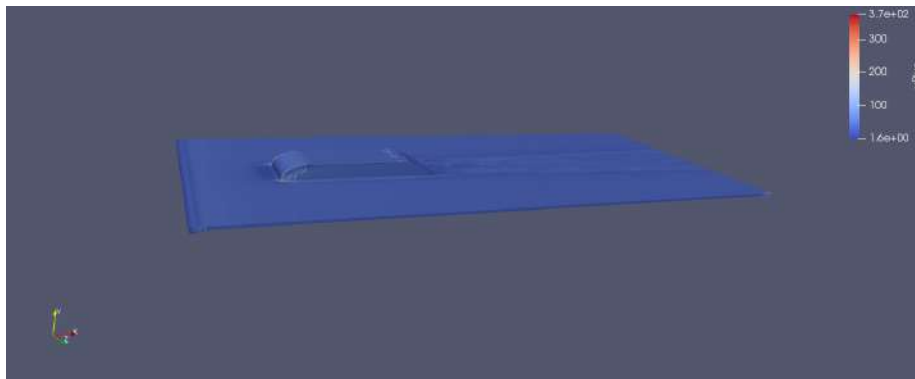


Figure 3.58: DES 3D Mesh 2 - The value of y^+ is generally good and mostly under 50

Pressure coefficient results

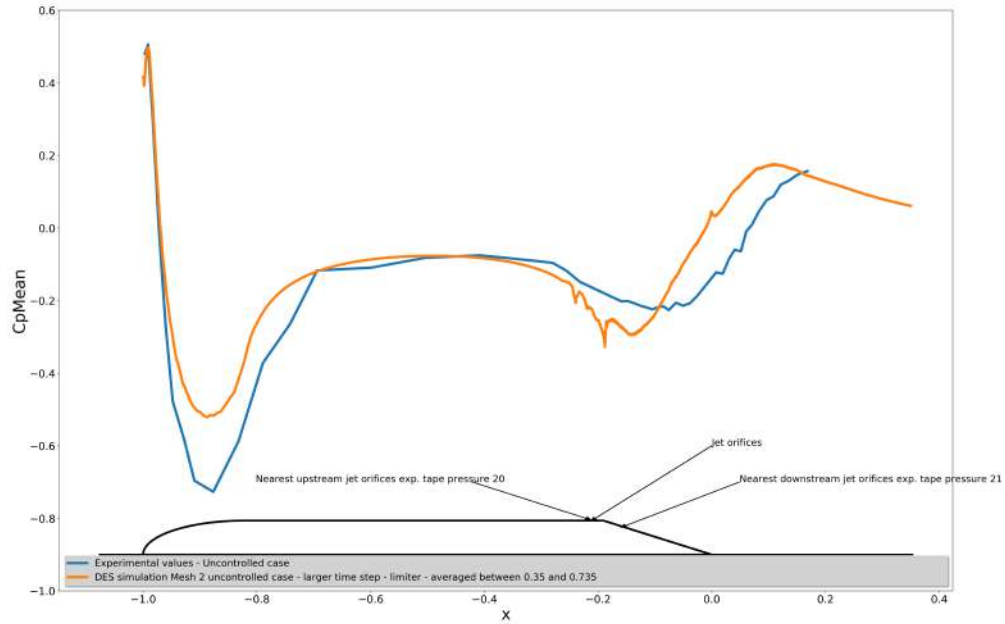


Figure 3.59: Pressure coefficient middle plane $z=0$ - DES 3D kwSST simulations Mesh 2 and experimental data - uncontrolled case.

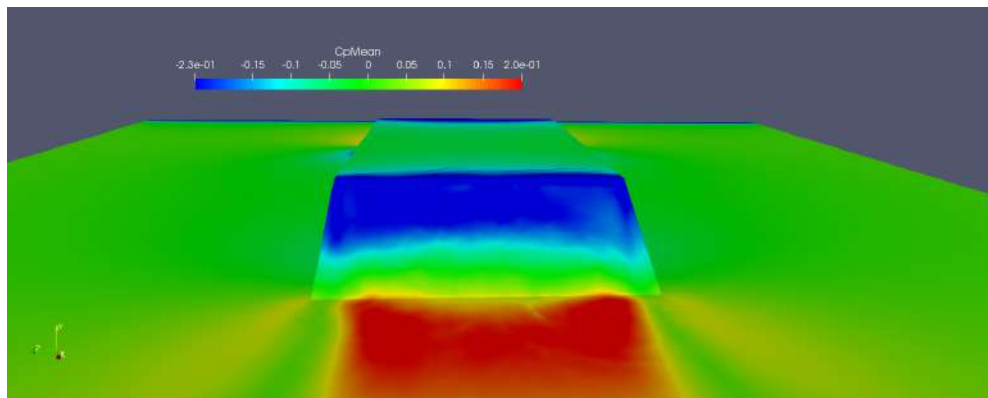


Figure 3.60: Pressure coefficient at the rear of the shape on the ramp - DES 3D kwSST simulations Mesh 2 - uncontrolled case.

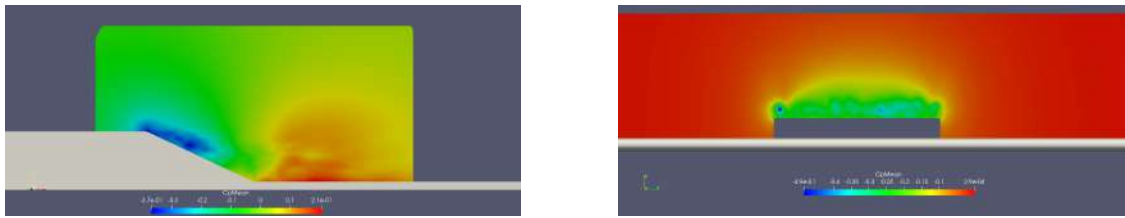


Figure 3.61: Pressure coefficient middle plane $z=0$ (left) and transverse plane $x=1.53$ m (right) - DES 3D kwSST simulations Mesh 2 - uncontrolled case.

Mean flow topology results

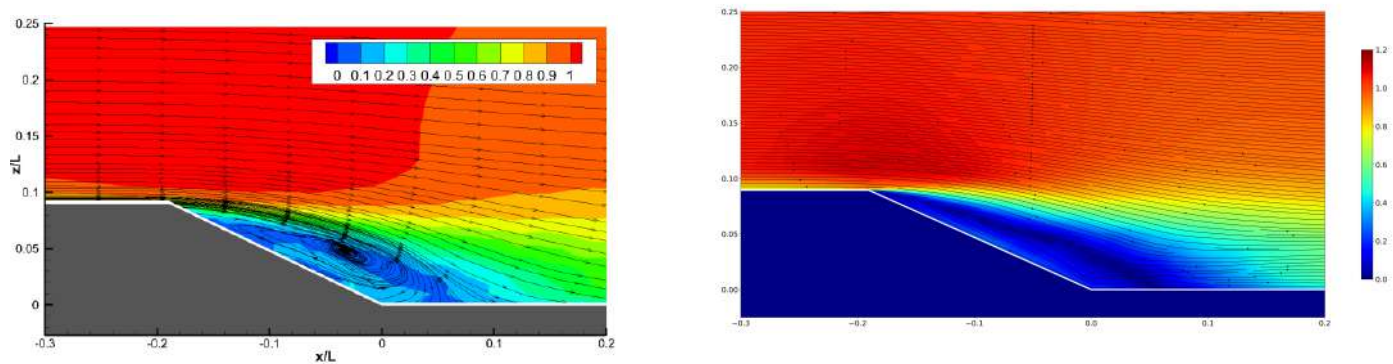


Figure 3.62: Streamline mean adimensional velocity middle plane $z=0$ - Experimental data distance of reattachment $h_r/L = 0.24$ [5] (left) - Streamline mean adimensional velocity middle plane $z=0$ - DES 3D kwSST Mesh 2 distance of reattachment $h_r/L = 0.255$ (right) - uncontrolled case.

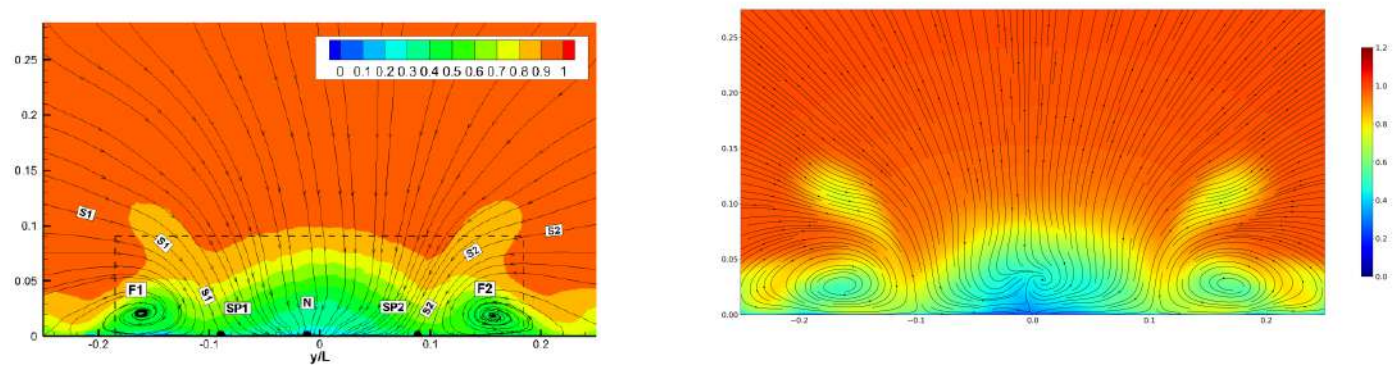


Figure 3.63: Streamline mean adimensional velocity transverse plane $x=1.77$ m - Experimental data [5] (left) - Streamline mean adimensional velocity transverse plane $x=1.77$ m - DES 3D kwSST Mesh 2 (right) - uncontrolled case.

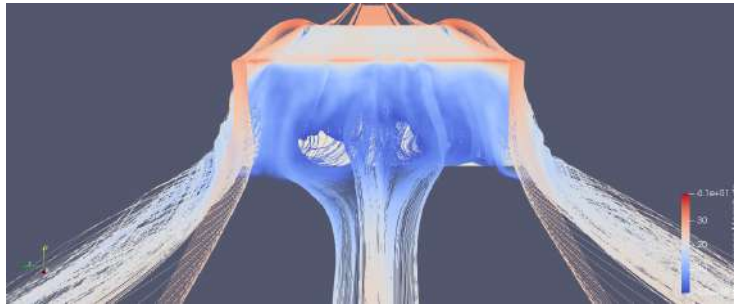


Figure 3.64: UMean streamline at the rear averaged on $t = 11T_L$ - DES 3D kwSST simulations Mesh 2 - uncontrolled case.

Unsteady flow topology results

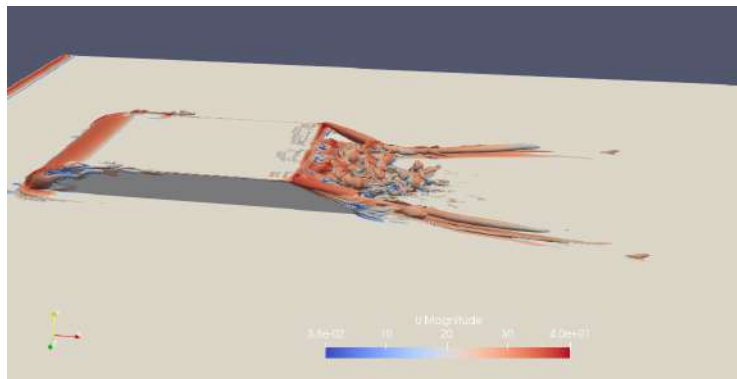


Figure 3.65: Q criterion DES 3D kwSST simulations Mesh 2 - Contour $Q = \frac{4U_\infty^2}{H^2}$ coloured by Umean - uncontrolled case.

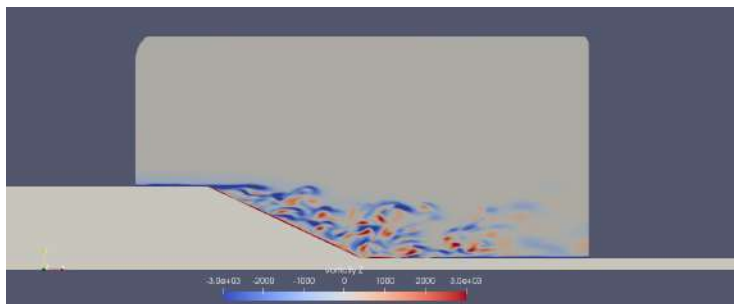


Figure 3.66: Vorticity contour middle plane $z=0$ - DES 3D kwSST simulations Mesh 2 - uncontrolled case.

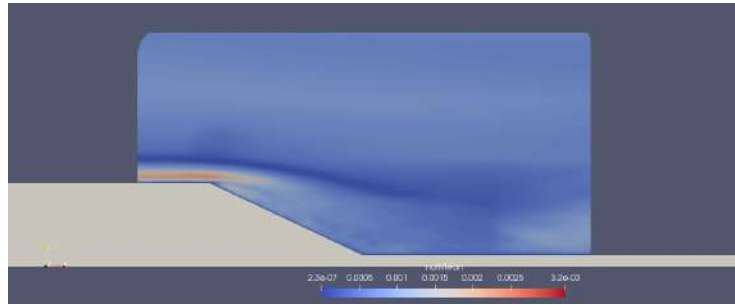


Figure 3.67: nut mean middle plane $z=0$ - DES 3D kwSST simulations Mesh 2 - uncontrolled case.

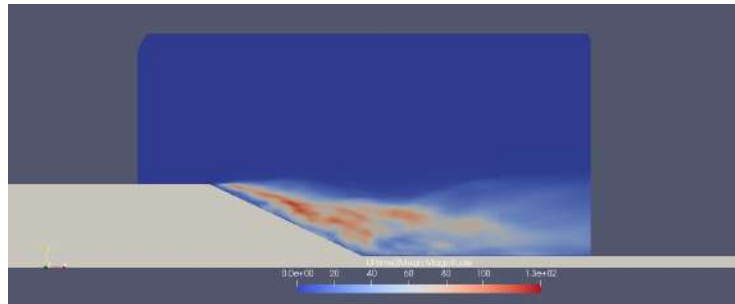


Figure 3.68: Reynolds stress magnitude middle plane $z=0$ - DES 3D kwSST simulations Mesh 2 - uncontrolled case.

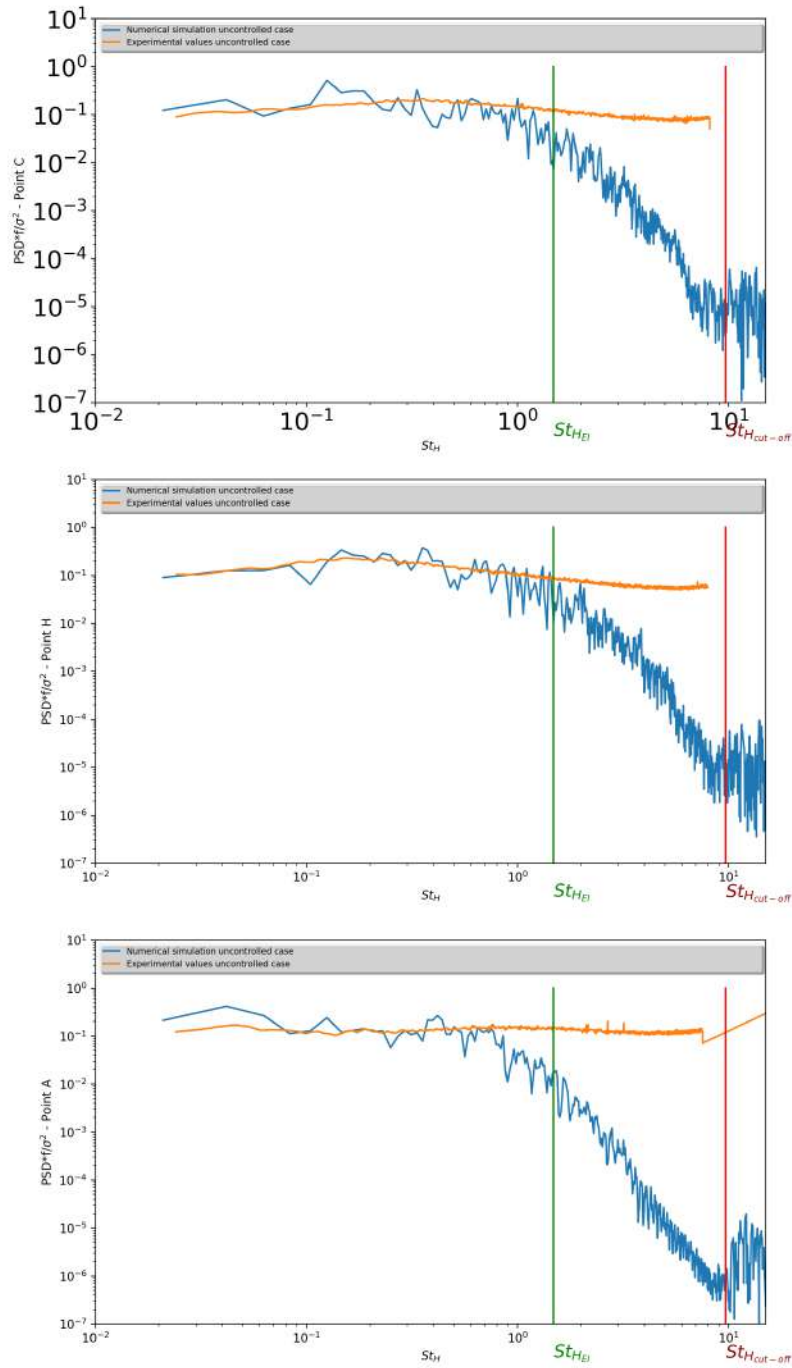


Figure 3.69: Normalised power spectral density of the velocity signal at points C,H,A - DES 3D kwSST simulations Mesh 2 and experimental values [5] - uncontrolled case.

Drag coefficient

	ReL.10-6	CD Uncontrolled flow
Experimental estimation	2,35	0,206
Numerical simulation DES mesh2		
Global Domain	2,35	0,1715

Figure 3.70: C_D value at the rear slant comparison DES 3D mesh6 simulation and experiment - uncontrolled case.

3.4.8 DES 3D simulation - Mesh 2 - kwSST - smaller time step

A second attempt at a DES simulation on the global domain on mesh 2 was done with a smaller time step and without a limiter on the transport equation of ω :

The model of turbulence used for the subgrid scales and the boundary layers is the kwSST model. The solution for the mean flow is reached when the C_p profile curve at the middle plane is relatively stable for an $1T_L$ average pressure. The solution presented below is obtained after $t = 10T_L$ and averaged over $t = 15T_L$.

The maximum of Co is set to 2, and the condition $Co \leq 1$ is, in general, respected.

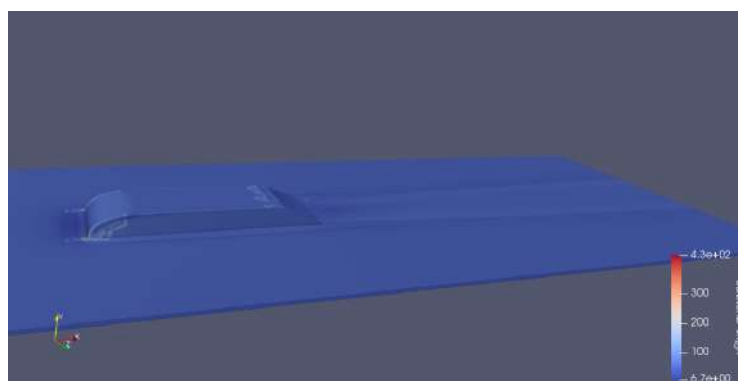


Figure 3.71: DES 3D Mesh 2 - The value of y^+ is generally good and mostly under 50

Pressure coefficient results

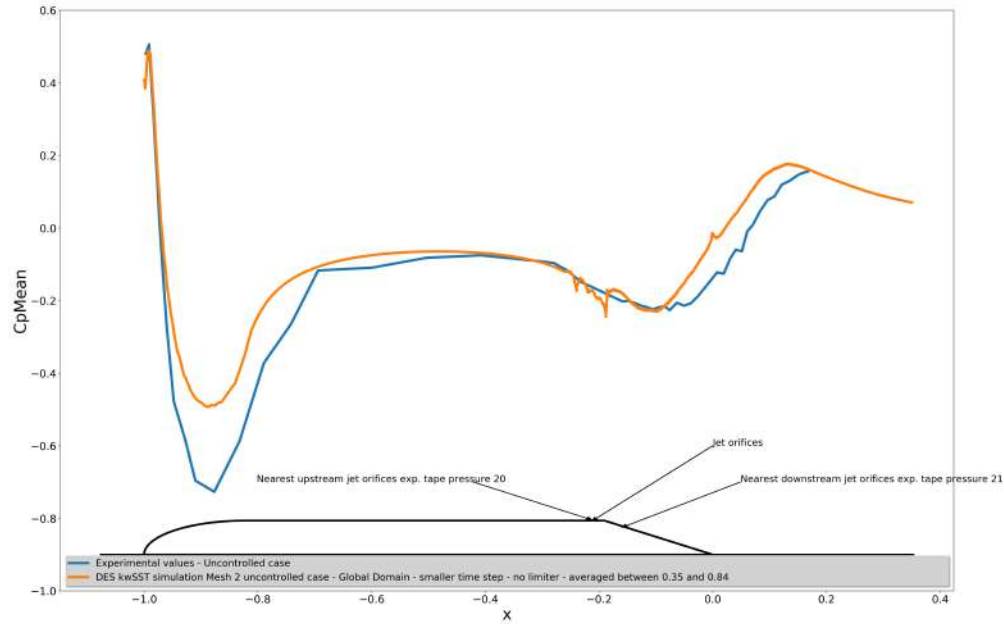


Figure 3.72: Pressure coefficient middle plane $z=0$ - DES 3D kwSST simulations Mesh 2 and experimental data - uncontrolled case.

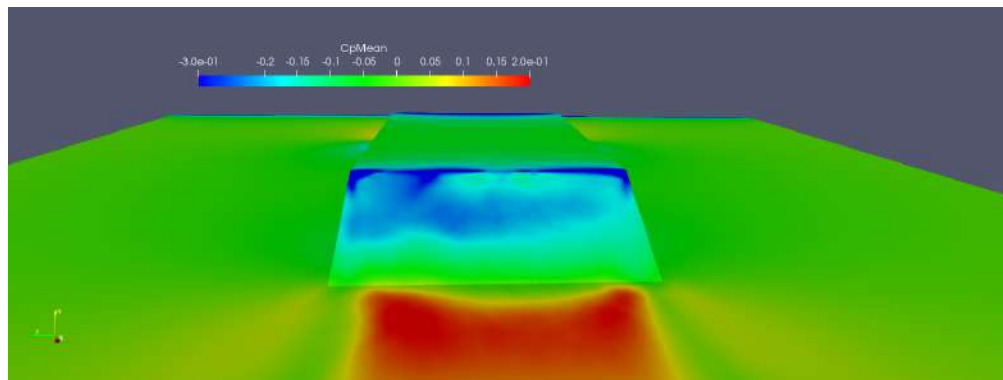


Figure 3.73: Pressure coefficient at the rear of the shape on the ramp - DES 3D kwSST simulations Mesh 2 - uncontrolled case.

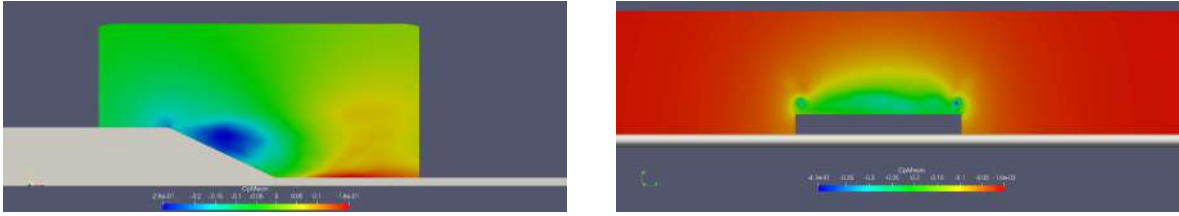


Figure 3.74: Pressure coefficient middle plane $z=0$ (left) and transverse plane $x=1.53$ m (right) - DES 3D kwSST simulations Mesh 2 - uncontrolled case.

Mean flow topology results

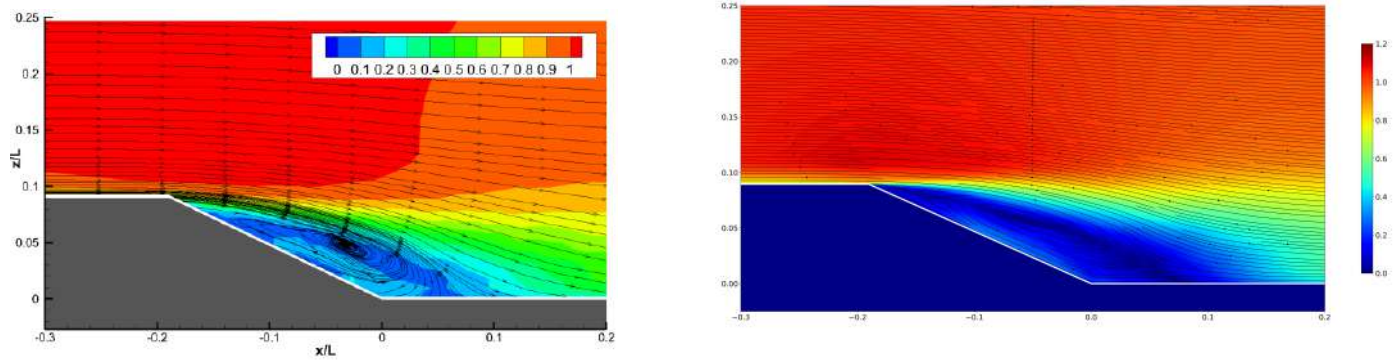


Figure 3.75: Streamline mean adimensional velocity middle plane $z=0$ - Experimental data distance of reattachment $h_r/L = 0.24$ [5] (left) - Streamline mean adimensional velocity middle plane $z=0$ - DES 3D kwSST Mesh 2 distance of reattachment $h_r/L = 0.275$ (right) - uncontrolled case.

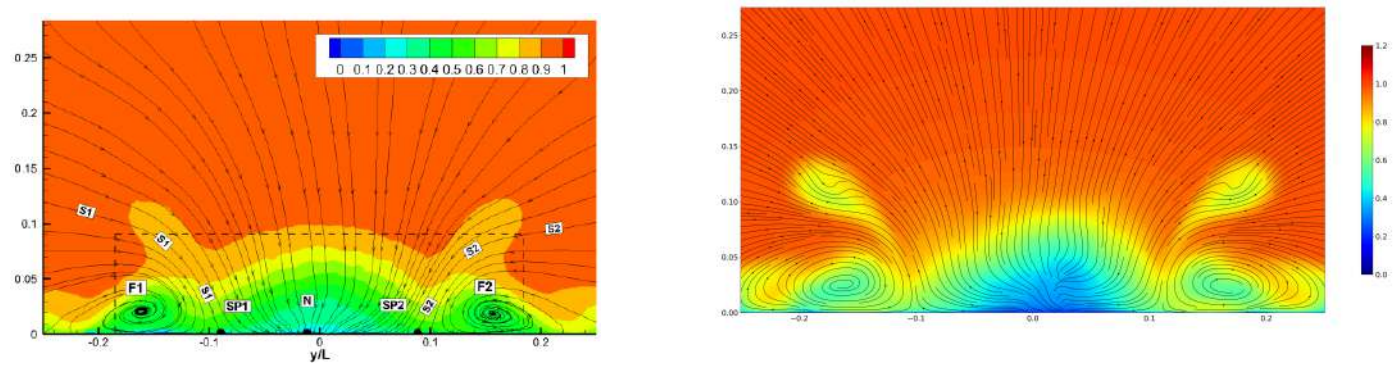


Figure 3.76: Streamline mean adimensional velocity transverse plane $x=1.77$ m - Experimental data [5] (left) - Streamline mean adimensional velocity transverse plane $x=1.77$ m - DES 3D kwSST Mesh 2 (right) - uncontrolled case.

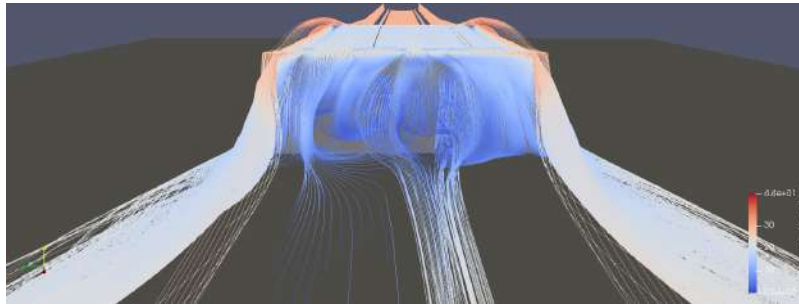


Figure 3.77: UMean streamline at the rear - DES 3D kwSST simulations Mesh 2 - uncontrolled case.

Unsteady flow topology results

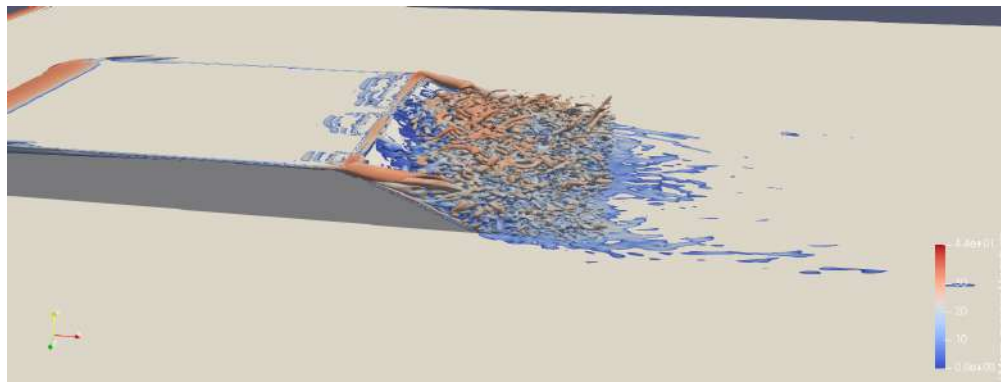


Figure 3.78: Q criterion DES 3D kwSST simulations Mesh 2 - Contour $Q = \frac{4U_\infty^2}{H^2}$ coloured by Umean - uncontrolled case.

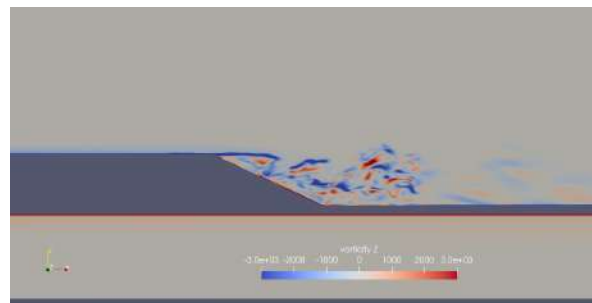


Figure 3.79: Vorticity contour middle plane $z=0$ - DES 3D kwSST simulations Mesh 2 - uncontrolled case.

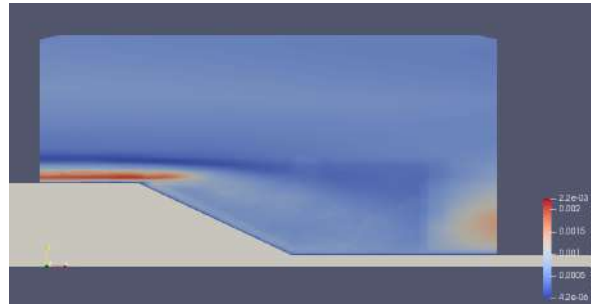


Figure 3.80: ν_t mean middle plane $z=0$ - DES 3D kwSST simulations Mesh 2 - uncontrolled case.

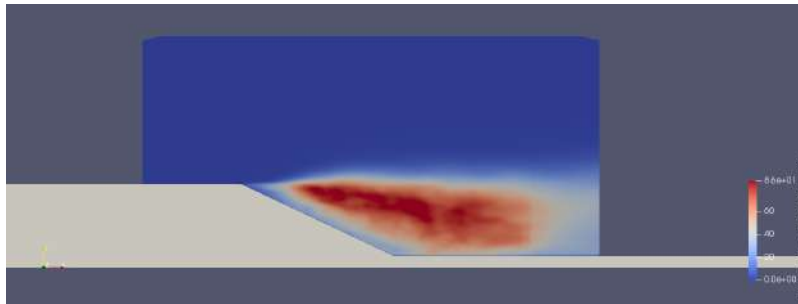


Figure 3.81: Reynolds stress magnitude middle plane $z=0$ - DES 3D kwSST simulations Mesh 2 - uncontrolled case.

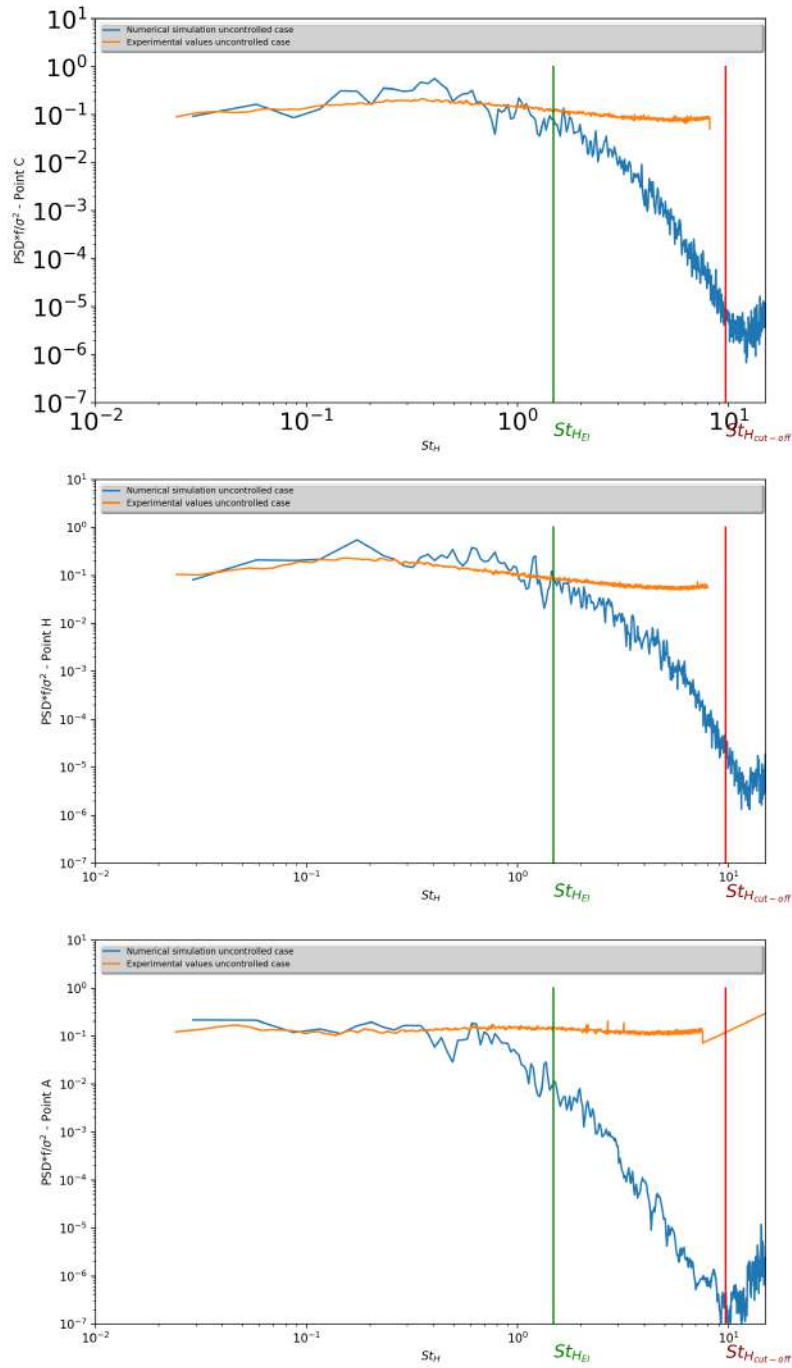


Figure 3.82: Normalised power spectral density of the velocity signal at points C,H,A - DES 3D kwSST simulations Mesh 2 and experimental values [5] - uncontrolled case.

Drag coefficient

	ReL10-6	CD Uncontrolled flow
Experimental estimation	2,35	0,206
Numerical simulation DES mesh2 Global Domain	2,35	0,1715

Figure 3.83: C_D value at the rear slant comparison DES kwSST 3D mesh 2 global domain simulation and experiment - uncontrolled case.

3.4.9 Discussion

The DES technique obtained a significantly better solution than with the RANS one, with non significant asymmetry and a better recovery of pressure down-flow from the ramp (see figures 3.46 and 3.24 for the mesh 1 and 3.72 and 3.35 for the mesh 2). Coherent turbulent structures were not represented with the RANS solution and better highlighted in the case for the DES technique, especially in the mixing layer (see figures 3.52, 3.53, 3.30 and 3.31 for the mesh 1 and 3.78, 3.79, 3.41 and 3.42 for the mesh 2). Furthermore, the RANS simulation on mesh 2 do not converge towards a potentially representative solution.

For the DES solution on mesh 1, the traversal recirculation bubble was too developed, and the two longitudinal vortices were too weak (see figures 3.50 and 3.49). The spectral density of the velocity magnitude of the unsteady flow was under developed for high frequencies and small vortices, with a long dissipative recovery zone between the cut-off frequency and the energetic structures (see figure 3.56). The turbulent structures linked with the ramp geometry ($Q = \frac{4U_\infty^2}{H^2}$) are not well represented. The mesh is not fine enough to correctly capture the energy of the coherent turbulent structures over l_{EI} , as discussed in the section 3.2.3. The solution obtained for the mean flow and unsteady flow is not satisfying with this mesh refinement.

The attempt of a quick simulation on the mesh 2 with a large time step and a limiter on the gradient for ω was inconsequential with a poor representation of the C_p on the body (see figures 3.59 and 3.60) and with an under developed recirculation bubble (see figure 3.62)

The DES simulation on the mesh 2 with smaller time steps and without a limiter on the gradient is interesting, with a suitable match between the C_p curve obtained by calculation and the experimental results (see figure 3.72) despite an optimistic pressure recovery near the reattachment zone. The reattachment distance of the recirculation bubble was closer to that estimated experimentally, and the two longitudinal vortices were well represented (see figure 3.75 and 3.76). For the unsteady flow, the turbulent structures linked with the ramp geometry became more present, and the spectral densities of the velocity were more energetic and corresponded better to the experimental densities over l_{EI} (see figures 3.78 and 3.82).

The pressure present at the front of the body was less pronounced in numerical solutions than what was obtained by wind tunnel experimental measurements.

We can observe, in all the solutions obtained, peaks of low pressure just after the separation zone, more or less present, on the middle longitudinal plane and not detected experimentally. The value of the drag coefficient approximates that estimated experimentally. It is higher, probably related to low pressure peaks not shown by experience.

3.5 Restrict domain simulations - uncontrolled case

In this section, we test the DES technique on the mesh 2 in a restrict domain and compare the results obtained with the ones of the preceding section. We also examine the behaviour of the Sparlat-Allmaras model with a DES technique on the mesh 2.

3.5.1 Computational domain

To compute a precise solution within the timeframe of this internship, we had to restrict the domain that was simulated and focus on the regions of interest such as the rear of the ramp. We also had to capture small structures to obtain statistical data that are comparable to the experimental data and able to interact with the eddies generated by the impulsed jets.

The domain we considered is defined as follows (see figure 3.84). It is more than three times smaller than the domain considered in the chapter 3.4. It allows a 0.43 metre distance after the inlet and before the shape rupture and the flow separation for the development of natural turbulence and 2,5 metres after for the development of the mixing layer.

The plane $x=1$ metre corresponds then here to the inlet domain.

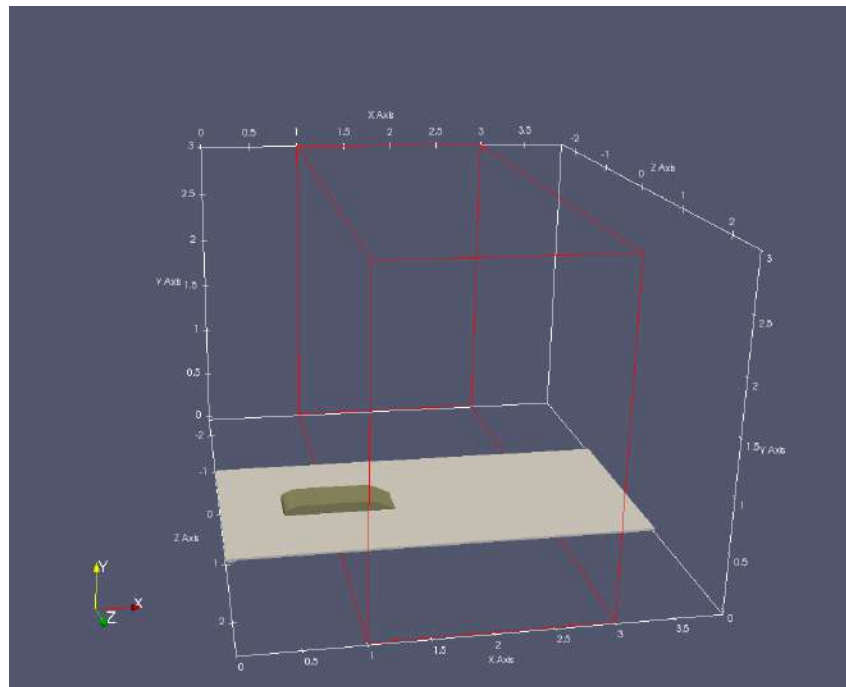


Figure 3.84: Restrict domain 5 m x 3 m x 2 m

3.5.2 Mesh

The mesh used is the mesh 2 for the uncontrolled case (see chapter 3.2.4).

3.5.3 Schemes

All the schemes used are second-order schemes, without a limiter.

The estimation of values on the faces cells is done with a linear interpolation of the centres cells computed values.

The estimation of the gradient on the faces cells for Laplacian scheme is corrected in the case of non-orthogonal mesh.

The time scheme is transient, second order implicit for the DES calculations.

3.5.4 Resolution

Time-dependent equations are resolved with iterative methods and Gauss-Seidel smoother, while the Poisson's equation resolution of the pressure is done with preconditioned techniques or with a geometric-algebraic multi-grid solver (GAMG) to gain in performance in the case of a small time step.

3.5.5 Boundary conditions

We were confronted to the problem of the boundary conditions, especially those concerning the inlet conditions.

For the boundary layers, we assumed we were in a RANS zone of the DES method (see chapter 3.4.1).

For the outlet boundary, a simple Neumann zero gradient condition was considered.

Therefore, all the settings could be taken from the boundary of the global domain simulations (see chapter 3.4.1), except for the inlet settings. The zone of this boundary is situated in the middle of the wind-tunnel section where the mean flow and the turbulence (even the one related to the geometry of the problem) develop. We had to focus on this issue to define correct conditions able to give us a solution that matched the physical solution. This is the object of the following section.

Turbulent inlet boundary conditions

As discussed in the chapter 2.4.2, we considered setting at the entry values obtained in the global domain simulations for the mean flow.

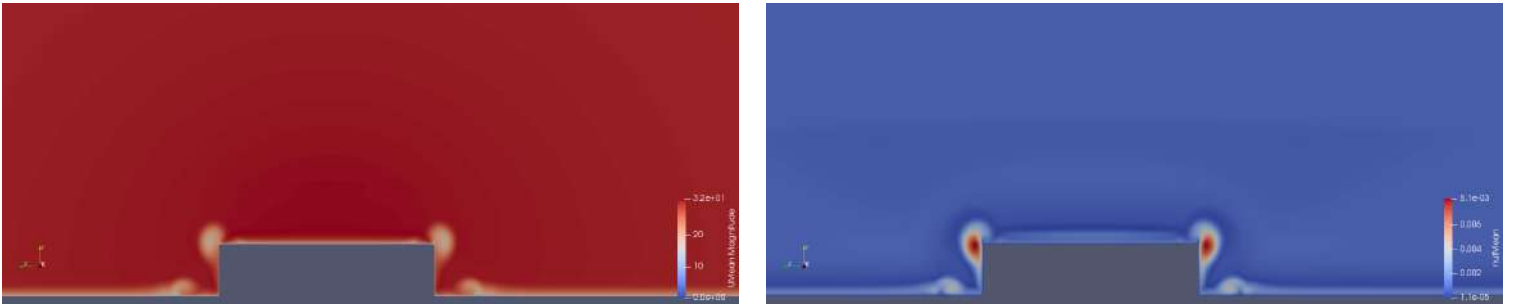


Figure 3.85: UMean inlet boundary conditions(left) - ν_t inlet boundary conditions(right)

The principal issue then is the generation of fluctuations at the inlet that come as close to the solution as possible.

Many techniques exist to simulate turbulent inlet boundary conditions as described by Danet [2] and Immer [3].

The first of these techniques can be grouped together in methods with physical turbulent generation.

- The Laminar-turbulent transition method sets laminar conditions far at the front of the zone. We need that turbulence and fluctuations develop.
- The cyclic domain or drive domain method requires a geometrical periodic entry domain. This is not the case in this study.

The second group of methods is related to synthetic turbulence, that is, generated through a model straight at the inlet of the domain without pre-zone or pre-calculation. We are interested in the filtered noise methods principally because they are implemented in OpenFOAM.

The filtered noise method corresponds to a random Gaussian white noise used with a filter to obtain time and space correlations (see Immer [3] for details).

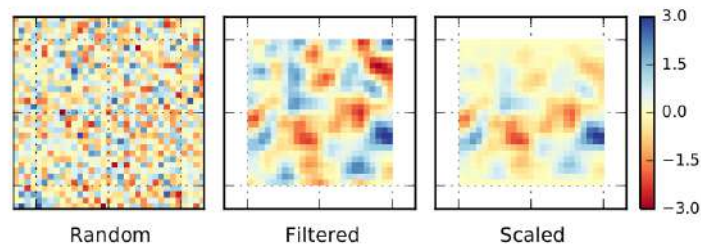


Figure 3.86: Different steps of turbulent inlet BC generation [3]

To illustrate the technique, we can consider the generation in space of turbulent structures for a one dimensional problem:

The first step of this method is to generate a random uncorrelated fluctuation signal η for the velocity with no reference to the flow, more specifically, uniform distributed.

Then, to obtain coherence in space turbulent structures, a numerical filter is applied to η :

$$f_m = \sum_{n=0}^N b_n \eta_{m+n}$$

where N is the number of points from the compute domain. For a Gaussian filter, b_n can be set as $b_n = e^{-\frac{\pi n^2}{2l_{filter}^2}}$, with l_{filter} being the turbulence length scale.

These structures have to be scaled to the physical problem. This is done through the Reynolds stress (for a 2D-3D problem it is also a mean to correlate the different components from η)

This technique of inlet turbulence modelling corresponds in OpenFOAM to a function called *turbulentDFSEMinlet*.

The main fluctuations at the inlet come from the two transverse vortices generated by the front vertical edges of the body (see figure 3.52)

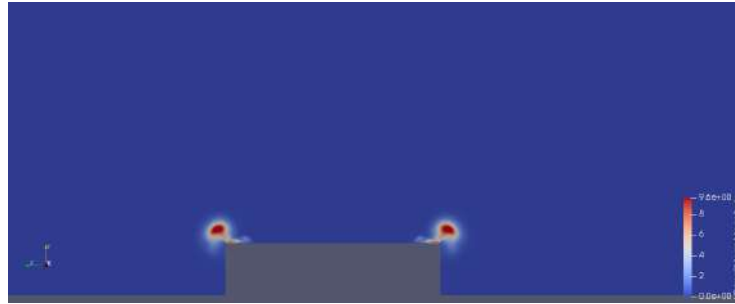


Figure 3.87: Reynolds stress at $x=1$ m from the DES global domain simulations

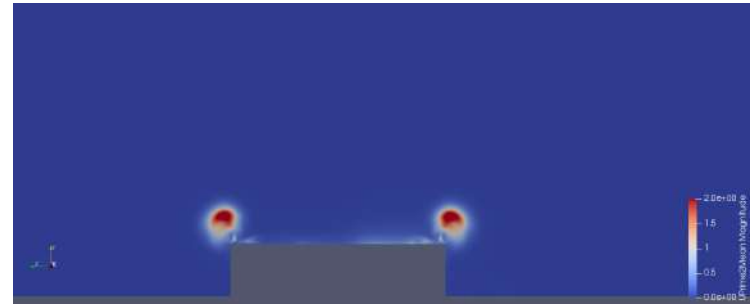
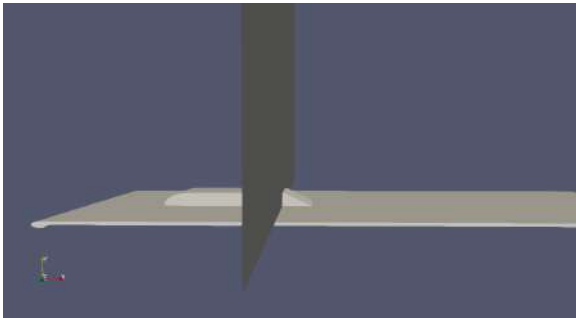


Figure 3.88: Plane $x=1.42$ m (left) - Reynolds stress magnitude at $x=1.42$ m from the DES global domain simulations (right)

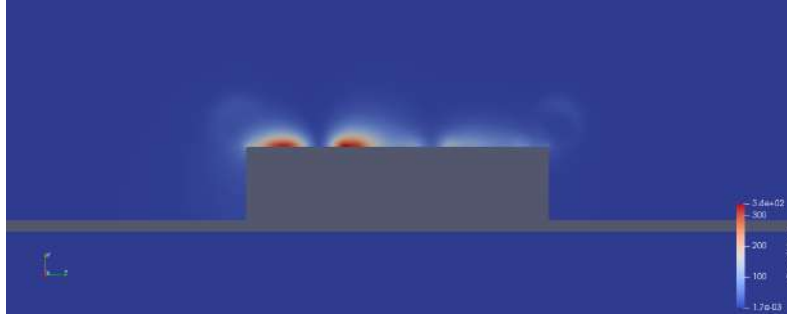


Figure 3.89: Plane $x=1.42$ m (left) - Pressure fluctuations magnitude at $x=1.42$ m from the DES global domain simulations

The kinetic energy of these fluctuations is in the range of $10m^2/s^{-2}$ corresponding to 10% of turbulence and becomes weaker approaching the separation zone at $x=1.42$ with 5% of turbulence.

The turbulence fluctuations at $x=1.42$ metre in the boundary layer are in the range of 3%.

To determine the influence of the synthetic turbulence at the inlet, we first set at the entry of the restrict domain the mean flow values coming from the simulations on the global domain without synthetic fluctuations. We make consequently a strong assumption that the turbulence developed sufficiently well in the boundary layers within 0.43 metre before the separation. Then a second run was conducted with inlet synthetic turbulence.

3.5.6 DES 3D simulation - Mesh 2 - Sparlat-Allmaras - without inlet synthetic turbulence

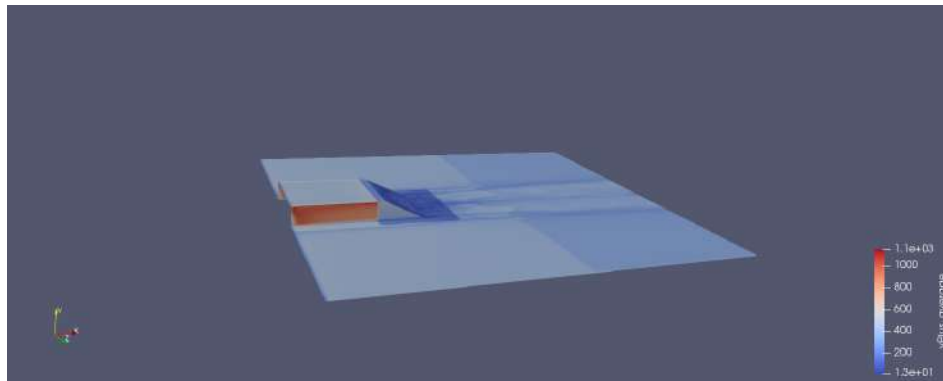
Conditions of the run

The model of turbulence used for the subgrid scales and the boundary layers is the Sparlat-Allmaras model.

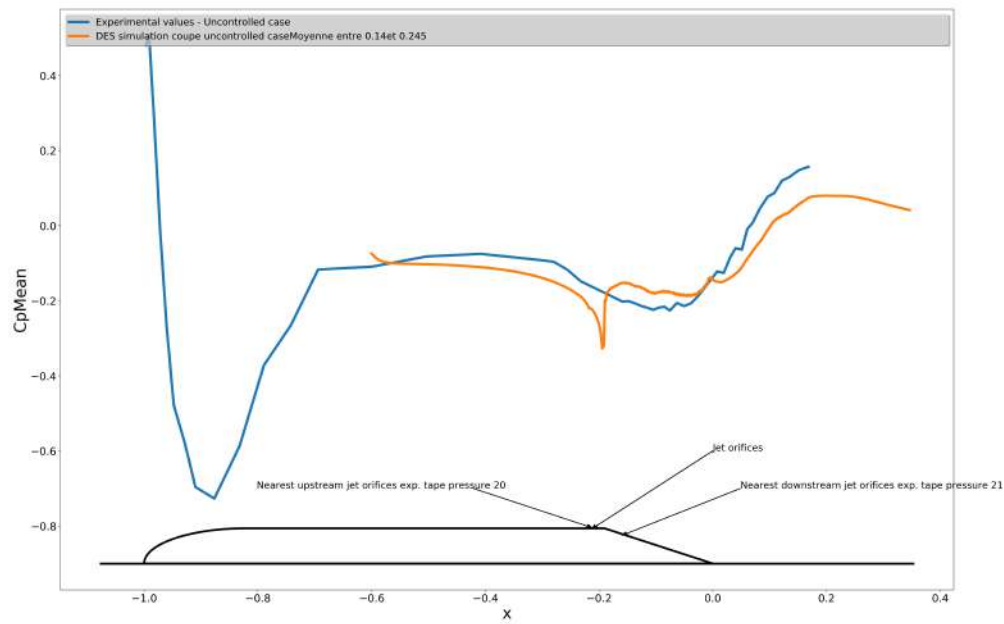
The solution for the mean flow is reached when the C_p profile curve at the middle plane is relatively stable for an $1T_L$ average pressure.

The solution presented below is obtained after $t = 6T_L$ and averaged over $t = 5T_L$.

The condition $Co \leq 1$ is globally respected, thus avoiding numerical dissipation for hyperbolic equations.

Figure 3.90: DES 3D Mesh 2 - Values of y^+

Pressure coefficient results

Figure 3.91: Pressure coefficient middle plane $z=0$ - DES 3D Sparlat Allmaras simulations Mesh 2 and experimental data - uncontrolled case.

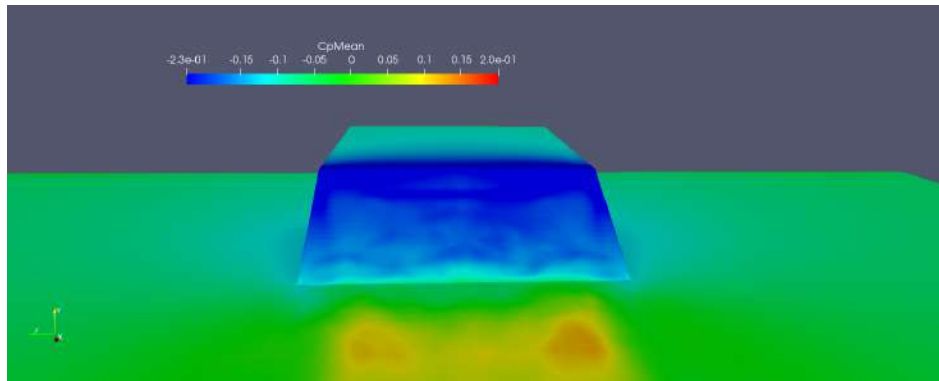


Figure 3.92: Pressure coefficient at the rear of the shape on the ramp - DES 3D Sparlat Allmaras simulations Mesh 2 - uncontrolled case.

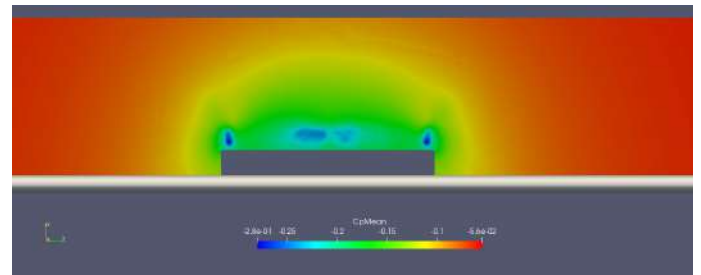
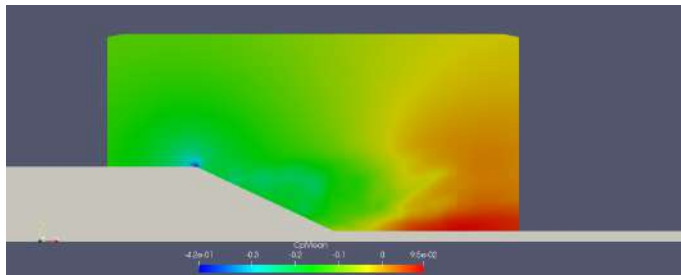


Figure 3.93: Pressure coefficient middle plane $z=0$ (left) and transverse plane $x=1.53$ m (right) - DES 3D Sparlat Allmaras simulations Mesh 2 - uncontrolled case.

Mean flow topology results

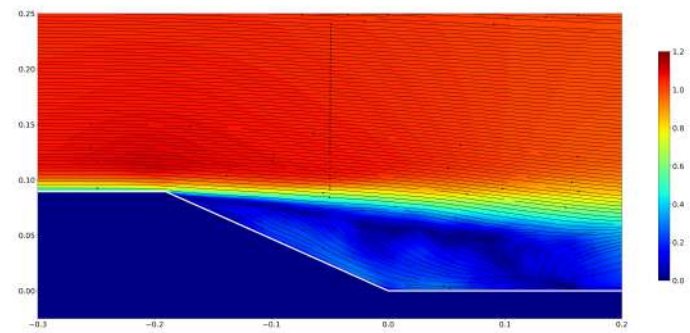
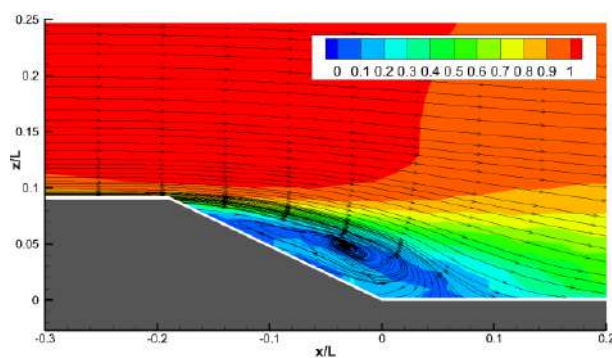


Figure 3.94: Streamline mean adimensional velocity middle plane $z=0$ - Experimental data distance of reattachment $h_r/L = 0.24[5]$ (left) - Streamline mean adimensional velocity middle plane $z=0$ - DES 3D Sparlat Allmaras Mesh 2 distance of reattachment $h_r/L = 0.350$ (right) - uncontrolled case.

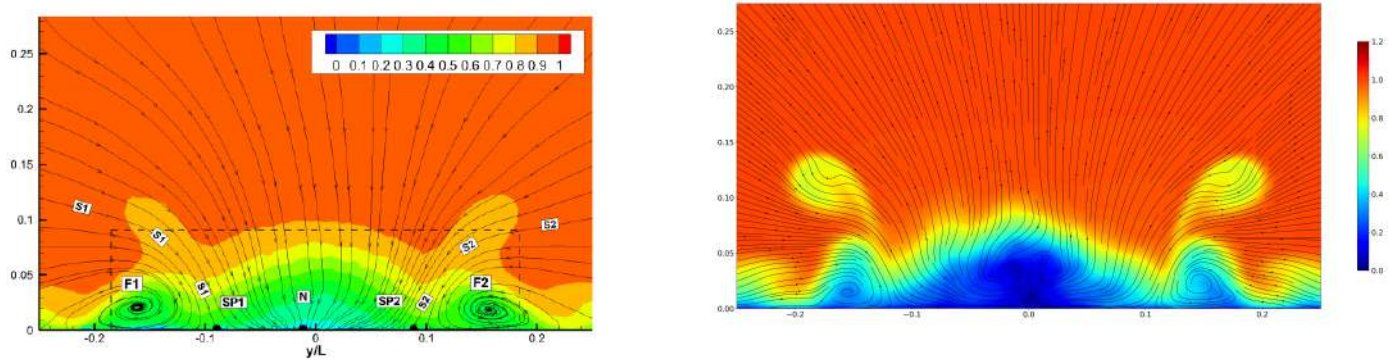


Figure 3.95: Streamline mean adimensional velocity transverse plane $x=1.77$ m - Experimental data [5] (left) - Streamline mean adimensional velocity transverse plane $x=1.77$ m - DES 3D Sparlat Allmaras Mesh 2 (right) - uncontrolled case.

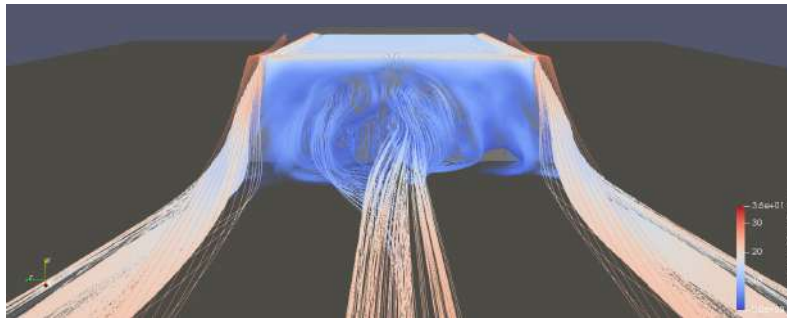


Figure 3.96: UMean streamline at the rear - DES 3D Sparlat Allmaras simulations Mesh 2 - uncontrolled case.

Unsteady flow topology results

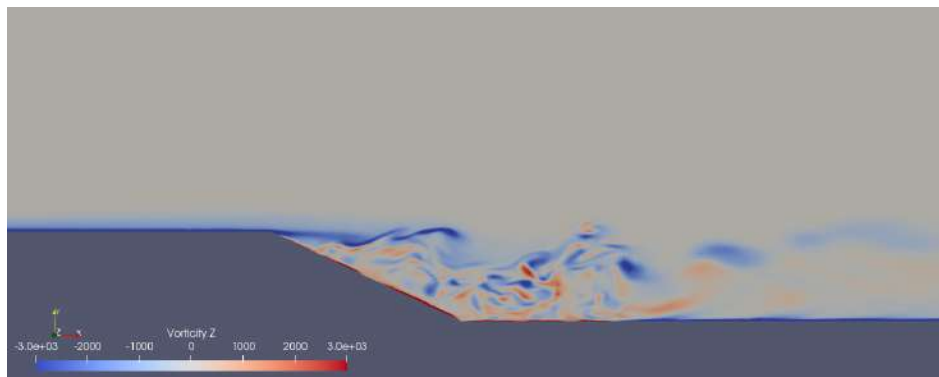


Figure 3.97: Vorticity contour middle plane $z=0$ - DES 3D Sparlat-Allmaras simulations Mesh 2 - uncontrolled case.

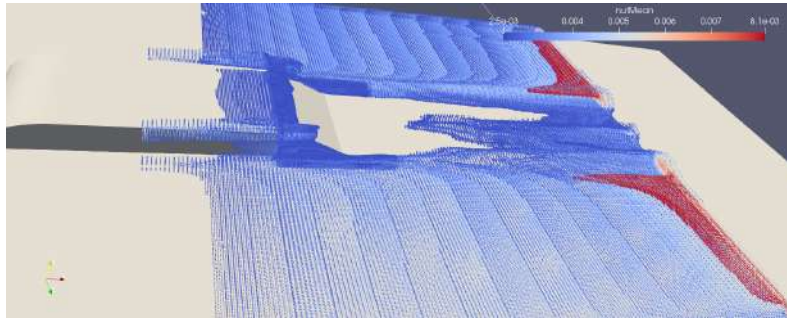


Figure 3.98: nut mean values over $2.5 \times 10^{-3} m^2/s$ at the rear - DES 3D Sparlat-Allmaras simulations Mesh 2 - uncontrolled case.

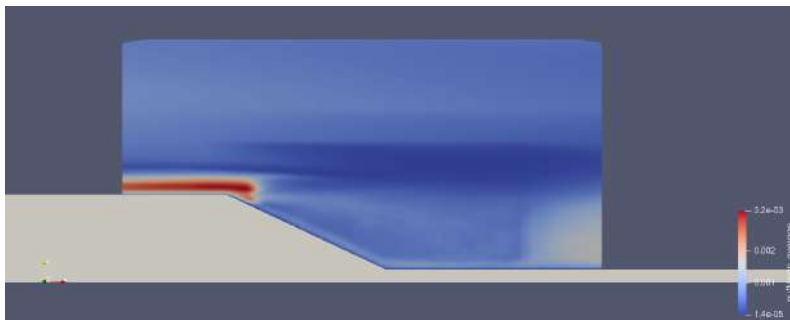


Figure 3.99: nut mean middle plane $z=0$ - DES 3D Sparlat-Allmaras simulations Mesh 2 - uncontrolled case.

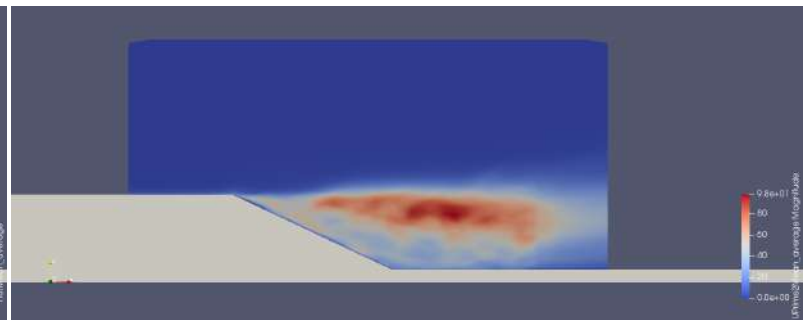


Figure 3.100: Reynolds stress magnitude middle plane $z=0$ - DES 3D Sparlat-Allmaras simulations Mesh 2 - uncontrolled case.

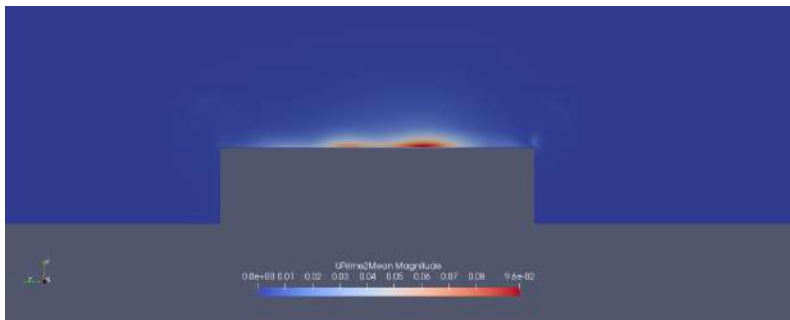


Figure 3.101: Reynolds stress magnitude plane $x=1.42$ - DES 3D Sparlat-Allmaras simulations Mesh 2 - uncontrolled case.

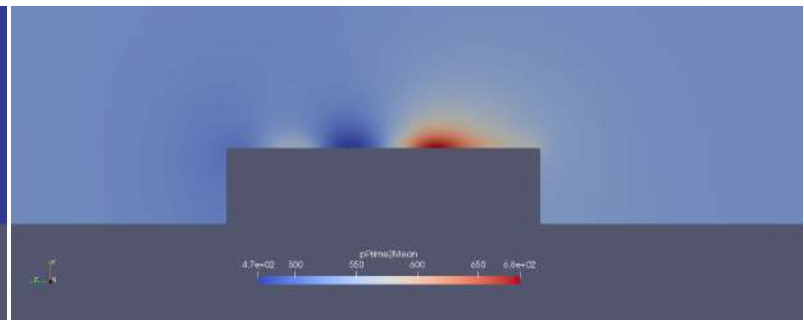


Figure 3.102: Pressure fluctuation magnitude middle plane $x=1.42$ - DES 3D Sparlat-Allmaras simulations Mesh 2 - uncontrolled case.

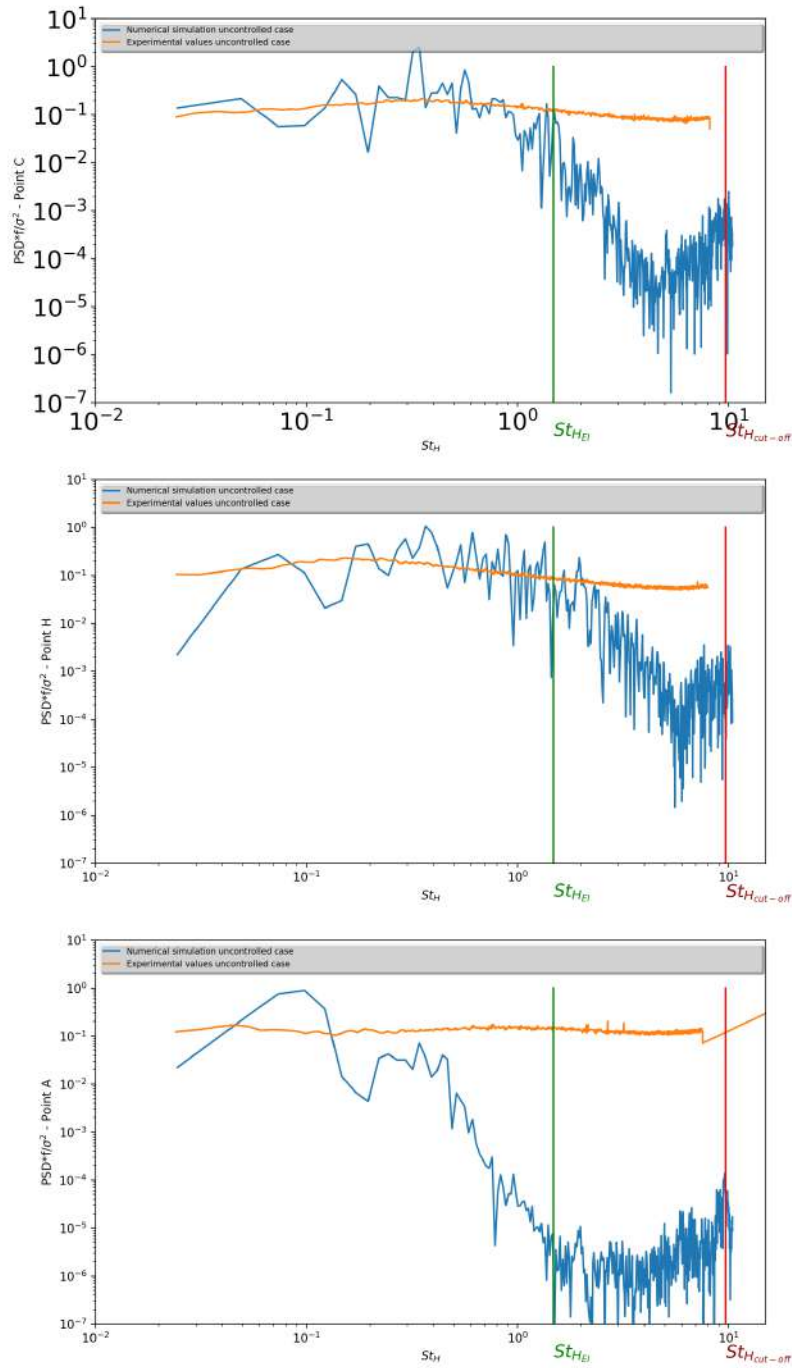


Figure 3.103: Normalised power spectral density of the velocity signal at points C,H,A (see 2.3.4) - DES 3D kwSST simulations Mesh 2 and experimental values [5] - uncontrolled case.

3.5.7 DES 3D simulation - Mesh 2 - kwSST - without inlet synthetic turbulence

Conditions of the run

The model of turbulence used for the subgrid scales and the boundary layers is the kwSST model.

The solution for the mean flow is reached when the C_p profile curve at the middle plane is relatively stable for an $1T_L$ average pressure.

The solution presented below is obtained after $t = 6T_L$ and averaged over $t = 7T_L$.

The condition $Co \leq 1$ is globally respected, thus avoiding numerical dissipation for hyperbolic equations.

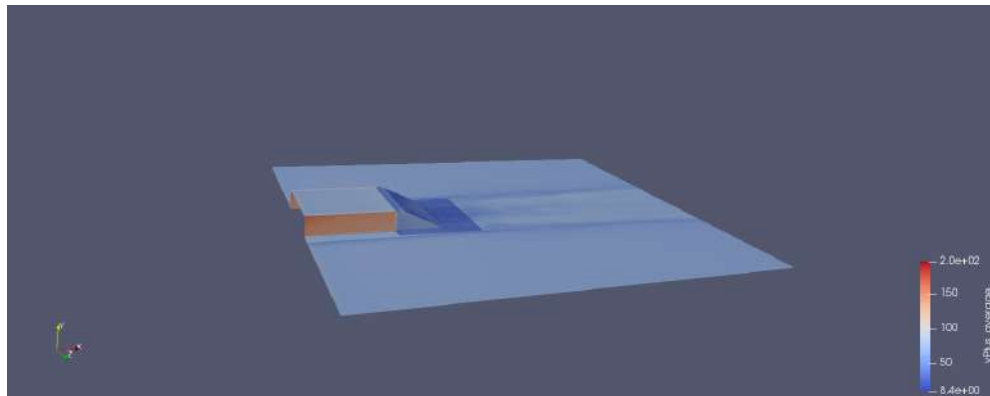


Figure 3.104: DES 3D Mesh 2 - The value of y^+ is generally good and mostly under 50

Pressure coefficient results

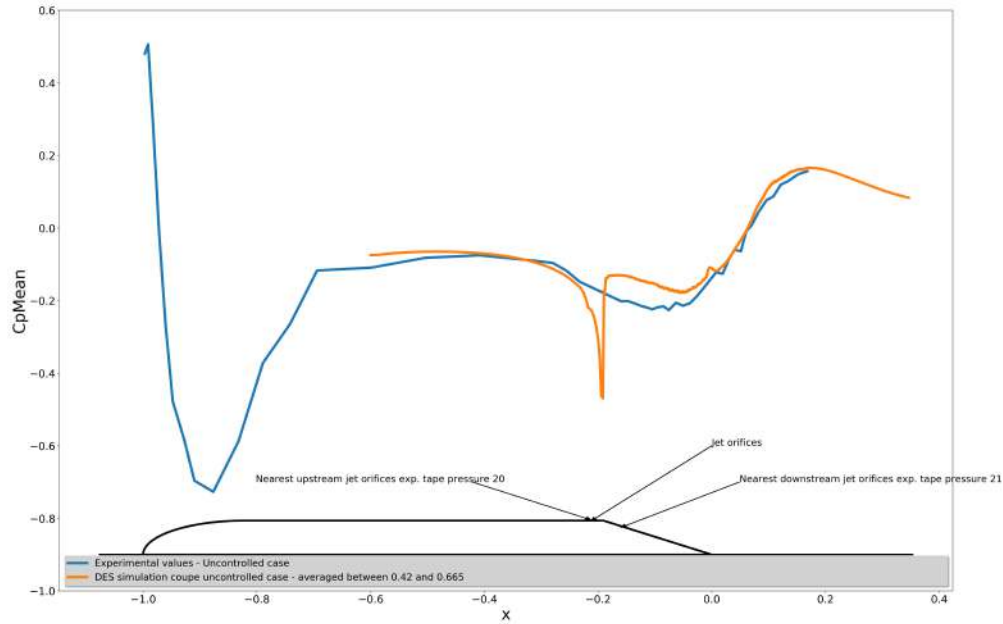


Figure 3.105: Pressure coefficient middle plane $z=0$ - DES 3D kwSST simulations Mesh 2 and experimental data - uncontrolled case.

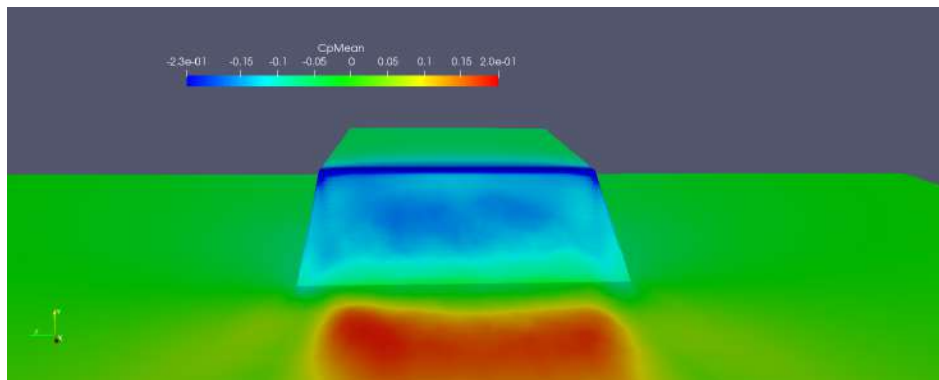


Figure 3.106: Pressure coefficient at the rear of the shape on the ramp - DES 3D kwSST simulations Mesh 2 - uncontrolled case.

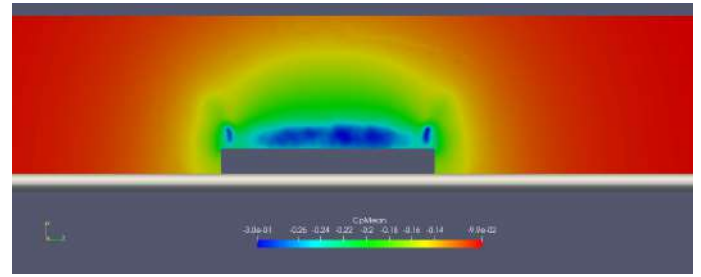
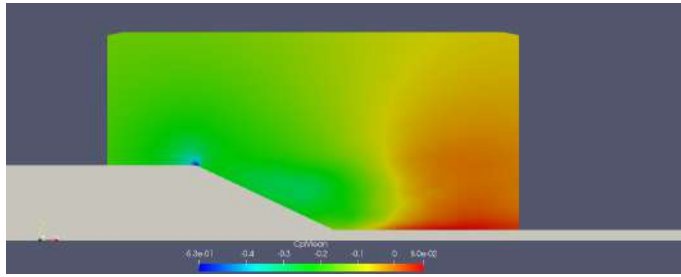


Figure 3.107: Pressure coefficient middle plane $z=0$ (left) and transverse plane $x=1.53$ m (right) - DES 3D kwSST simulations Mesh 2 - uncontrolled case.

Mean flow topology results

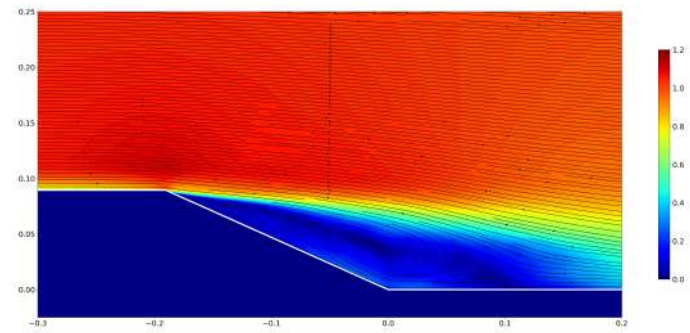
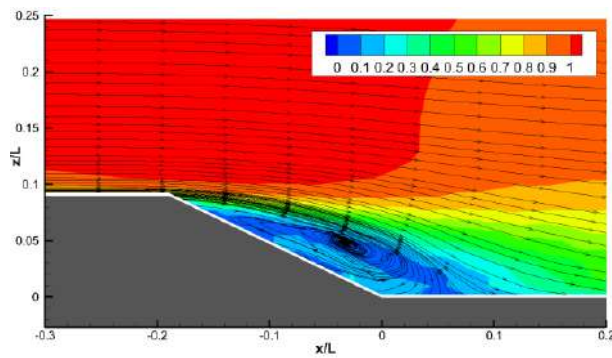


Figure 3.108: Streamline mean adimensional velocity middle plane $z=0$ - Experimental data distance of reattachment $h_r/L = 0.24$ [5] (left) - Streamline mean adimensional velocity middle plane $z=0$ - DES 3D kwSST Mesh 2 distance of reattachment $h_r/L = 0.300$ (right) - uncontrolled case.

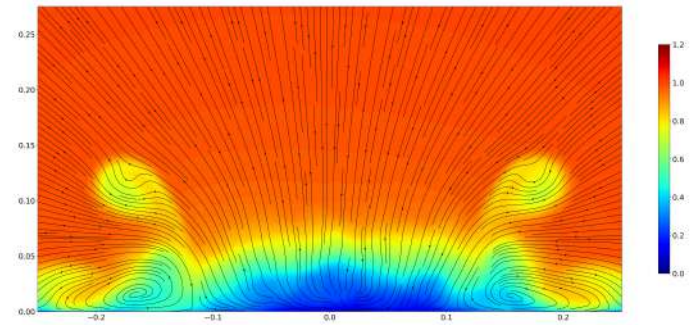
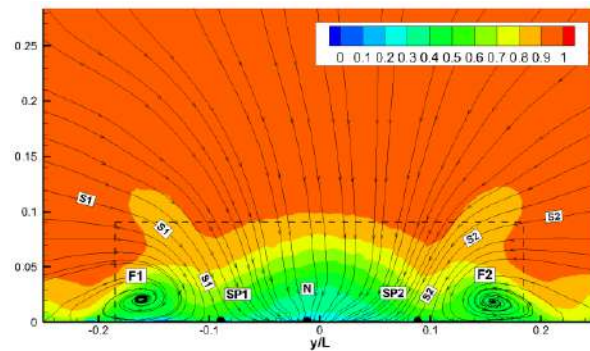


Figure 3.109: Streamline mean adimensional velocity transverse plane $x=1.77$ m - Experimental data [5] (left) - Streamline mean adimensional velocity transverse plane $x=1.77$ m - DES 3D kwSST Mesh 2 (right) - uncontrolled case.

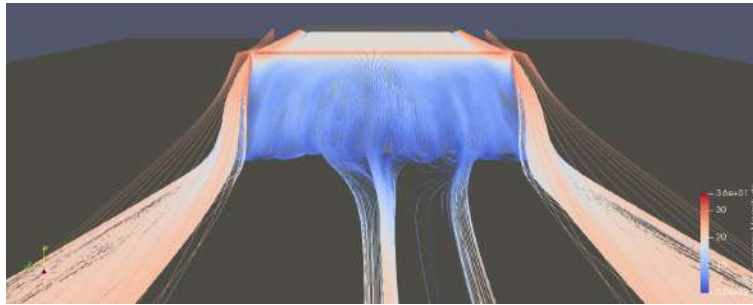


Figure 3.110: UMean streamline at the rear - DES 3D kwSST simulations Mesh 2 - uncontrolled case.

Unsteady flow topology results

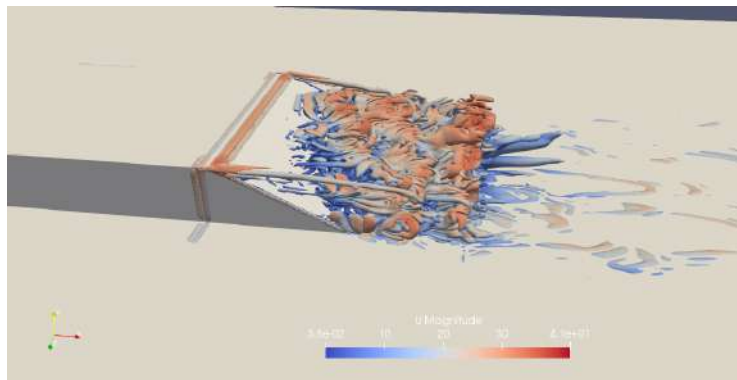


Figure 3.111: Q criterion DES 3D kwSST simulations Mesh 2 - Contour $Q = \frac{4U^2}{H^2}$ coloured by Umean - uncontrolled case.

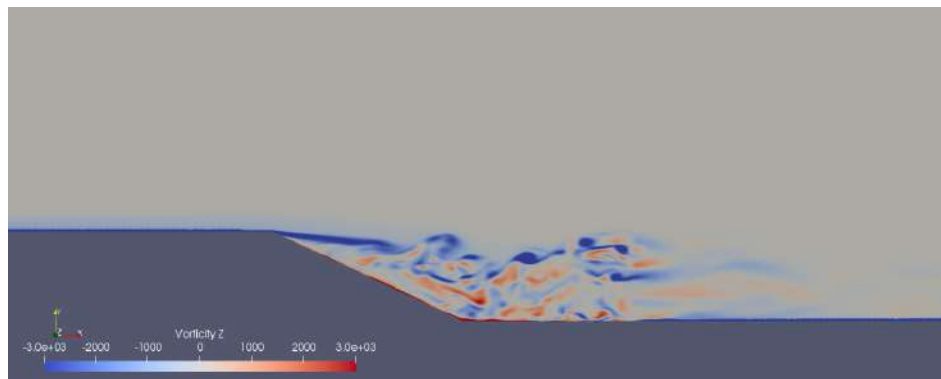


Figure 3.112: Vorticity contour middle plane $z=0$ - DES 3D kwSST simulations Mesh 2 - uncontrolled case.

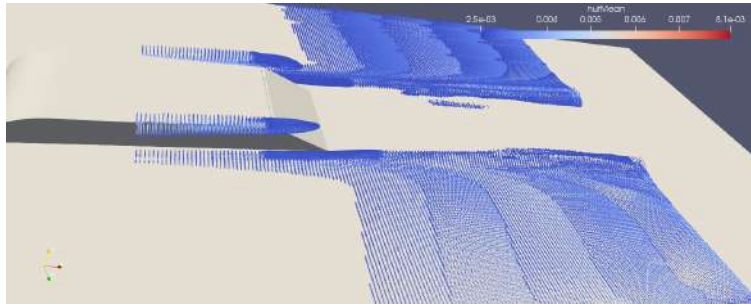


Figure 3.113: nut mean values over $2.5 \times 10^{-3} m^2/s$ at the rear - DES 3D kwSST simulations Mesh 2 - uncontrolled case.

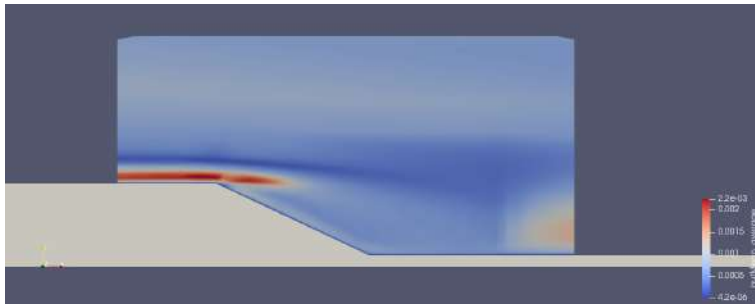


Figure 3.114: nut mean middle plane $z=0$ - DES 3D kwSST simulations Mesh 2 - uncontrolled case.

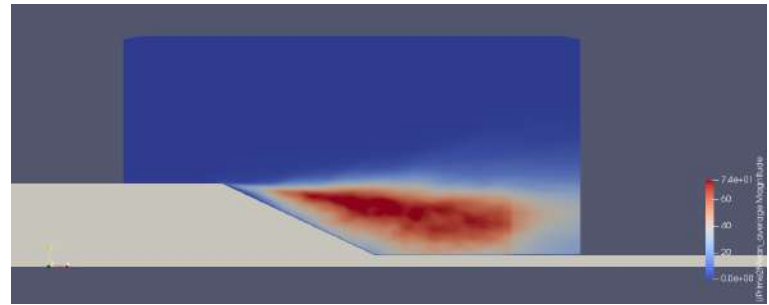


Figure 3.115: Reynolds stress magnitude middle plane $z=0$ - DES 3D kwSST simulations Mesh 2 - uncontrolled case.

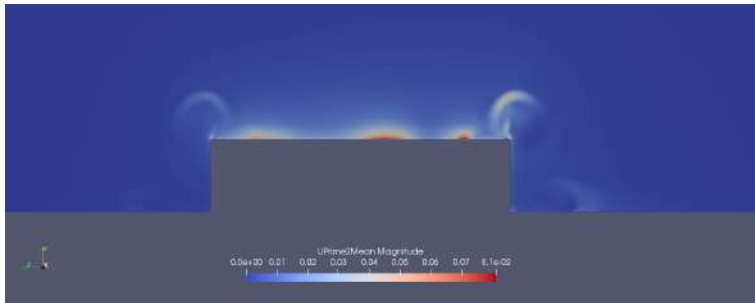


Figure 3.116: Reynolds stress magnitude plane $x=1.42$ - DES 3D kwSST simulations Mesh 2 - uncontrolled case.

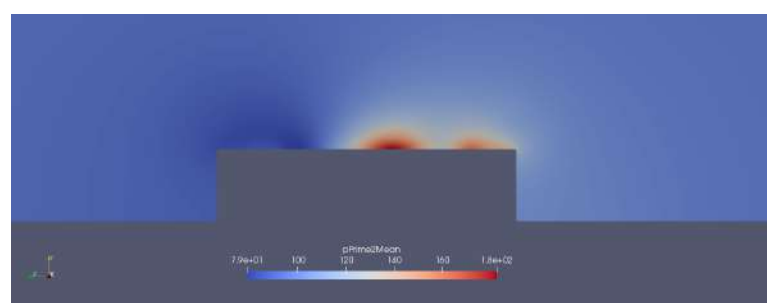


Figure 3.117: Pressure fluctuations magnitude middle plane $x=1.42$ - DES 3D kwSST simulations Mesh 2 - uncontrolled case.

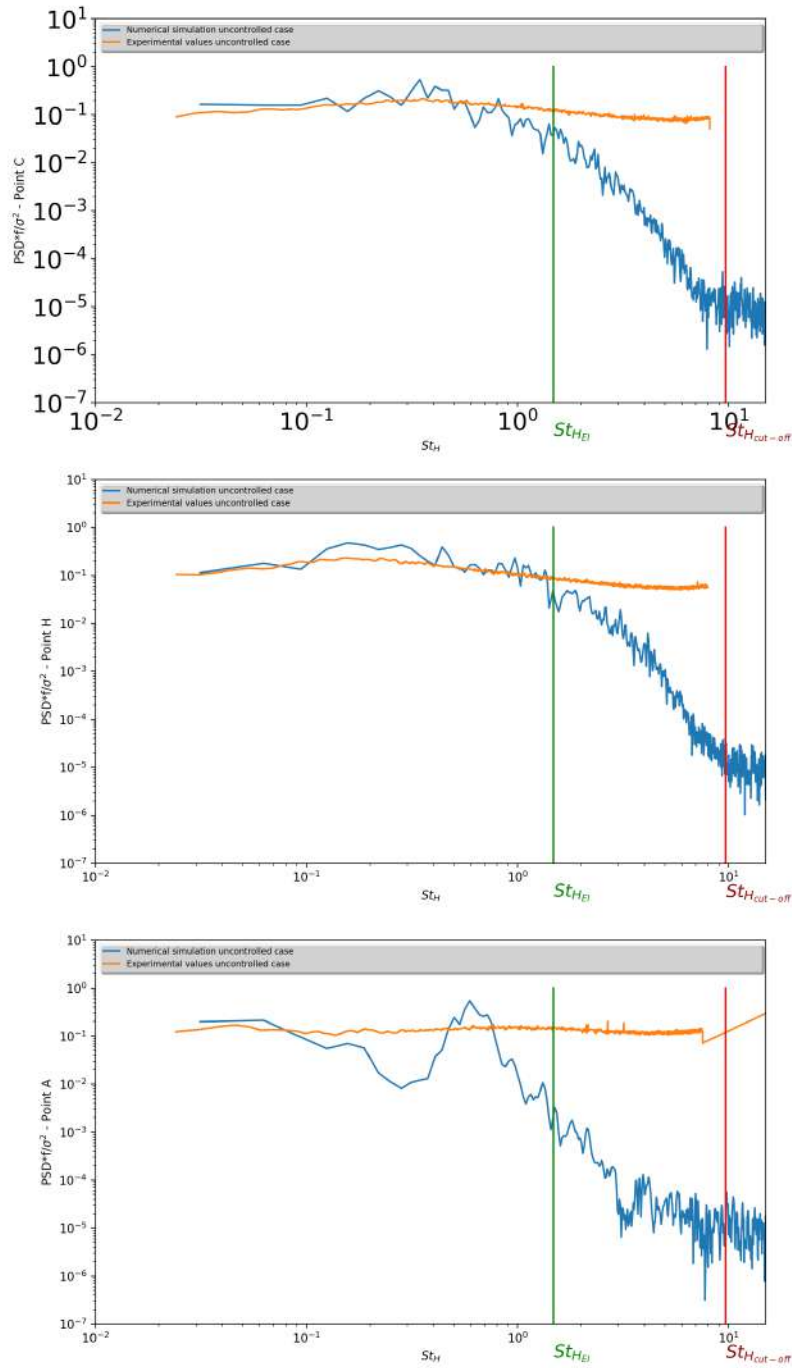


Figure 3.118: Normalised power spectral density of the velocity signal at points C,H,A (see 2.3.4) - DES 3D kwSST simulations Mesh 2 and experimental values [5] - uncontrolled case.

Drag coefficient

	ReL.10-6	CD Uncontrolled flow
Experimental estimation	2,35	0,206
Numerical simulation DES mesh2		
Restrict Domain	2,35	0,242022

Figure 3.119: C_D value at the rear slant comparison DES kwSST 3D mesh 2 restrict domain simulation and experiment - uncontrolled case.

3.5.8 DES 3D simulation - Mesh 2 - kwSST - with inlet synthetic turbulence

Conditions of the run

The model of turbulence used for the subgrid scales and the boundary layers is the kwSST model.

The solution for the mean flow is considered reached when the C_p profile curve at the middle plane is relatively stable for an $1T_L$ average pressure.

The solution presented below is obtained after $t = 13T_L$ and averaged over $t = 18T_L$.

The condition $Co \leq 1$ is globally respected, thus avoiding numerical dissipation for hyperbolic equations.

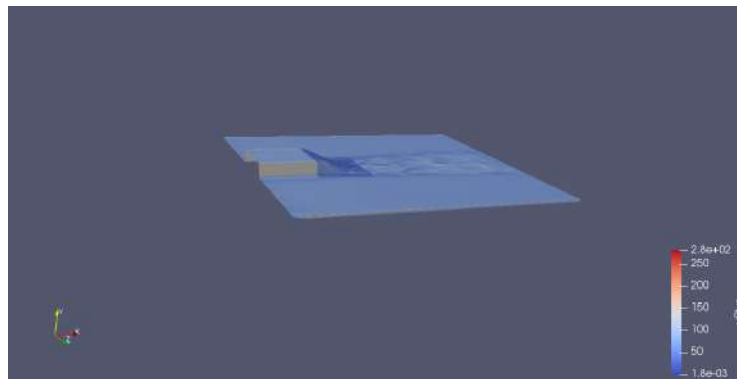


Figure 3.120: DES 3D Mesh 2 - The value of y^+ is generally good and mostly under 50

Pressure coefficient results

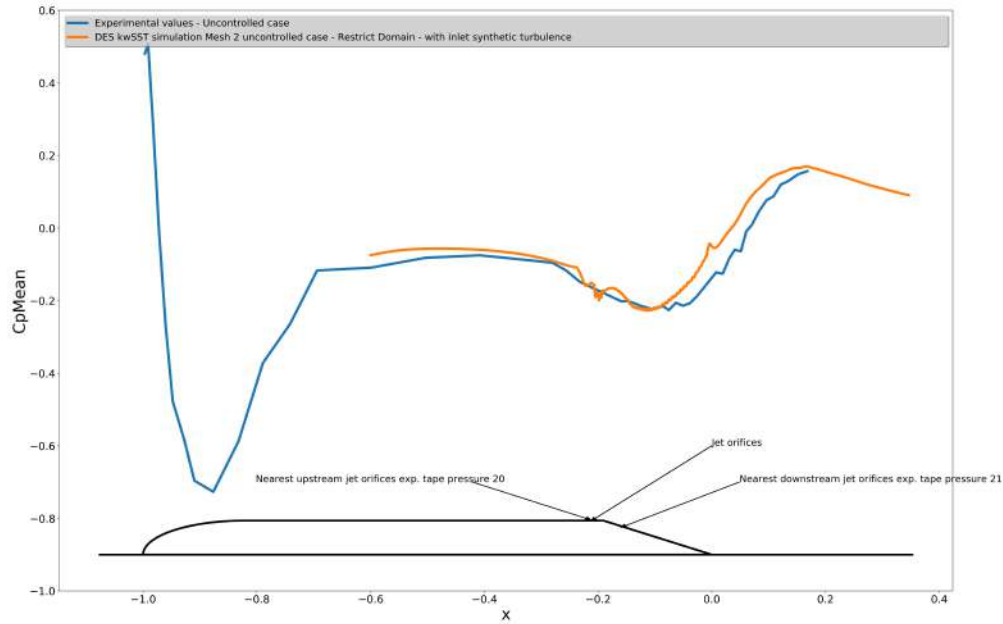


Figure 3.121: Pressure coefficient middle plane $z=0$ - DES 3D kwSST simulations Mesh 2 and experimental data - uncontrolled case.

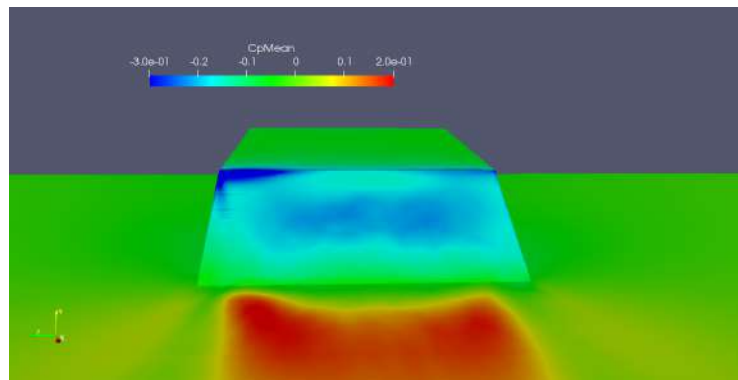


Figure 3.122: Pressure coefficient at the rear of the shape on the ramp - DES 3D kwSST simulations Mesh 2 - uncontrolled case.

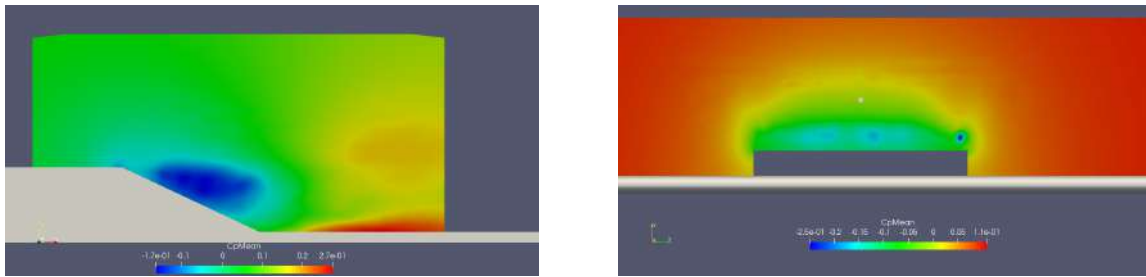


Figure 3.123: Pressure coefficient middle plane $z=0$ (left) and transverse plane $x=1.53$ m (right) - DES 3D kwSST simulations Mesh 2 - uncontrolled case.

Mean flow topology results

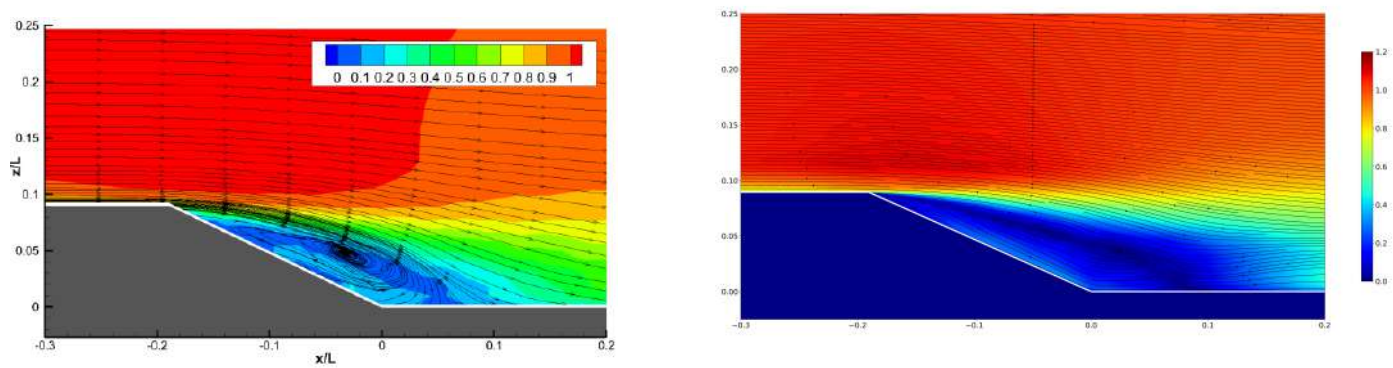


Figure 3.124: Streamline mean adimensional velocity middle plane $z=0$ - Experimental data distance of reattachment $h_r/L = 0.24$ [5] (left) - Streamline mean adimensional velocity middle plane $z=0$ - DES 3D kwSST Mesh 2 distance of reattachment $h_r/L = 0.288$ (right) - uncontrolled case.

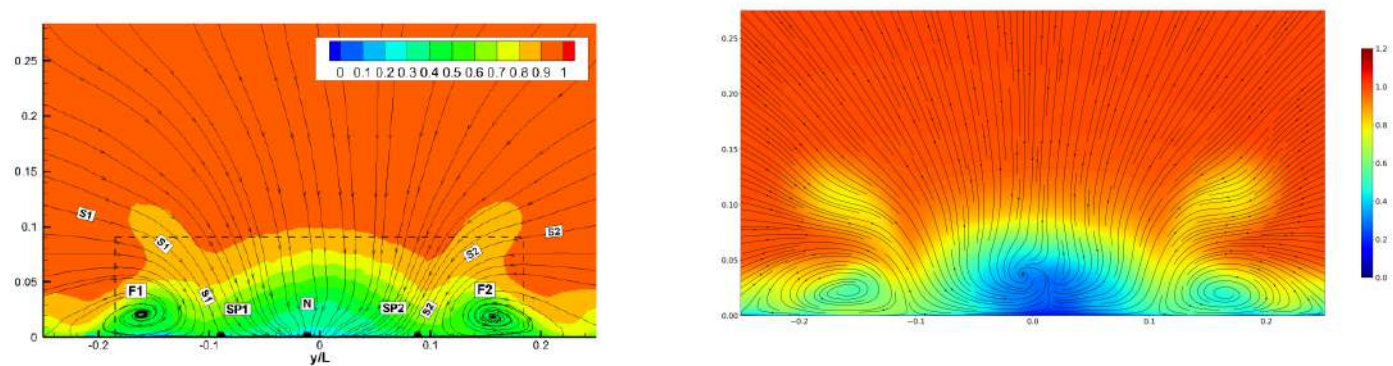


Figure 3.125: Streamline mean adimensional velocity transverse plane $x=1.77$ m - Experimental data [5] (left) - Streamline mean adimensional velocity transverse plane $x=1.77$ m - DES 3D kwSST Mesh 2 (right) - uncontrolled case.

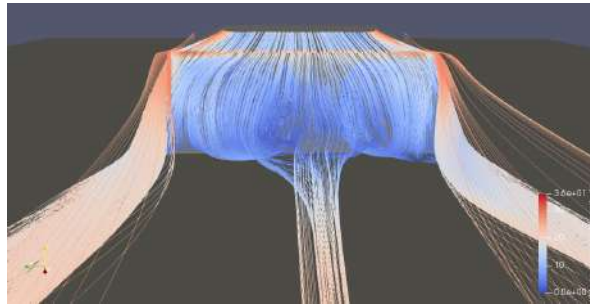


Figure 3.126: UMean streamline at the rear - DES 3D kwSST simulations Mesh 2 - uncontrolled case.

Unsteady flow topology results

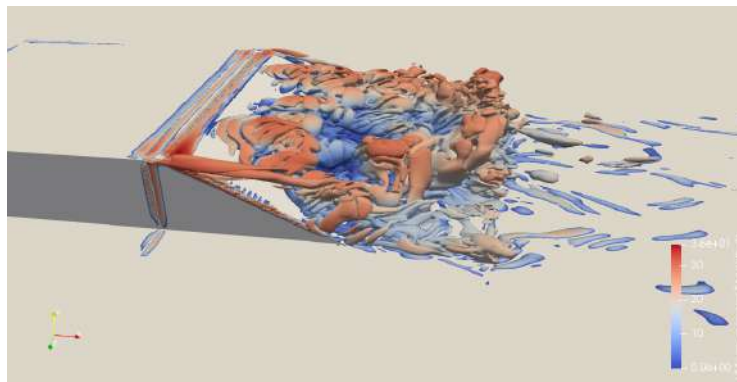


Figure 3.127: Q criterion DES 3D kwSST simulations Mesh 2 - Contour $Q = \frac{4U^2}{H^2}$ coloured by Umean - uncontrolled case.

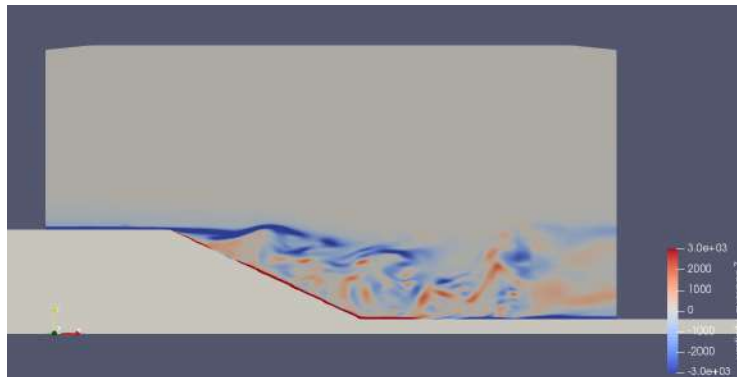


Figure 3.128: Vorticity contour middle plane $z=0$ - DES 3D kwSST simulations Mesh 2 - uncontrolled case.

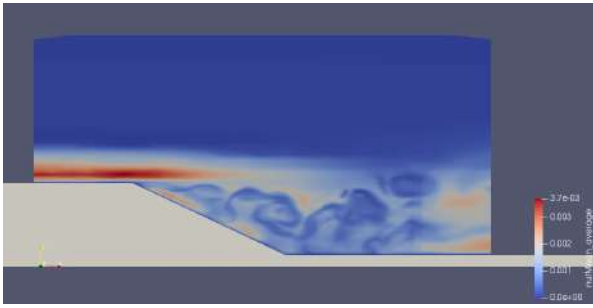


Figure 3.129: nut mean middle plane $z=0$ - DES 3D kwSST simulations Mesh 2 - uncontrolled case.

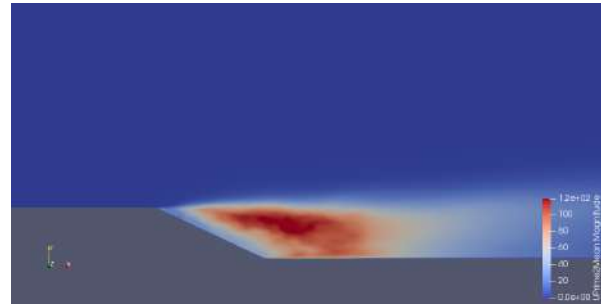


Figure 3.130: Reynolds stress magnitude middle plane $z=0$ - DES 3D kwSST simulations Mesh 2 - uncontrolled case.

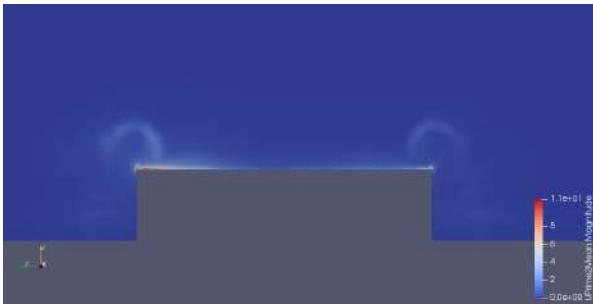


Figure 3.131: Reynolds stress magnitude plane $x=1.42$ - DES 3D kwSST simulations Mesh 2 - uncontrolled case.



Figure 3.132: Pressure fluctuations magnitude middle plane $x=1.42$ - DES 3D kwSST simulations Mesh 2 - uncontrolled case.

Drag coefficient

	ReL.10-6	CD Uncontrolled flow
Experimental estimation	2,35	0,206
Numerical simulation DES mesh2		
Restrict Domain with inlet synthetic turbulence	2,35	0,178

Figure 3.133: C_D value at the rear slant comparison DES kwSST 3D mesh 2 restrict domain simulation and experiment - uncontrolled case.

3.5.9 Discussion

The DES kwSST simulation without synthetic turbulence gives us relatively satisfying results for the mean flow, though an overestimated pressure recovery just after the separation, a marked negative peak of pressure at the separation 3.106, a transverse recirculation bubble slightly overdeveloped 3.108 and weak longitudinal vortices 3.109.

Concerning the unsteady flow, turbulence fluctuations are quite well represented relatively far from the separation (point C and H from the PSD curve 3.118) with correct consideration of the turbulent energy linked with the geometry (in the non universal zone that is, under St_{HEI}).

The results are in fact globally more middling near the separation point with a lake of turbulent energy (point A from the PSD curve 3.118) and turbulent structures (Q criterion 3.111).

Observing and comparing the Reynolds stress fluctuations in the boundary layer of 0.95 % just before the separation at $x=1.42$ metres 3.116 with the fluctuations in the boundary layer of 3 % generated with a simulation on the whole domain 3.88 we can see that we overestimated the assumption of a well-developed turbulence within a distance of 0.43 metre. This likely induced the lake of representative turbulence structures just after the separation and the overestimated pressure recovery of the mean flow in this zone.

The DES Spalart-Allmaras does not seem to be adapted for this configuration of geometry-domain-mesh, given the poor results with a large developed transverse recirculation bubble 3.94, weak longitudinal vortices 3.95 and under-developed turbulence structures compared to the kwSST model 3.103. This model seems to be more dissipative with perhaps as discussed in the section 2.4.4 an overestimated turbulence length of the modeled turbulence.

Synthetic turbulence at the inlet improves the development of turbulent fluctuations just before the separation at $x=1.42$ metre and after with a value of the intensity of turbulence of 10% 3.131, giving a better representation of the C_p around the body, the disappearance of the negative peak of pressure at the separation, and better values of the distance of reattachment. This seems to be the more suitable solution on the restrict domain matching well with the DES kwSST solution for the Mesh 2 on the whole domain.

3.6 Restrict domain simulations - controlled case $f/DC=180\text{Hz}/50$

In this section, we run a DES simulation of the controlled case $f/DC=180\text{Hz}/50$ on the mesh 3 with the kwSST turbulence model.

The results presented here must to be considered with caution given that, to complete the calculations on time, the time step was set to a large value, which degrades the respect of a good CFL condition everywhere on the computational domain - see section 3.6.6 .

3.6.1 Computational domain

The computational domain is the same as the last section 3.5.

3.6.2 Mesh

The mesh used is the mesh 3 for the controlled case (see chapter 3.2.4).

3.6.3 Schemes

The schemes used are the same as the last section 3.5.

3.6.4 Resolution

Time-dependent equations are resolved with iterative methods and Gauss-Seidel smoother, while the Poisson's equation resolution of the pressure is done with a geometric-algebraic multi-grid solver (GAMG) to gain performance.

3.6.5 Boundary conditions

The boundary conditions used are the same as the last section 3.5 with synthetic turbulence at the inlet and a pulsed-jet velocity signal at the jet orifices which is described below.

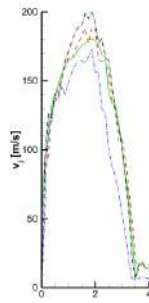


Figure 3.134: Experimental velocity signal in m/s at 1 mm above the exit - controlled case - Experimental data [5] .

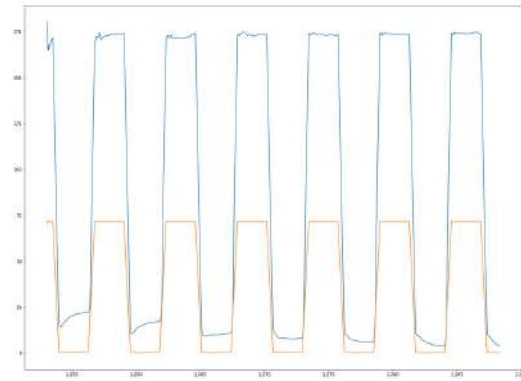


Figure 3.135: Numerical velocity signal in m/s at the ground of the jet orifices (yellow) and 1 mm above the exit (blue) - controlled case $f/DC=180\text{Hz}/50$.

3.6.6 DES 3D simulation - Mesh 3 - kwSST - with inlet synthetic turbulence

Conditions of the run

The model of turbulence used for the subgrid scales and the boundary layers is the kwSST model.

The solution presented below is obtained after $t = 4.5T_L$. The time step was set to $2.5e^{-5}s$ given large Co (between 2 and 80) in the vicinity of the jet orifice during the blowing phase -figure 3.136.

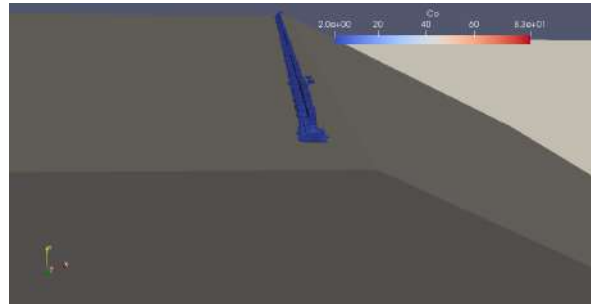


Figure 3.136: CFL condition - DES 3D kwSST simulations Mesh 3 - controlled case $f/DC=180\text{Hz}/50$.

Pressure coefficient results

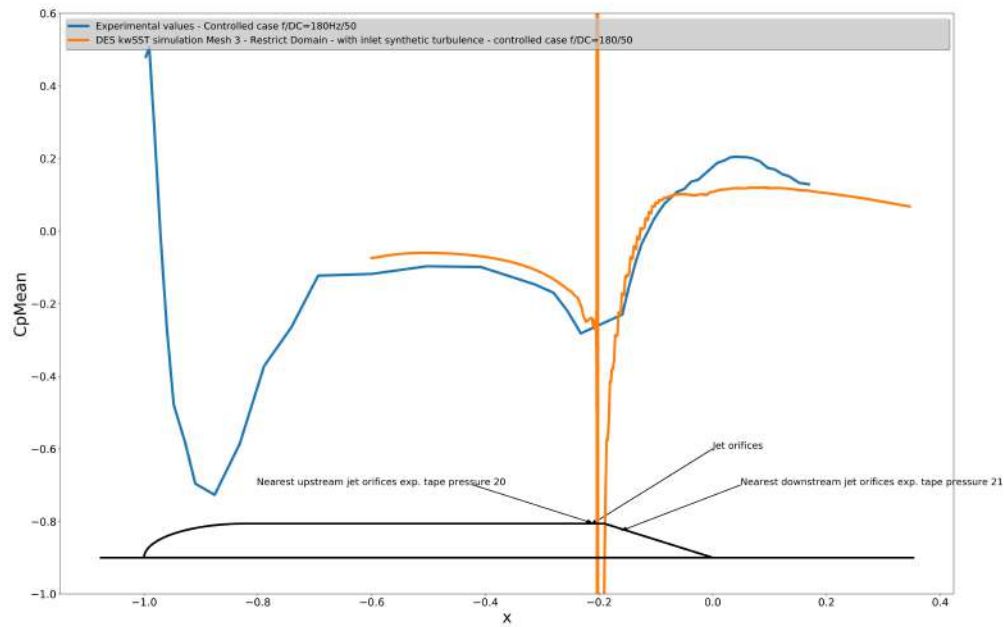


Figure 3.137: Pressure coefficient middle plane $z=0$ - DES 3D kwSST simulations Mesh 3 and experimental data - controlled case $f/DC=180\text{Hz}/50$.

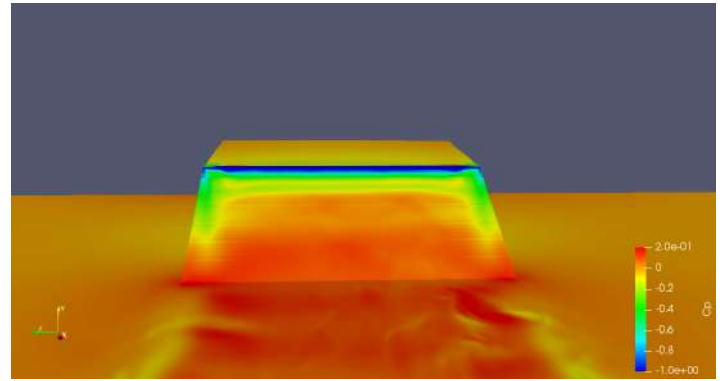
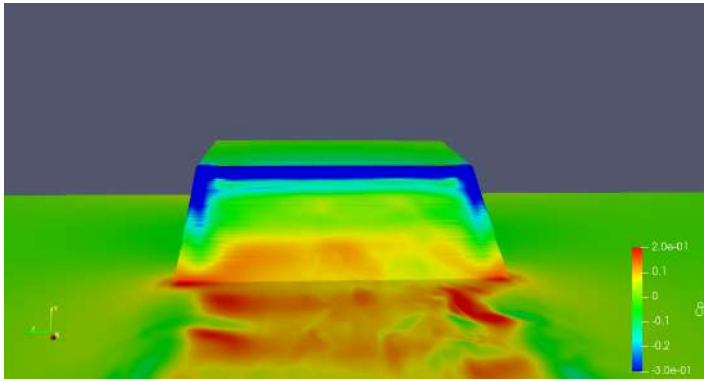


Figure 3.138: Pressure coefficient at the rear of the shape on the ramp represented on two different scales - DES 3D kwSST simulations Mesh 3 - controlled case $f/DC=180\text{Hz}/50$.

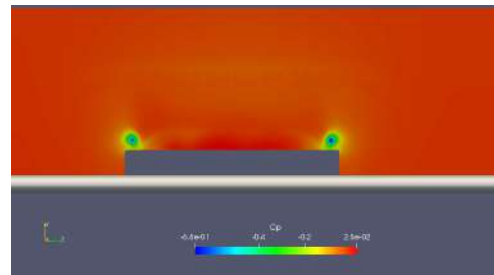
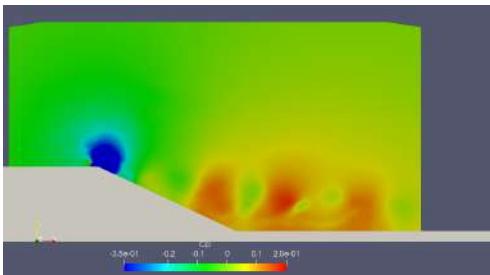


Figure 3.139: Pressure coefficient middle plane $z=0$ (left) and transverse plane $x=1.53\text{ m}$ (right) - DES 3D kwSST simulations Mesh 3 - controlled case $f/DC=180\text{Hz}/50$.

Mean flow topology results

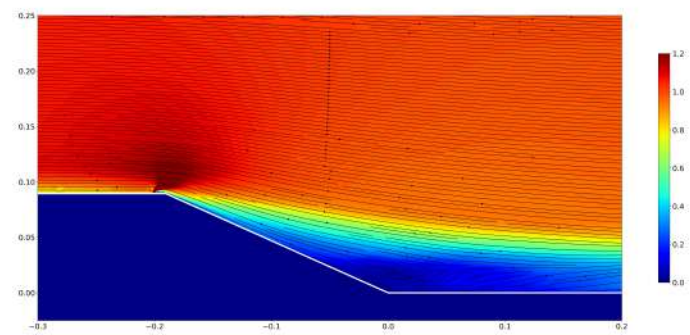
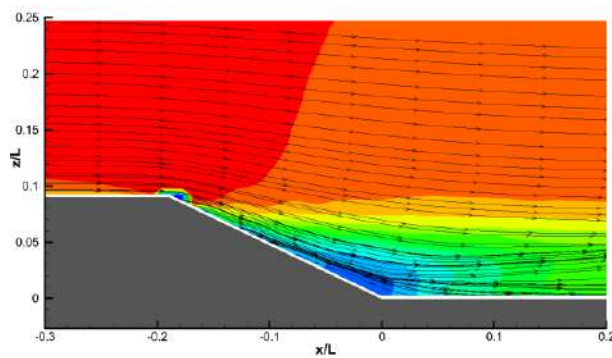


Figure 3.140: Streamline mean adimensional velocity middle plane $z=0$ - Experimental data [5] (left) - Streamline mean adimensional velocity middle plane $z=0$ - DES 3D kwSST Mesh 3 (right) - controlled case $f/DC=180\text{Hz}/50$.

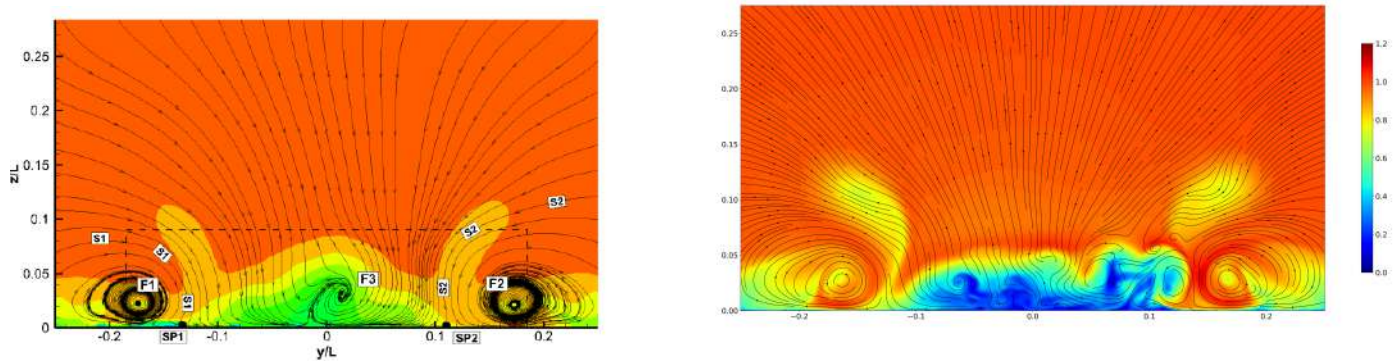


Figure 3.141: Streamline mean adimensional velocity transverse plane $x=1.77$ m - Experimental data [5] (left) - Streamline **instantaneous** adimensional velocity transverse plane $x=1.77$ m - DES 3D kwSST Mesh 3 (right) - controlled case $f/DC=180\text{Hz}/50$.

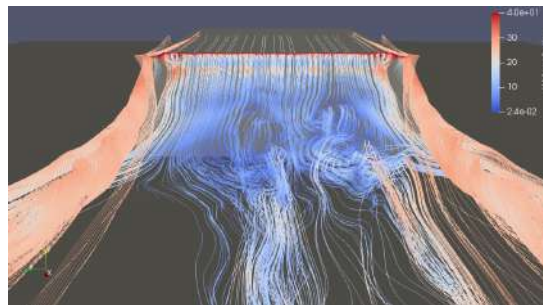


Figure 3.142: U **instantaneous** streamline at the rear - DES 3D kwSST simulations Mesh 3 - controlled case $f/DC=180\text{Hz}/50$.

Unsteady flow topology results

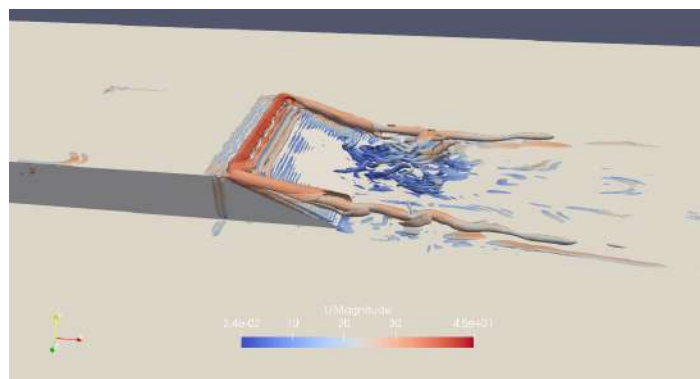


Figure 3.143: Q criterion DES 3D kwSST simulations Mesh 3 - Contour $Q = \frac{4U_{\infty}^2}{H^2}$ coloured by U_{mean} - controlled case $f/DC=180\text{Hz}/50$.

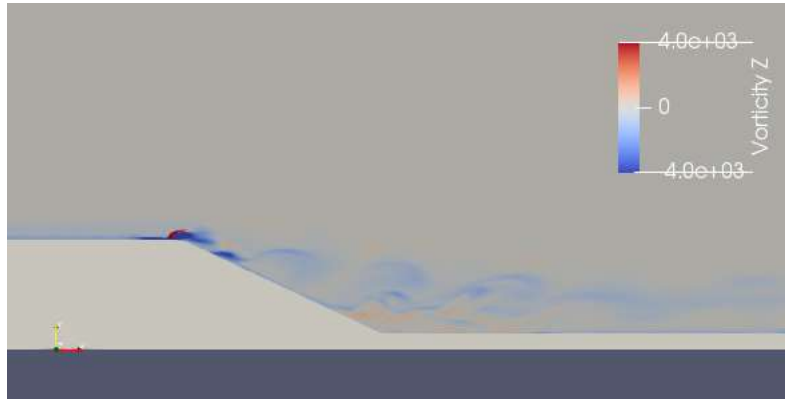


Figure 3.144: Vorticity contour middle plane $z=0$ - DES 3D kwSST simulations Mesh 3 - controlled case $f/DC=180\text{Hz}/50$.

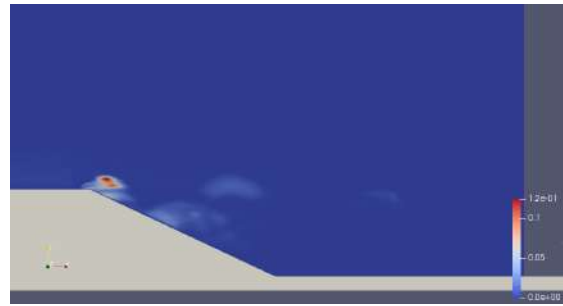


Figure 3.145: nut values over $0.1\text{m}^2/\text{s}$ at the rear - DES 3D kwSST simulations Mesh 3 - controlled case $f/DC=180\text{Hz}/50$.

3.6.7 Discussion

It is important to note here for the discussion of results and the comparison with experimental data that there was no experimental pressure step in the zone of the jet orifices, in their vicinity and just after the separation zone, so the negative pressure peaks found by computation in these zones are not presented in the experimental results.

Flow topology

The flow topology of the numerical solution in the middle plane $z=0$ is approaching correctly the experimental results -figure 4.11. The reinforcement of the two longitudinal vortices is visible on the figure 3.141. The instantaneous velocity is quite stable in the first portion of the slant after the separation zone -figure 3.142 - and the turbulent structures disappear in this area - see figure 3.143 (right).

Pressure recovery

As we can observe in figure 3.137 the pressure profile calculated for the body in the middle plane matched well with the experimental one. The recovery of pressure is also numerically observable and well represented on the rear slant except at the very end of it where the numerical solution is less optimistic than the experimental observation.

We naturally found a pressure peak of high pressure values just over the jet orifices. A relatively long recovery zone with a peak of weak pressure values, continuing after the separation zone, that is, on the rear slant, can be observed. This area of very low pressure is also highlighted with the 3D representation of the distribution of the C_p on the body - figure 3.138, with values of C_p reaching -1 just in the vicinity of the separation.

This low pressure zone seems to be due to the formation of a strong vortex downstream the jets as already discussed in the section 1.2.2. In our case, this downstream vortex, after his formation on the straight plane just before the separation, seems to separate into two structures after a certain blowing time, one of them reaching the top of the rear slant of the body and inducing a low pressure zone -see figure 3.148.

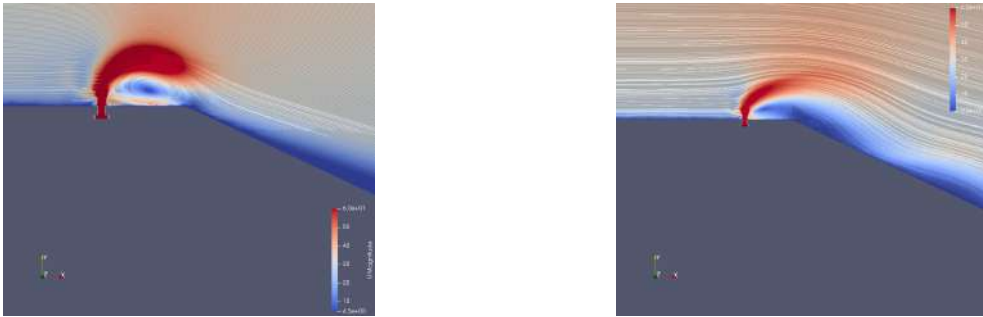


Figure 3.146: Velocity streamline - Formation of a structure of negative circulation with a strong weak pressure zone (Left) - Tilting of the structure on the ramp after a certain blowing time (right) - controlled case $f/DC=180\text{Hz}/50$.

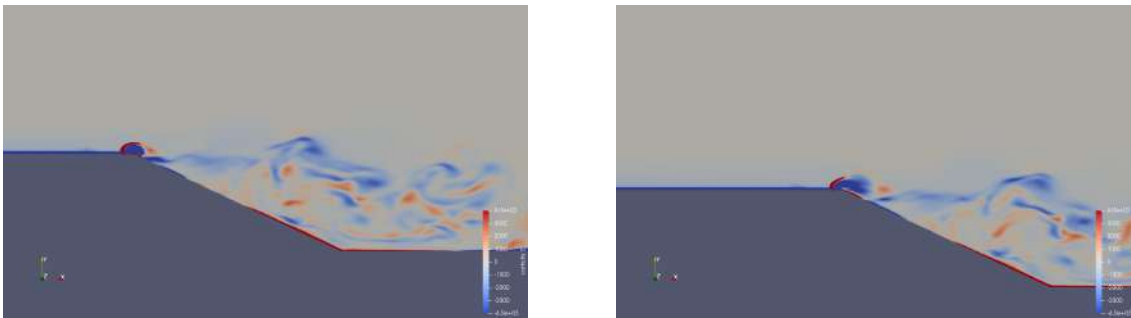


Figure 3.147: Vorticity - Formation of a structure of negative circulation with a strong weak pressure zone (Left) - Tilting of the structure on the ramp after a certain blowing time (right) - controlled case $f/DC=180\text{Hz}/50$.

[11] identified seemingly this phenomenon on low pressure area at the top of a rear windows of an Ahmed body and allocates this phenomenon more because of the reattachment of the flow itself.

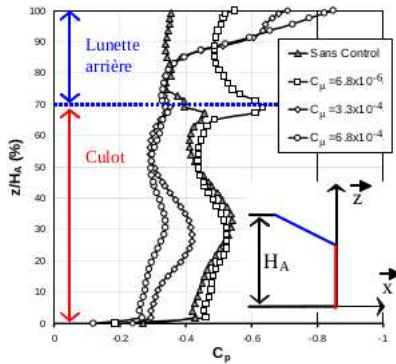


Figure III.12 : Distributions de C_p sur l'arrière de la géométrie simplifiée sans et avec contrôle pour $F_w^* = 1$ et $C_\mu = 0, 6.8 \times 10^{-6}, 3.3 \times 10^{-4}, 6.8 \times 10^{-4}$

- **Un second phénomène** est associé à l'existence d'une région à très faibles coefficients de pression statique, de l'ordre de $C_p = -0.85$. Aucun plateau de pression n'est mis en évidence, la valeur minimale de pression statique est relevée sur le haut de la lunette arrière et les coefficients de pression statique augmentent du haut vers le bas de la lunette arrière. Ce phénomène physique, traditionnellement associé au recollement de la couche limite sur des profils d'aile et ici sur la lunette arrière, apparaît pour des C_μ supérieurs ou égaux à 3.3×10^{-4} .

Figure 3.148: Low pressure area at the top of a rear windows of an Ahmed body [11]

The two low pressure zones at the right and left edge of the slant - figure 3.138 and 3.139 (right), already present in the uncontrolled case and induced by the two longitudinal vortices, are reinforced as these two vortices reduce the global pressure recovery after the separation and question an interesting prevision drag reduction.

Drag coefficient analysis

	ReL.10-6	CD Uncontrolled flow	CD Controlled flow f/DC=180/50	CD gain in %
Experimental estimation	2,35	0,206	0,0026	98,74
Numerical simulation	2,35	0,178	0,118956	33,17

Figure 3.149: C_D values at the rear slant comparison simulation and experiment - uncontrolled case controlled case $f/DC=180\text{Hz}/50$.

The formula to obtain the C_D on the slant is the same used by [5] :

$$C_D = - \frac{\sum_{i \text{ over-slant-surface}} C_{pi} \Delta S_i}{HW}$$

As explained in the section 2.3.2 the drag coefficient obtained by [5] is an estimation of an extrapolation of the pressure measured in the middle plane all over the rear slant. With this technique and because of the lake of experimental pressure tape in the vicinity of the separation zone and at the edge of the slant, more precisely, in the area of supposed by computation low pressure values, the gain on the drag coefficient obtained by [5] could be overestimated. In this numerical work, we obtained a value of C_D for the controlled flow on the slant largely superior to the experimental one, then a significantly inferior gain, though this last one was good with a decrease of 33.17 %.

Chapter 4

Results synthesis and conclusion

4.1 Results synthesis and methods of computation

4.1.1 Methods of computation

This work lasted 12 months. The CFD solver chosen was OpenFOAM, a known freeware using FV methods with a wide variety of turbulence models implemented.

We tried to obtain the solution of the mean flow rapidly first conducting RANS 2D and RANS 3D simulations. Since the problem was exclusively 3D with formation of two contra-rotating longitudinal vortices the RANS 2D strategy was irrelevant. Similarly, the RANS 3D technique with first order turbulence model did not prove effective, possibly because of the large energetic zone of coherent turbulence structures linked with the geometry and the impossibility of modelling a universally developed turbulence that is, with a first order model of turbulence. Therefore a LES strategy had to be considered.

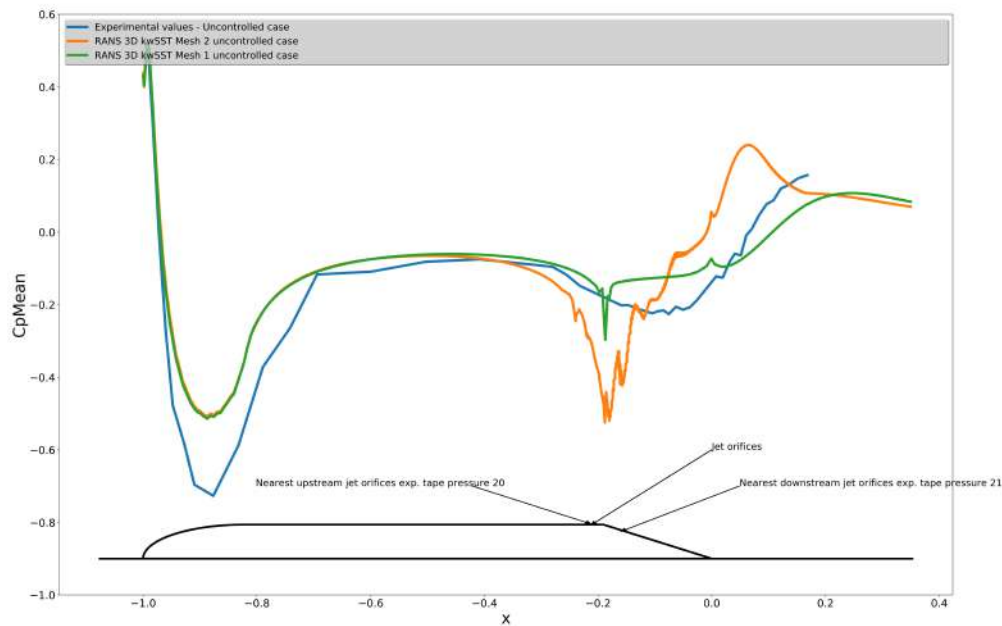


Figure 4.1: Pressure coefficient middle plane $z=0$ - Synthesis RANS 3D kwSST simulations and experimental data - uncontrolled case.

	ReL.10-6	CD Uncontrolled flow
Experimental estimation	2,35	0,206
Numerical simulation RANS mesh1	2,35	0,142712
Numerical simulation RANS mesh2	2,35	0,1612

Figure 4.2: C_D value at the rear slant RANS 3D kwSST 3D synthesis and experiment - uncontrolled case.

A DES simulation on the whole wind-tunnel domain with the appropriate mesh, schemes and time step gives us a good representation of the physical solution, despite an optimistic pressure recovery near the reattachment zone. The mesh must be fine enough to calculate turbulent structures linked to the geometry of the problem, specifically, with a size over l_{EI} -see section 3.2. A acting on the time step and on the accuracy of the schemes, that is, increasing the time step and applying a limiter on the gradient scheme to maintain the stability of the solution during the simulation to gain in computation time was not an effective strategy.

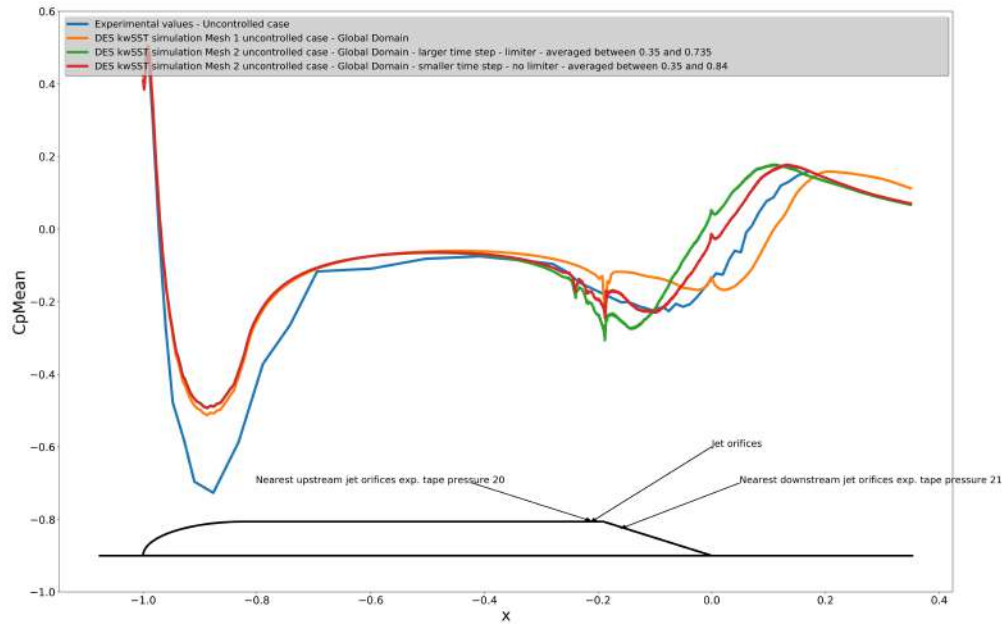


Figure 4.3: Pressure coefficient middle plane $z=0$ - Synthesis RANS 3D kwSST simulations and experimental data - uncontrolled case.

	ReL.10-6	CD Uncontrolled flow
Experimental estimation	2,35	0,206
Numerical simulation DES mesh1 Global Domain	2,35	0,136144
Numerical simulation DES mesh2 Global Domain large time step	2,35	0,1715
Numerical simulation DES mesh2 Global Domain smaller time step	2,35	0,1715

Figure 4.4: C_D value at the rear slant DES 3D kwSST 3D synthesis and experiment - uncontrolled case.

The controlled case required a more refined mesh in the vicinity of the jet orifices with smaller time step. To obtain results within the time constraints of the internship, we had to restrict the domain of calculation. The method implemented in OpenFOAM to obtain turbulent inlet boundary conditions -see section 3.5.5 - is a filtered noise method given synthetic fluctuations. This component of OpenFOAM was tested in this

work, giving us the results expected and were considered satisfying to run an initial calculation of the solution on the controlled case $f_i/DC_i = 180Hz/50$ and to discuss on the preliminary results obtained.

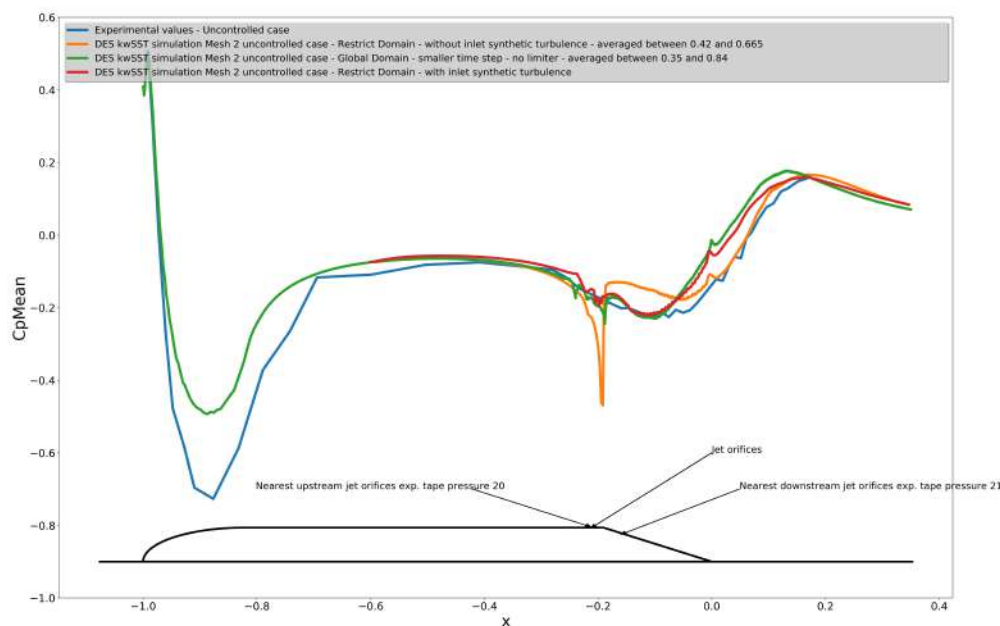


Figure 4.5: Pressure coefficient middle plane $z=0$ - Synthesis RANS 3D kwSST simulations and experimental data - uncontrolled case.

	ReL.10-6	CD Uncontrolled flow
Experimental estimation	2,35	0,206
Numerical simulation DES mesh2 Restrict Domain	2,35	0,242022
Numerical simulation DES mesh2 Restrict Domain with inlet synthetic turbulence	2,35	0,178
Numerical simulation DES mesh2 Global Domain	2,35	0,1715

Figure 4.6: C_D value at the rear slant DES 3D kwSST 3D synthesis and experiment - uncontrolled case.

The run of the controlled case simulation was conducted on the restrict domain with a relatively large time step given large Co values in the vicinity of the jet orifices. However, the results obtained seem to reflect the solution expected linked to the experimental values.

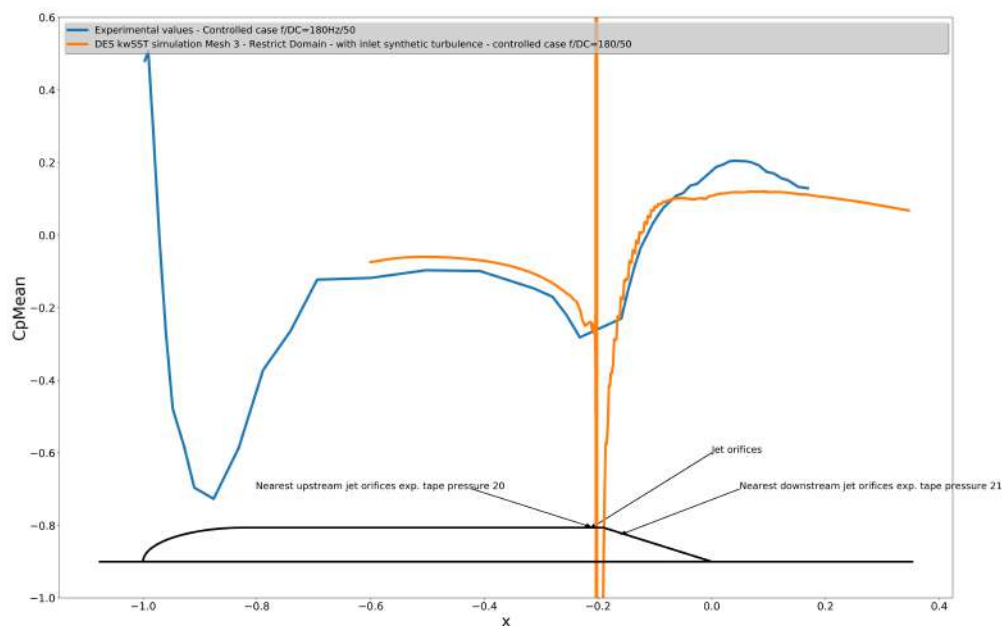


Figure 4.7: Pressure coefficient middle plane $z=0$ - DES 3D kwSST simulations Mesh 3 and experimental data - controlled case $f/DC=180\text{Hz}/50$.

4.1.2 Topology of the flow - synthesis

The best match to the experimental data for the topology of the mean flow is obtained with the DES kwSST simulation on the mesh 2 on the whole domain.

	Distance of reattachement - middle plane - uncontrolled case
Experimental data	0,24
RANS 2D kwSST mesh2	0,486
RANS 3D kwSST mesh1	0,349
RANS 3D kwSST mesh2	recirculation bubble not formed
DES kwSST mesh1	0,369
DES kwSST mesh2 large time step	recirculation bubble not formed
DES kwSST mesh2 small time step	0,275
DES kwSST mesh2 restrict domain	
without inlet synthetic turbulence	0,3
DES kwSST mesh2 restrict domain with inlet synthetic turbulence	0,288

Figure 4.8: Reattachment length values at the rear slant comparison simulation and experiment - uncontrolled case controlled case $f/DC=180\text{Hz}/50$.

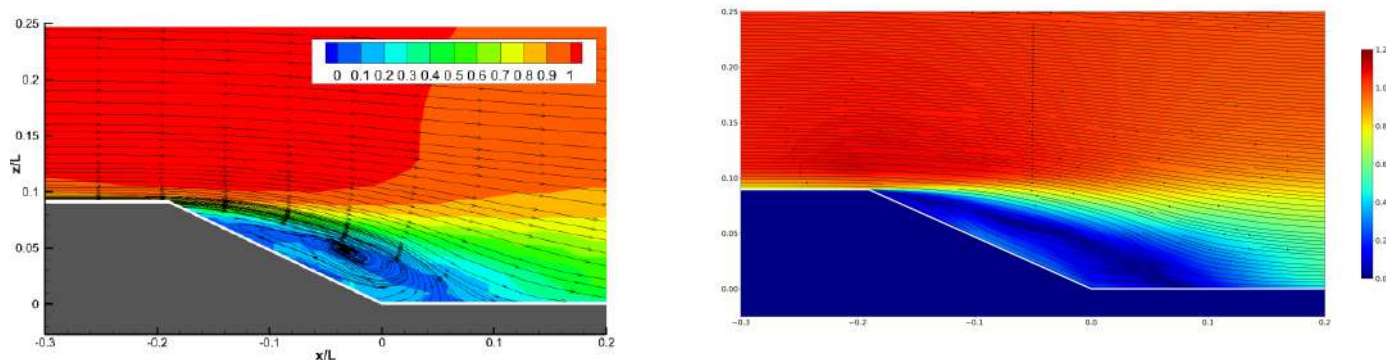


Figure 4.9: Streamline mean adimensional velocity middle plane $z=0$ - Experimental data distance of reattachment $h_r/L = 0.24$ [5] (left) - Streamline mean adimensional velocity middle plane $z=0$ - DES 3D kwSST Mesh 2 distance of reattachment $h_r/L = 0.275$ (right) - uncontrolled case.

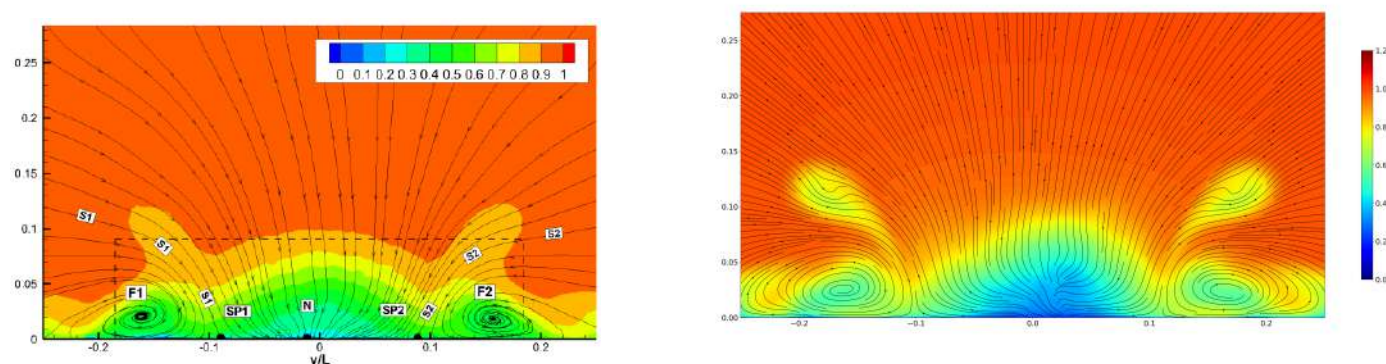


Figure 4.10: Streamline mean adimensional velocity transverse plane $x=1.77$ m - Experimental data [5] (left) - Streamline mean adimensional velocity transverse plane $x=1.77$ m - DES 3D kwSST Mesh 2 (right) - uncontrolled case.

For the controlled case the topology of the mean flow matched well with the experiment.

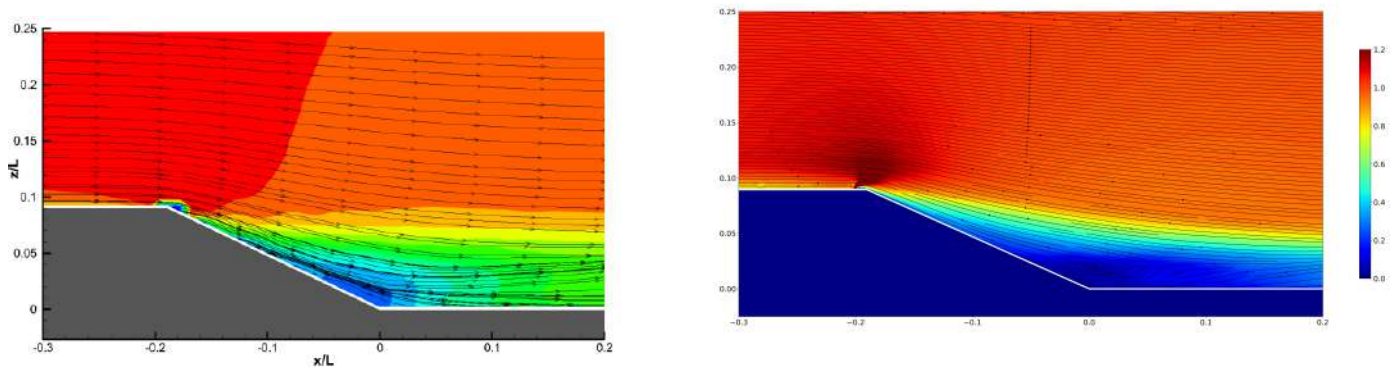


Figure 4.11: Streamline mean adimensional velocity middle plane $z=0$ - Experimental data [5] (left) - Streamline mean adimensional velocity middle plane $z=0$ - DES 3D kwSST Mesh 3 (right) - controlled case $f/DC=180\text{Hz}/50$.

4.1.3 Gain on the drag coefficient - synthesis

Not having used a aerodynamic balance determining the forces and moments on the body Hlevca *et al.* [5] extrapolated the experimental values of pressure measured in the median longitudinal plane over the rear slant surface to estimate the drag coefficient. Previous studies of this type of configuration highlight the presence of two longitudinal vortices inducing low pressure area at the edge of the rear ramp - [22], [3], [11] ... The numerical solutions obtained in this work also present these low pressure areas. Furthermore, it shows up at another area of low pressure at the top of the ramp just after the separation zone where no experimental pressure tape was present. This allows us to gain an estimation of the drag coefficient that is less optimistic than the one deduced from the experimental results.

	ReL.10-6	CD Uncontrolled flow	CD Controlled flow $f/DC=180/50$	CD gain in %
Experimental estimation	2,35	0,206	0,0026	98,74
Numerical simulation	2,35	0,178	0,118956	33,14

Figure 4.12: C_D values at the rear slant comparison simulation and experiment - uncontrolled case controlled case $f/DC=180\text{Hz}/50$.

4.2 Conclusion and next steps

A DES simulation strategy was adapted to obtain satisfying results for this problem. A restriction of the domain of computation with inlet synthetic turbulence significantly improves the calculation performances without degrading the solution, giving the possibility of further parametric changes on the problem in this study.

With more time or computational resources, it could be interesting to refine the mesh near the reattachment point or extend the zone 6 of the mesh further over the wake flow to avoid the gap observed in this zone between the numerical solution and the physical solution, whether for the case with control or without control.

Areas of low pressure on the ramp found numerically were not considered in the experience [5] to estimate the drag coefficient because they were not detected by the middle plane pressure sensors. Therefore, the gain on the drag coefficient obtained in the case of AFC applied seems to be overestimated by [5].

For the controlled case a first run on the restrict domain with a large time step and with inlet synthetic turbulence was conducted, and gave sufficient results. A run on the whole domain or on the restrict domain with synthetic turbulence at the inlet, and with smaller time step must be done to confirm the low pressure zone at the top of the ramp, and to confirm the way the down-flow jet vortex is formed and tilts on the ramp. In the experimental study [5] varying the frequency and keeping the blowing time constant did not provide significant results on variations on the pressure recovery. From there, it could be interesting to study numerically the formation and evolution of the down-flow jet vortex -centre of a low pressure area- at different blowing times keeping the frequency constant.

Bibliography

- [1] S. Ahmed, R. Ramm, and G. Falting. Some salient features of the time averaged ground vehicle wake. *SAE Technical Paper Series 840300*, 1984.
- [2] Alexandra Danet. *Influence des conditions amont sur l'écoulement derrière une marche par la Simulation des Grandes Echelles*. PhD thesis, INPG, 2001.
- [3] Yoann Eulalie. *Étude aérodynamique et contrôle de la traînée sur un corps de Ahmed culot droit*. PhD thesis, Université de Bordeaux, 2014.
- [4] Zhao Guoqing and Zhao Qijun. Parametric analyses for synthetic jet control on separation and stall over rotor airfoil. *Chinese Journal of Aeronautics*, 2013.
- [5] Dan Hlevca, Patrick Gilliéron, and Francesco Grasso. Experimental study of the active control applied to the flow past a backward facing ramp. *Experiments in Fluids*, 2018.
- [6] Ryan Holman, Yogen Utturkar, Rajat Mittal, Barton L. Smith, and Luis Cattafesta. Formation criterion for synthetic jets. *AIAA Journal*, 2005.
- [7] Marc Christian Immer. *Time-resolved measurement and simulation of local scale turbulent urban flow*. PhD thesis, ETH Zurich, 2016.
- [8] P. Joseph, X. Amandolèse, and J.-L. Aider. Drag reduction on the 25 slant angle ahmed reference body using pulsed jets. *Experiments in Fluids*, 2012.
- [9] Pierrick Joseph, Dorian Bortolus, and Francesco Grasso. Flow control on a 3d backward facing ramp by pulsed jets. *Comptes Rendus Mécanique*, 2014.
- [10] Georgi Kalitzin, Gorazd Medic, Gianluca Iaccarino, and Paul Durbin. Near-wall behavior of rans turbulence models and implications for wall functions. *Computational physics*, 2004.
- [11] Cédric LECLERC. *REDUCTION DE LA TRAINEE D'UN VEHICULE AUTOMOBILE SIMPLIFIE A L'AIDE DU CONTROLE ACTIF PAR JET SYNTHETIQUE*. PhD thesis, INSTITUT NATIONAL POLYTECHNIQUE DE TOULOUSE, 2008.
- [12] H. Lienhart and S. Becker. Flow and turbulence structure in the wake of a simplified car model. *SAE Technical Paper Series 2003-01-0656*, 2003.
- [13] Florian Menter and Thomas Esch. Elements of industrial heat transfer predictions. *Proceedings of COBEM*, 2001.

- [14] Jens Ortmanns, Martin Bitter, and Christian J. Khler. Dynamic vortex structures for flow-control applications. *Exp Fluids*, 2008.
- [15] P.-Y. Pamart, J. Danois, E. Garnier, and P. Sagaut. Large eddy simulation study of synthetic jet frequency and amplitude effects on a rounded step separated flow. *AIAA Journal*, 2010.
- [16] Stephen B. Pope. Turbulent flow.
- [17] Bhanu Prakash, J M Bergada, and F. Mellibovsky. Three dimensional analysis of ahmed body aerodynamic performance enhancement using steady suction and blowing flow control techniques. *Tenth International Conference on Computational Fluid Dynamics (ICCFD10)*, 2018.
- [18] Barnard R.H. Road vehicle aerodynamic design. *Mechaero Publishing*, 2001.
- [19] P.R. Sparlat and S.R. Allmaras. A one-equation turbulence model for aerodynamic flows. *AIAA Journal*, 1992.
- [20] P.R. Sparlat, W-H Jou, M. Strelets, and S.R. Allmaras. Comments on the feasibility of les for wings, and on a hybrid rans/les approach. 1997.
- [21] Michael Strelets. Detached eddy simulation of massively separated flows. *AIAA Journal*, 2001.
- [22] Adrien THACKER. *CONTRIBUTION EXPÉRIMENTALE Á L'ANALYSE STATIONNAIRE ET INSTATIONNAIRE DE L'ÉCOULEMENT Á L'ARRIÈRE D'UN CORPS DE FAIBLE ALLONGEMENT*. PhD thesis, Laboratoire PRISME - UNIVERSITÉ D'ORLÉANS, 2010.